

# **Shape-temperature relationship of ice crystals in mixed-phase clouds based on observations with polarimetric cloud radar**

Der Fakultät für Physik und Geowissenschaften  
der Universität Leipzig  
eingereichte

D I S S E R T A T I O N

zur Erlangung des akademischen Grades

DOCTOR RERUM NATURALIUM  
Dr. rer. nat.

vorgelegt

von Diplom-Ingenieur Alexander Myagkov  
geboren am 18. Oktober 1987 in Chernenko, UdSSR

Gutachter: Prof. Dr. Andreas Macke  
Prof. Dr. Herman Russchenberg

Tag der Verleihung: 19. September 2016



**Bibliographic description:**

Myagkov, Alexander

Shape-temperature relationship of ice crystals in mixed-phase clouds based on observations with polarimetric cloud radar

University of Leipzig, Dissertation

125 p., 194 ref., 42 fig., 7 tab.

**Abstract:**

This thesis is devoted to the experimental quantitative characterization of the shape and orientation distribution of ice particles in clouds. The characterization is based on measured and modeled elevation dependencies of the polarimetric parameters differential reflectivity and correlation coefficient. The polarimetric data is obtained using a newly developed 35-GHz cloud radar MIRA-35 with hybrid polarimetric configuration and scanning capabilities. The full procedure chain of the technical implementation and the realization of the setup of the hybrid-mode cloud radar for the shape determination are presented. This includes the description of phase adjustments in the transmitting paths, the introduction of the general data processing scheme, correction of the data for the differences of amplifications and electrical path lengths in the transmitting and receiving channels, the rotation of the polarization basis by  $45^\circ$ , the correction of antenna effects on polarimetric measurements, the determination of spectral polarimetric variables, and the formulation of a scheme to increase the signal-to-noise ratio. Modeling of the polarimetric variables is based on existing back-scattering models assuming the spheroidal representation of cloud scatterers. The parameters retrieved from the model are polarizability ratio and degree of orientation, which can be assigned to certain particle orientations and shapes.

In the thesis the first quantitative estimations of ice particle shape at the top of liquid-topped clouds are presented. Analyzed ice particles were formed in the presence of super-cooled water and in the temperature range from  $-20^\circ\text{C}$  to  $-3^\circ\text{C}$ . The estimation is based on polarizability ratios of ice particles measured by the MIRA-35 with hybrid polarimetric configuration, manufactured by METEK GmbH. For the study, 22 cases observed during the ACCEPT (Analysis of the Composition of Clouds with Extended Polarization Techniques) field campaign were used. Polarizability ratios retrieved for cloud layers with cloud-top temperatures of about  $-5$ ,  $-8$ ,  $-15$ , and  $-20^\circ\text{C}$  were 1.6, 0.9, 0.6, and 0.9, respectively. Such values correspond to prolate, quasi-isotropic, oblate, and quasi-isotropic particles, respectively. Data from a free-fall chamber were used for the comparison. A good agreement of detected shapes with well-known shape-temperature dependencies observed in laboratories was found.





---

# Table of Contents

<b>1</b>	<b>Introduction</b>	<b>1</b>
<b>2</b>	<b>Formation and development of ice particles: Laboratory studies and remote observations</b>	<b>7</b>
2.1	Heterogeneous ice formation in the atmosphere . . . . .	7
2.2	Laboratory investigations of ice crystal development . . . . .	10
2.3	Polarimetric radar observations of ice microphysics . . . . .	12
2.3.1	Polarimetry in weather radar networks . . . . .	13
2.3.2	Polarimetry in cloud radars . . . . .	16
2.3.3	Polarization coupling . . . . .	19
2.4	Aims and scientific questions . . . . .	20
<b>3</b>	<b>Effects of antenna patterns on cloud radar polarimetric measurements</b>	<b>21</b>
3.1	Measurements of complex antenna patterns . . . . .	21
3.1.1	Problem definition . . . . .	22
3.1.2	Measurement description . . . . .	26
3.1.3	Results of antenna pattern measurements . . . . .	30
3.2	Correction of LDR measurements . . . . .	35
3.3	Discrimination between insects and clouds . . . . .	42
<b>4</b>	<b>Cloud radar MIRA-35 with hybrid mode</b>	<b>45</b>
4.1	Implementation and phase adjustment . . . . .	45
4.2	Processing of the coherency matrix . . . . .	49
4.3	Correction of the coherency matrix for differences of channels . . . . .	50
4.4	The coherency matrix in the slanted basis . . . . .	50
4.5	Correction for the antenna coupling . . . . .	53
4.6	Spectral polarimetric variables . . . . .	54
4.7	Sensitivity issue . . . . .	56

---

<b>5</b>	<b>Shape and orientation retrieval</b>	<b>59</b>
5.1	Backscattering model . . . . .	59
5.2	Retrieval technique . . . . .	66
5.3	Case study . . . . .	70
<b>6</b>	<b>Shape-temperature relationship of pristine ice crystals</b>	<b>77</b>
6.1	Instrumentation and data set . . . . .	77
6.2	Examples of the shape retrieval . . . . .	81
6.2.1	Case 1: 12 October 2014, 15:00–16:00 UTC . . . . .	81
6.2.2	Case 2: 18 October 2014, 01:00–02:00 UTC . . . . .	83
6.2.3	Case 3: 20 October 2014, 18:00–19:00 UTC . . . . .	85
6.2.4	Case 4: 10 November 2014, 02:00–03:00 UTC . . . . .	87
6.2.5	Case 5: 7 November 2014, 20:00–21:00 UTC . . . . .	89
6.3	Comparison of shape with laboratory studies . . . . .	91
6.4	Orientation of pristine ice crystals . . . . .	94
<b>7</b>	<b>Summary and outlook</b>	<b>95</b>
	<b>Bibliography</b>	<b>99</b>
	<b>List of Abbreviations</b>	<b>119</b>
	<b>List of Symbols</b>	<b>121</b>

---

# Chapter 1

## Introduction

Clouds are one of the main atmospheric components and play an essential role in the global climate system. With an albedo of up to 80 % [Mazin and Khrgian, 1989; Liu *et al.*, 2011] clouds scatter a large part of the solar radiation back to the space. On the other hand, clouds contribute to the greenhouse effect by reflecting back the long-wave radiation emitted by the Earth's surface. Covering on average 75 % of the sky [Wylie *et al.*, 2005], clouds influence the global radiation budget significantly. The difference between radiation budgets at the Earth surface in cloud and cloud-free conditions in the short-wave and long-wave regions is found to be  $-46.6 \text{ W m}^{-2}$  and  $29.5 \text{ W m}^{-2}$ , respectively [Loeb *et al.*, 2009]. The microphysical properties of clouds are in addition susceptible to variations in the properties of aerosol particles which are required as nuclei of cloud droplets and ice crystals. Because aerosol conditions are changed by human activity, also anthropogenic effects on cloud properties are likely. Recent investigations have shown that the effective anthropogenic radiative forcing at the Earth surface induced by aerosol-cloud interaction is in the range from  $-1.2$  to  $0 \text{ W m}^{-2}$  [Flato *et al.*, 2013]. The negative values indicate that anthropogenic effects of aerosols on clouds cause radiative cooling of the atmosphere. Unfortunately, a low confidence level of this estimation limits our understanding of the exact impact of clouds and aerosol-cloud interaction on the climate.

Water and energy transportation within the global hydrological cycle cannot function without clouds [Chahine, 1992]. Cloud systems are mainly sustained by moisture from the oceans and produce liquid and solid precipitation over land. Based on long-term gauge and satellite observations the annual mean precipitation rate over the last several decades was found to be about  $2.6 \text{ mm d}^{-1}$  [Xie and Arkin, 1997; Chen *et al.*, 2002; Adler *et al.*, 2003]. In other words, about  $1.3 \times 10^{12} \text{ kg}$  of water precipitates from clouds every day,  $\sim 23 \%$  of that precipitation amount occurs over land. This amount of water refreshes ice glaciers and ground water, which are source not only of water for vegetation and population, but also for hydroelectric power plants. On the other hand, spatial and temporal variability in

---

precipitation amounts can cause hazards such as floods, droughts, and storms. Thus, an accurate characterization of cloud formation and development can improve predictability of severe weather events [Tippett *et al.*, 2015] and a quantification of future water resources and hydrological extremes for agriculture [Piras *et al.*, 2014] especially in the face of global climate change.

Satellite-based observations from 2005 to 2011 showed that the majority of liquid precipitation over land is sourced from cold clouds [Mülmenstädt *et al.*, 2015], i.e. the formation of raindrops includes the ice phase. Moreover, the authors also showed that in mid-latitudes 30 to 50 % of cold clouds producing liquid precipitation are mixed-phase, i.e. they contain coexisting liquid water droplets and ice crystals. Such a coexistence has been also often registered in numerous in situ and remote observations of the atmosphere [Raubert, 1987; Cober *et al.*, 2001a; Mazin, 2006; De Boer *et al.*, 2009; Shupe, 2011]. In general, precipitation produced by mixed-phase clouds is more intense in comparison with the one formed in purely liquid clouds [Niu and Li, 2012]. This phenomenon is the result of the Wegener-Bergeron-Findeisen process [Findeisen *et al.*, 2015] which describes the efficient growth of ice crystals to precipitation-sized hydrometeors in air masses that are unsaturated with respect to liquid water but saturated with respect to ice. Besides their relevance for precipitation formation, the long-lasting nature of mixed-phase clouds impacts the radiative budget and the thermodynamic structure of the atmosphere [Sun and Shine, 1994, 1995; McFarquhar and Cober, 2004; Yoshida and Asano, 2005]. In addition, the presence of supercooled liquid water in clouds is a serious hazard for short-haul regional aircraft [Cober *et al.*, 2001b] and unmanned aerial vehicles [Siquig, 1990; Curry *et al.*, 2004; Kankiewicz *et al.*, 2005]. Sand *et al.* [1984] showed the influence of supercooled liquid water on the aircraft performance, which can be considerably reduced because of increased drag and decreased lift. Finally, mixed-phase cloud layers can hamper military missions such as a target's detection, usage of opto-electronic sensors and weapons, refueling and strike missions [Fleishauer *et al.*, 2002; Kankiewicz *et al.*, 2005]. In spite of the importance of mixed-phase clouds, they are still understudied in comparison to single-phase clouds [Luke *et al.*, 2010; Zhang *et al.*, 2010], because of the respectively large number of processes occurring in mixed-phase clouds [Morrison *et al.*, 2012].

Existing models, based on the Wegener-Bergeron-Findeisen mechanism [Korolev and Mazin, 2003], show the high instability of supercooled liquid layers. Modeling results indicate that due to their instability mixed-phase clouds can completely glaciate within several hours. In contrast, observations have shown that mixed-phase clouds can persist in the atmosphere for days up to a week [Zuidema *et al.*, 2005; Shupe, 2011; Morrison *et al.*, 2012; Westbrook and Illingworth, 2013]. For a better understanding of such large-scale processes it is necessary to investigate the mechanisms that take place in mixed-phase clouds at smaller temporal and spatial scales. Accurate modeling of these mechanisms requires detailed infor-

---

---

mation on cloud particle size, number concentration, shape, and phase [McFarquhar *et al.*, 2013]. Precise data in convective precipitating mixed-phase cloud systems, which have a strong impact on the global precipitation and radiation budgets, is often unavailable. Airborne in situ measurements in such cloud systems are limited because of dangerous icing conditions for aircraft and the instrumentation carried aboard. Remote-sensing observations are hampered by propagation effects and signal attenuation in particular. Moreover, interpretation of available data sets is complicated because of numerous processes occurring in convective precipitating cells. For instance, the number of transition processes between water vapor, liquid, and ice can exceed 25 [Tao and Moncrieff, 2009]. Therefore, thin mixed-phase clouds with a single supercooled liquid layer at the top and ice virgae below are of special interest [Wang *et al.*, 2004; Smith *et al.*, 2009]. Such clouds have less complex microphysical and dynamical properties [Fleishauer *et al.*, 2002; Ansmann *et al.*, 2009; Zhang *et al.*, 2012] and, thus, are considered as a key to obtain a comprehensive picture of the formation of pristine ice crystals under ambient conditions. The knowledge about the pristine ice crystal properties will allow for an accurate characterization of subsequent processes such as ice multiplication and precipitation formation.

Ground-based remote sensing has shown a large potential for improving the understanding of the lifecycle of thin mixed-phase clouds [Hogan *et al.*, 2003; Ansmann *et al.*, 2009; De Boer *et al.*, 2009; Delanoë and Hogan, 2010; Kanitz *et al.*, 2011; Westbrook and Illingworth, 2013]. Even though microphysical retrieval techniques based on ground-based remote observations are a valuable source of information for studying mixed-phase clouds, further investigations are required in order to increase the accuracy of these retrievals. One important and yet barely explored parameter is the predominant shape of ice crystals within a population. Estimates of ice mass, area, or number concentration require knowledge of particle shape [Westbrook and Heymsfield, 2011; Delanoë *et al.*, 2014]. De Boer *et al.* [2009] considered the shape of ice particles to be the largest source of errors in existing size and number concentration retrievals that are based on combined lidar and radar vertical observations. For instance, the authors reported that the assumed ice particle shape can cause changes in the calculated effective size and number concentration of up to 200  $\mu\text{m}$  and 90  $\text{l}^{-1}$ , respectively. In existing microphysical models an accurate representation of ice particle shape plays an important role as the shape parameterizes size–mass–terminal velocity relations of ice crystals [Mitchell, 1996; Delanoë *et al.*, 2014], the depositional growth rate [Westbrook and Heymsfield, 2011], and scattering properties of the ice crystals [Delanoë and Hogan, 2010]. Moreover, knowledge of the ice particles’ shape provides a potential for the retrieval of the particle number size distribution. Such a retrieval can be based on cloud radar Doppler spectra and known relations between size and terminal velocity for different particle habits [Mitchell, 1996]. Mace *et al.* [2002] presented a retrieval of the number size distribution based on the moments of Doppler spectra obtained with a 35-GHz cloud radar.

---

The authors estimated the uncertainties of the retrieval associated with the ice particle habit and found those to be 60 % and 40 % in ice water content (IWC) and median ice particle size, respectively. Continuous information about the number size distribution of ice particles can later on be helpful for a better understanding and characterization of the efficiency of heterogeneous ice formation, which currently is subject of numerous studies [Hoose and Möhler, 2012; Murray *et al.*, 2012; Phillips *et al.*, 2013; Ladino Moreno *et al.*, 2013; DeMott *et al.*, 2015].

Cloud radar is one of the most promising remote-sensing instruments for particle shape determination. Recent investigations of Kneifel *et al.* [2011] and Kneifel *et al.* [2015] show the potential of the multi-frequency approach in the separation of snow particle habits when Mie scattering is present. According to Kneifel *et al.* [2015], the approach is most effective for a median volume diameter exceeding 2 mm. Often, nevertheless, characterization of smaller ice crystals is required. For example, in thin mid-level mixed-phase clouds the typical size of ice crystals is about an order of magnitude lower, hampering the applicability of the multi-frequency approach.

Another powerful tool for the shape estimation of cloud particles is cloud-radar polarimetry. The polarimetric approach is known to be effective in the case when cloud particles can be approximated using the well-known spheroidal model [Holt, 1984]. Matrosov [1991a] presented theoretical considerations about the potential of polarimetric cloud radars for the shape classification of ice crystals. The author analyzed modeled elevation dependencies of polarimetric products that could be measured with several polarimetric configurations. Matrosov and Kropfli [1993], Matrosov *et al.* [2001], and Reinking *et al.* [2002] experimentally evaluated the proposed polarimetric configurations that were emulated using rotatable quarter- and/or half-wavelength phase plates. The plates were mounted into the waveguide system of a ground-based Ka-band radar, operated by the Wave Propagation Laboratory of the National Oceanic and Atmospheric Administration (NOAA). A number of studies present polarimetric measurements of winter clouds taken by airborne [Galloway *et al.*, 1997; Wolde and Vali, 2001] and ground-based cloud radars [Pazmany *et al.*, 1994; Lohmeier *et al.*, 1997; Reinking *et al.*, 2002]. Often such measurements were compared with the microphysical properties of the ice crystals observed in situ with aircraft or on ground. Despite the observational evidence that polarimetric variables are sensitive to the shape of particles, which was confirmed by the above-mentioned studies, further investigations in this area are required to realize an operational quantitative characterization of particle shape [Matrosov *et al.*, 2012]. An approach to quantitatively obtain the particle shape and orientation from weather radar observations of polarimetric parameters was, e.g., presented by Melnikov and Straka [2013], but their retrieval has limitations in the discrimination between oblate and prolate particles.

Even though the potential of different polarimetric configurations for a detailed shape retrieval of hydrometeors were evaluated in the above-mentioned studies, many cloud radars

---

---

are operated in simpler configurations. The widely used spaceborne 94-GHz cloud profiling radar aboard the Cloudsat satellite has no polarization capabilities at all [Stephens *et al.*, 2008]. Other systems are operating in the depolarization mode (also known as polarization diverse mode). In this mode the radar emits a wave with a certain constant polarization state (usually linear or circular) and receives co-polarized and cross-polarized components of the backscattered wave. This is, e.g., the case for the default setup of MIRA-35 [Görsdorf *et al.*, 2015] as well as the Ka-band Zenith-pointing Radar of the US Department of Energy Atmospheric Radiation Measurement program. Normally, such radars provide only one polarimetric product – the depolarization ratio which is the ratio of the returned power in the cross-polarized channel to the returned power in the co-polarized channel. If only the depolarization ratio is used to derive an estimate of ice particle shape, an assumption about the distribution of ice crystal orientation has to be made as described by Matrosov *et al.* [2001]. Ryzhkov [2001] concluded that not only power relations but also the correlation between the orthogonal components of the received wave should be analyzed for the characterization of both shape and orientation distribution.

This work is devoted to the development of a novel polarimetric technique to quantitatively derive shape and orientation of particles as they are formed in thin stratiform mixed-phase clouds. The available experience in the field of radar polarimetry was utilized to implement a new polarimetric configuration into a 35-GHz cloud radar that is able to measure the spectral coherency matrix based on which a set of spectral polarimetric variables can be obtained. The cloud radar performance was evaluated based on a dataset acquired during the ACCEPT (Analysis of the Composition of Clouds with Extended Polarization Techniques) field measurement campaign which took place at the Cabauw Experimental Site for Atmospheric Research (CESAR), the Netherlands, in fall of 2014. Based on the ACCEPT observations the capabilities of the cloud radar and the new polarimetric retrieval technique to derive the shape and orientation of pristine ice crystals was evaluated against well-known shape-temperature relationships for ice crystals grown in laboratories under ambient conditions. A theoretical perspective presented in Chapter 2 covers basics of ice formation in the presence of liquid water and gives an overview on the polarimetric approach for the microphysical studies of ice particles. In the final part of Chapter 2 scientific questions to be answered in the thesis are given based on the previous review. Chapters 3 and 4 are devoted to the technical aspects of the cloud radar MIRA-35, including antenna pattern measurements, technical implementation, and calibration. The retrieval technique for quantitative shape and orientation estimations is described in Chapter 5. The experimental part of this study, covered in Chapters 5 and 6, is based on measurements with a newly developed 35-GHz cloud radar MIRA-35 with hybrid polarimetric configuration and the Leipzig Aerosol and Cloud Remote Observations System (LACROS, Wandinger *et al.* [2012]) collected during the ACCEPT field measurement campaign. A comparison of the parameters of

---

ice crystals obtained from the polarimetric measurements with those from laboratory studies is presented in Chapter 6. In Chapter 7 a summary, conclusions, and outlook are provided. The majority of material presented within this work was published in *Myagkov et al.* [2015], *Myagkov et al.* [2016a], and *Myagkov et al.* [2016b].

---



## Chapter 2

# Formation and development of ice particles: Laboratory studies and remote observations

It is well-known that microphysical properties of ice particles are strongly defined by the ambient conditions under which the crystals form and develop. A snowflake is regarded as a “letter from the sky” in *Nakaya* [1954] since weather conditions are hidden in its morphology. Undergoing different trajectories, ice crystals in the atmosphere experience diverse temperature and humidity regimes. Thus, it is hard to find two crystals with the same structure, although ice particles falling close together may have some apparent similarities [*Nelson*, 2008]. In order to better understand processes influencing the development of ice particles in mixed-phase clouds it is necessary to know under which conditions ice crystals are formed and grow. In the first part of this chapter basics on the formation and initial development of ice crystals in mixed-phase clouds are considered. The second part presents a literature review on the applicability of radar polarimetry for the estimation of microphysical properties of natural ice particles. In the third part of the chapter goals of the study and questions to be answered within this thesis are given.

### 2.1 Heterogeneous ice formation in the atmosphere

Long-term in situ measurements have shown that about 80 % of mid-level clouds occur at temperatures from  $-35$  to  $0$  °C [*Mazin*, 2006]. Under such conditions cloud particles are primarily formed via heterogeneous mechanisms. Heterogeneous formation is only possible in the presence of aerosol particles which at certain environmental conditions can act either as ice nucleating particles (INP, *Vali et al.* [2015]) or as cloud condensation nuclei (CCN) and form ice crystals or liquid drops, respectively. The main fraction of CCN consists of relatively

---

small (diameter  $\sim 100$  nm) salt and organic particles. The efficiency of CCN activation in an aerosol population at a certain level of supersaturation with respect to liquid water is mainly defined by the particle concentration. Analyzing a number of studies on CCN measurements *Andreae* [2009] found that the amount of aerosols acting as CCN is about 10–60 % and 3–50 % for maritime areas and continental zones, respectively. Due to a higher concentration of aerosols over land the typical concentration of CCN over continental areas can be an order of magnitude higher than over the ocean [*Pruppacher and Klett*, 1997, ch. 9]. *Andreae* [2009] showed that values of CCN concentration at 0.4 % supersaturation for the marine atmosphere vary from  $2.3 \times 10^7 \text{ m}^{-3}$  in remote regions to  $1.7 \times 10^9 \text{ m}^{-3}$  in polluted regions. In the continental atmosphere CCN concentrations range from  $9 \times 10^7 \text{ m}^{-3}$  to  $9.1 \times 10^9 \text{ m}^{-3}$ .

The ability of aerosol particles to activate the ice nucleation process or to initiate condensation of liquid water at certain atmospheric conditions strongly depends on their size and chemical composition. In general, particles acting as INP are large (diameter  $\sim 1 \mu\text{m}$ ), solid, water-insoluble particles. The most efficient INP are mineral dust, metals, and biological particles. Up to 50 % of INP consist of mineral dust [*DeMott et al.*, 2003a; *Baustian et al.*, 2012], sourced from deserts in Africa, the Middle East, or Asia [*Sassen*, 2002; *DeMott et al.*, 2003b; *Sassen et al.*, 2003; *Richardson et al.*, 2007; *Kamphus et al.*, 2010].

Size, concentration, and chemical composition of INP define the nucleation mechanism and rate of ice formation in mixed-phase clouds. Based on long-term lidar observations in different geographical locations *Seifert et al.* [2010] and *Kanitz et al.* [2011] report that the fraction of ice-containing clouds is strongly dependent on aerosol properties. Vast reviews of laboratory studies on ice nucleation by different types of aerosols were given by *Baustian et al.* [2012], *Hoose and Möhler* [2012], and *Ladino Moreno et al.* [2013]. In general, INP concentration increases exponentially with decreasing ambient temperature. At temperatures from  $-25$  to  $-10$  °C the INP concentration is several orders of magnitude lower than the concentration of CCN and typically ranges from 10 to  $5 \times 10^5 \text{ m}^{-3}$  [*DeMott et al.*, 2010].

Beside concentrations of CCN and INP, atmospheric ambient conditions have a strong impact on the microphysical properties of formed ice crystals. For example, laboratory investigations by *Matsuo and Fukuta* [1987] showed differences between ice particles grown at conditions close to ice saturation (IS) and water saturation (WS). The authors found that liquid-dependent formation results in ice crystals having up to an order of magnitude larger size and mass, and, therefore, faster sedimentation velocity. In addition, ambient temperature defines the shape of formed ice particles. Figure 2.1 represents a comprehensive morphological diagram of ice crystal habit as a function of temperature and humidity [*Bailey and Hallett*, 2009]. At temperatures between  $-20$  and  $0$  °C ice crystals have a primary shape while at lower temperatures a mixture of different types of particles can occur. In the single crystalline mode, the shape of ice particles formed at IS features in general similar temperature dependencies as at WS, but the shape is less pronounced [*Matsuo and Fukuta*,

---

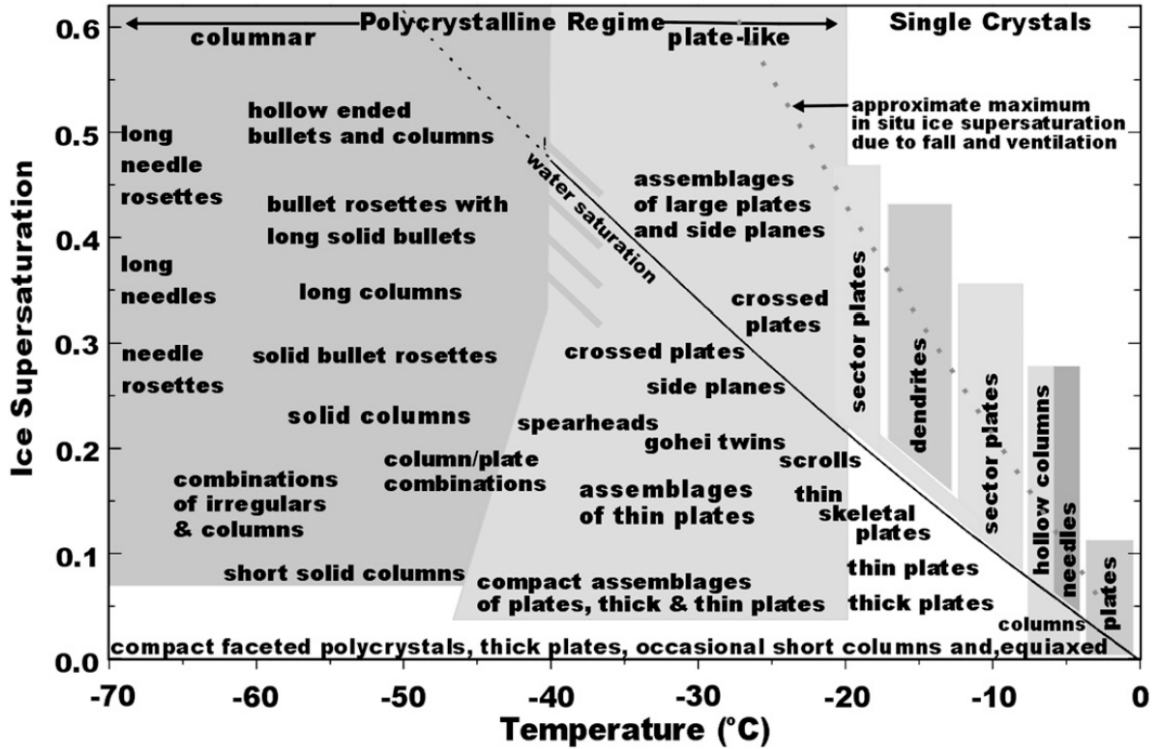


Figure 2.1: Habit diagram for ice crystals at different formation conditions. The figure is adopted from Bailey and Hallett [2009].

1987]. Mechanisms associated with the formation of ice crystal habits are addressed in Sec. 2.2.

Formation of the ice phase in mixed-phase clouds can be strongly affected by the presence of supercooled liquid water which enhances deposition growth and riming of ice particles, as well as secondary ice production processes. In-situ and remote observations have shown that supercooled drops form thin layers at the top and inside of mid-level clouds [Raubert and Tokay, 1991; Verlinde et al., 2007; Luke et al., 2010; Morrison et al., 2012]. Based on three weeks of measurements from two imaging probes carried by the Met Office C-130 Hercules research aircraft, Hogan et al. [2003] studied the liquid fraction within thin mixed-phase clouds at temperatures from  $-23$  to  $-7$  °C. The authors reported liquid water content (LWC) and effective radius of supercooled drops to be on the order of  $0.05$ – $0.1$   $\text{g m}^{-3}$  and  $3$ – $5$   $\mu\text{m}$ , respectively. Those obtained by Korolev et al. [2003] from long-term airborne observations are  $0.02$ – $0.1$   $\text{g m}^{-3}$  and  $15$   $\mu\text{m}$ , respectively. Even though indications of ice-dependent freezing at mid-levels were reported by Sassen and Khvorostyanov [2008], the majority of the ice crystals in mixed-phase clouds are formed heterogeneously within the liquid layer [Ansmann et al., 2009; De Boer et al., 2011]. Westbrook and Illingworth [2011] reported that about 95 % of ice particles at temperatures warmer than  $-20$  °C originated

from liquid water particles. The transition from the liquid phase to the ice phase and its partitioning depends strongly on the environmental temperature and, as it was previously mentioned, the properties of the available INP [DeMott *et al.*, 2010; Hoose and Möhler, 2012; Kanitz *et al.*, 2011; Seifert *et al.*, 2015]. Temperature, pressure, and humidity at which ice crystals are formed also define their shape and apparent density, which in turn determine the sedimentation velocity [Fukuta and Takahashi, 1999; Bailey and Hallett, 2009]. The vertical and dynamical structure of a mixed-phase cloud furthermore determines the type and intensity of ice multiplication processes whose occurrence are a prerequisite for the formation of intensive precipitation [Hallett, 1974; Rangno and Hobbs, 2005; Seifert and Beheng, 2006]. Korolev *et al.* [2007] analyzed 584 profiles of liquid water content measured in situ. The authors found that the thickness of supercooled liquid layers in mixed-phase clouds often exceeds 100 m. Having terminal velocities on the order of  $10^{-1} \text{ m s}^{-1}$  [Fukuta and Takahashi, 1999], newly formed ice particles can grow under water saturation conditions for several tens of minutes.

## 2.2 Laboratory investigations of ice crystal development

At atmospheric pressures and temperatures in the range from  $-80$  to  $0$  °C bonded water molecules are arranged into hexagonal structures (ice Ih) [Pruppacher and Klett, 1997, ch. 3]. Pristine ice crystals observed in situ in the atmosphere and grown in laboratories often have a shape of hexagonal columns and plates or six-branched dendrites [Kampe *et al.*, 1951; Fukuta, 1969; Lamb and Hobbs, 1971; Ryan *et al.*, 1976; Keller and Hallett, 1982; Takahashi *et al.*, 1991; Bailey and Hallett, 2009; Castellano *et al.*, 2014]. Therefore, pristine ice particles are often represented by a hexagonal prism which has two basal and six prism faces. Basal and prism faces are, using Miller-Bravais index, often denoted as  $\{0001\}$  and  $\{1010\}$ , respectively, in above-cited literature. Throughout this thesis the shape of an ice crystal is characterized by the axis ratio:

$$\xi_g = \frac{c}{a}, \quad (2.1)$$

where  $a$  and  $c$  are width and height of the ice crystal, respectively. In the case of the hexagonal approximation,  $a$  and  $c$  correspond to the diameter of the circle circumscribing a basal face and the distance between basal faces of the prism, respectively.

Laboratory studies show a strong dependence of ice crystal growth on temperature and saturation conditions. Different temperature–growth rate dependencies for basal and prism faces result in changes of the ice crystal habit. Airborne in situ observations indicate that similar dependencies can occur in clouds [Fleishauer *et al.*, 2002]. Kuroda and Lacmann [1982] explained the temperature dependence of ice crystal shape by different surface kinetic growth mechanisms. The dominant mechanisms for the growth of a hexagonal prism at certain temperatures are presented in Table 2.1. In the range from  $-4$  to  $0$  °C basal and

prism faces grow via the Vapor–Quasi-Liquid–Solid mechanism (V–QL–S). This mechanism includes two phase transitions. Water vapor continuously condenses onto the quasi-liquid layer at the surface of an ice crystal. At the same time, water directly contacting with the surface of the ice crystal freezes. *Gibbs* [1878] found that a crystal formed from a fluid has a shape corresponding to the minimum of the free energy:

$$\Delta G = \sum \Delta G_i = \sum \sigma_i s_i, \quad (2.2)$$

where  $\Delta G_i$  is the work required to form the  $i$ -th surface of the crystal,  $\sigma_i$  is the work spent in forming a unit of the  $i$ -th surface, and  $s_i$  is the area of the  $i$ -th surface. Since for the V–QL–S mechanism  $\Delta G_{0001} > \Delta G_{1010}$ , the growth rate of prism faces is higher. *Lamb and Hobbs* [1971] experimentally estimated the linear growth rates of basal and prism faces at supersaturation around 1.3 Pa. Under such low supersaturation the growth is dominated by molecular events at the crystal surface, while deposition growth has negligible influence [*Pruppacher and Klett*, 1997, ch. 13]. The growth rates of basal and prism faces at  $-4$  °C were found to be  $\sim 0.3$  and  $\sim 0.7$   $\mu\text{m s}^{-1}$ , respectively. Thus, a formed ice crystal likely has a platelike shape. At temperatures from  $-10$  to  $-4$  °C prism faces still grow via the V–QL–S mechanism. At the same time, the adhesive mechanism becomes dominant for basal faces. Water molecules are strongly adsorbed onto the rough (at a molecular level) surface of the crystal. The rate of the adhesive mechanism is higher than the one of V–QL–S. At  $-6$  °C growth rates of basal and prism faces are  $\sim 0.7$  and  $\sim 0.4$   $\mu\text{m s}^{-1}$ , respectively. Therefore, columnar ice crystals are formed. In the temperature range from  $-20$  to  $-10$  °C basal faces grow via adhesive mechanisms, while two-dimensional nucleation of water vapor plays the major role in the growth of prism faces. The rate of two-dimensional nucleation is about one order of magnitude lower than the one of the adhesive mechanism. This results in up to  $0.5$   $\mu\text{m s}^{-1}$  growth of prism faces while the growth rate of basal faces is lower than  $0.1$   $\mu\text{m s}^{-1}$ . This difference causes the formation of ice plates. At temperatures below  $-20$  °C all faces of an ice crystal grow via the two-dimensional nucleation mechanism. This mechanism is characterized by higher values of free energy  $\Delta G_{0001}$  in comparison with  $\Delta G_{1010}$  at temperatures down to  $-32$  °C, which leads to platelike crystals. At lower temperatures  $\Delta G_{0001} \approx \Delta G_{1010}$ .

Even though surface kinetic mechanisms are responsible for the general shape formation, they can only produce hexagonal-shaped ice crystals with axis ratios that do not differ from unity significantly. At the same time, axis ratios of ice crystals observed in laboratories often reach values down to 0.01 for platelike crystals and up to 10 for columnar-shaped particles [*Takahashi et al.*, 1991]. After the ice particle is formed via a surface kinetic mechanism, the subsequent geometry development is mainly driven by the diffusional growth, especially at high supersaturations. The diffusional growth is not only responsible for axis ratios that are much higher or much lower than unity, but also for the presence of columnar-

**Table 2.1:** Growth kinetic processes of hexagonal prisms as a function of temperature. Adopted from *Kuroda and Lacmann* [1982]. V-QL-S stands for Vapor-Quasi-Liquid-Solid mechanism.

Surface	Temperature			
	$-4...0$ °C	$-10...-4$ °C	$-20...-10$ °C	$<-20$ °C
{0001}	V-QL-S	Adhesive growth	2D nucleation growth	2D nucleation growth
{1010}	V-QL-S	V-QL-S	Adhesive growth	2D nucleation growth

shaped ice crystals at temperatures below  $-20$  °C [*Kuroda and Lacmann*, 1982]. At high supersaturations the morphological instability of ice crystals leads to preferred growth of edges and corners [*Yokoyama and Kuroda*, 1990]. This results in branched structures and hollow fillings in ice crystals [*Kuroda*, 1983]. A detailed review of processes involved in the growth of ice crystals is given by *Libbrecht* [2005].

## 2.3 Polarimetric radar observations of ice microphysics in the atmosphere

As it was shown in the previous section, the formation and growth processes of ice crystals under certain temperature and saturation conditions have been deeply investigated under laboratory conditions. Nevertheless, a direct application of this knowledge to numerical weather prediction and cloud-resolving models is limited because of a lack of continuous and accurate information on temperature, humidity, and dynamic structure of the atmosphere. There is no doubt that the constellation and determination of these parameters are much more complicated than of the respective parameters reproduced in laboratories. In addition, processes such as aggregation, riming, and splintering occurring in natural mixed-phase clouds make the investigation of microphysical properties of the ice phase even more complicated. These challenges drive the need for the development of retrieval techniques based on remote sensors that are sensitive to different physical properties of cloud particles. One instrument class, frequently applied in meteorological studies, is polarimetric radar. Proved efficiency of this instrument class led to the establishment of country-wide radar networks for weather monitoring. For instance, the American NEXRAD (Next-Generation Radar) and the European OPERA (The European Operational Program for Exchange of Weather Radar Information) networks contain 160 and 48 polarimetric weather radars, respectively [*Huuskonen et al.*, 2013].

### 2.3.1 Polarimetry in weather radar networks

Weather radars are usually operated at S, C, and X-frequency bands, corresponding to 3, 6, and 10 GHz, respectively. These instruments typically perform rapid scans in azimuth at low elevation angles in order to provide high temporal resolution and spatial coverage. Applications of weather radar polarimetry cover the following aspects:

- detection of severe hazards such as storms, strong rain and hail events, and tornadoes [Ryzhkov *et al.*, 2005b];
- quantitative precipitation estimation [Ryzhkov *et al.*, 2005a];
- classification of hydrometeors [Straka *et al.*, 2000; Park *et al.*, 2009];
- microphysical studies of liquid water and ice fractions [Kumjian and Ryzhkov, 2010, 2012; Kumjian *et al.*, 2012];
- identification of electrically active storms [Zrnica and Ryzhkov, 1999];
- ornithological and insect studies [Zrnica and Ryzhkov, 1998];
- mitigation of ground clutter and chaff contamination [Zrnica and Ryzhkov, 2004].

The basic operational principle of polarimetric weather radars implies the transmission of horizontally and vertically polarized pulses and the reception of horizontal and vertical components of the radiation returned from atmospheric scatterers. Using the radar equation for meteorological targets [Probert-Jones, 1964], the equivalent radar reflectivity factor at the horizontal polarization  $Z_h$  (hereafter denoted as radar reflectivity) is calculated from the signal-to-noise ratio in the horizontal channel  $\text{SNR}_h$ :

$$Z_h [\text{dBZ}] = 10 \log C_0 - 20 \log r_s + 10 \log \text{SNR}_h, \quad (2.3)$$

where  $C_0$  is a constant depending on radar parameters and the dielectric constant of water at the operation frequency and  $r_s$  is the distance between the radar and the scattering volume. The radar reflectivity is usually associated with the 6-th raw moment of the particle size distribution [Doviak *et al.*, 1979]. In the case of Rayleigh scattering, i.e. when particle sizes are much smaller than the radar wavelength  $\lambda$ , the radar reflectivity does not depend on the radar operation frequency.

Modern weather radars are coherent and, therefore, allow for registration of the complex amplitudes  $\dot{E}_h$  and  $\dot{E}_v$  of signals in the horizontal and vertical channels, respectively. These complex amplitudes are used for the calculation of differential reflectivity  $Z_{DR}$ , co-polar cross-correlation coefficient  $\rho_{hv}$  (further denoted as correlation coefficient), differential phase

---

shift  $\Phi_{DP}$ , specific differential phase shift  $K_{DP}$ , and backscattering differential phase shift  $\delta$ :

$$Z_{DR} = \frac{\langle \dot{E}_h \dot{E}_h^* \rangle}{\langle \dot{E}_v \dot{E}_v^* \rangle}, \quad (2.4)$$

$$\rho_{hv} = \frac{|\langle \dot{E}_h \dot{E}_v^* \rangle|}{\left( \langle \dot{E}_h \dot{E}_h^* \rangle \langle \dot{E}_v \dot{E}_v^* \rangle \right)^{1/2}}, \quad (2.5)$$

$$\Phi_{DP} = \arg(\langle \dot{E}_h \dot{E}_v^* \rangle), \quad (2.6)$$

$$K_{DP} = \frac{1}{2} \frac{d\Phi_{DP}}{dr_s}, \quad (2.7)$$

$$\delta = \Phi_{DP} - 2 \int K_{DP}(r_s) dr_s. \quad (2.8)$$

In Eqs. (2.4)–(2.6)  $\langle \rangle$  denotes averaging over a number of pulses,  $*$  is the complex conjugation sign. The given polarimetric radar products are sensitive to shape, orientation, dielectric properties, and concentration of hydrometeors and precipitation [Seliga and Bringi, 1978]. Theoretical dependencies of different polarimetric variables on the mentioned microphysical properties were given by Matrosov [1991a], Ryzhkov [2001], and Ryzhkov et al. [2002]. Decades of polarimetric observations and their comparison to the data collected from ground-based and airborne in situ instruments allowed for the development of empirical classification algorithms. For instance, rule-based and fuzzy logic algorithms used operationally in radar networks are able to classify atmospheric scatterers into a vast number of categories [Straka et al., 2000; Park et al., 2009]. A lot of effort has been put into scattering models, technical developments and calibration of radar hardware, and processing techniques. Knowledge on these topics was analyzed and summarized in the book of Bringi and Chandrasekar [2001].

In ice-focused studies of Hogan et al. [2002, 2003] and Field et al. [2004] polarimetric radar observations were combined with airborne in situ measurements. For their studies the authors applied a 3-GHz weather radar and analyzed only the radar reflectivity and the differential reflectivity. It was found that  $Z_{DR}$  values exceeding 3 dB, observed above the melting layer, are associated with the presence of supercooled liquid water. An indication that high  $Z_{DR}$  values correspond to pristine columnar or platelike ice crystals was shown. The authors suggested that high values of the differential reflectivity occur when the depositional growth dominates over aggregation, which could be valid for the upper part of a cloud. A spheroidal model was used in order to estimate a range of differential reflectivity produced by prolate (columnlike) and oblate (platelike) ice crystals. The results showed that prolate particles cannot induce  $Z_{DR}$  exceeding 4 dB. Usually, ice clouds produce  $Z_{DR}$  less than 0.5 dB caused either by axis ratios close to unity or by the low dielectric constant of an air-ice mixture of particles. The authors concluded that often high  $Z_{DR}$  values of small pristine ice particles can be suppressed by the presence of large aggregates dominating the backscattered signal. Backscattering differential phase shift  $\delta$  and specific differential phase



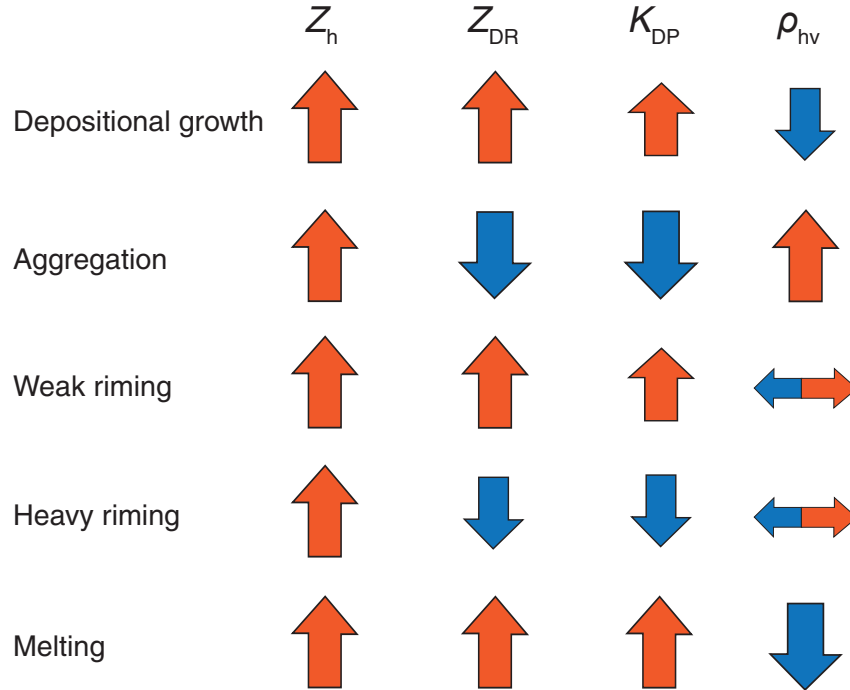


**Figure 2.2:** Polarimetric fingerprints for microphysical processes of ice phase development. The direction of arrows shows the change in the polarimetric variable while the size of the arrow indicates the magnitude of the change relative to other variables for the certain process. Bi-directional arrows represent possible changes in both directions. The figure is based on *Kumjian [2012]*.

shift  $K_{DP}$  at S, C, and X frequencies are self-consistent polarimetric parameters which can be used for the investigation of liquid [*Otto and Russchenberg, 2011*] and ice phases [*Trömel et al., 2013*] in deep-precipitating clouds.

Studies of microphysical processes occurring in cloud systems are often based on the comparison of observed polarimetric variables with those calculated with cloud models. A detailed evaluation of modeled and measured vertical profiles of polarimetric variables for cloud microphysical processes has been performed by *Kumjian and Ryzhkov [2010, 2012]*, *Kumjian et al. [2012]*, and *Kumjian [2012]*. The authors showed that different processes lead to diverse changes in size, shape, orientation, and dielectric properties of hydrometeors. Thus, vertical changes of a set of polarimetric parameters (“fingerprints”) allow the detection of such processes as size-sorting, collision, evaporation, freezing, aggregation, and melting. Fingerprints for ice development mechanisms are shown in Fig. 2.2. It can be seen that radar reflectivity alone is not sufficient for the discrimination between different processes. Conversely, polarimetric variables contain more information and provide a good basis for studies of ice microphysics.

*Andrić et al.* [2013] employed a two-moment bulk model in order to reproduce values of radar reflectivity  $Z_h$ , differential reflectivity  $Z_{DR}$ , specific differential phase shift  $K_{DP}$ , and correlation coefficient  $\rho_{hv}$  produced by ice particles at S-band. The authors found that small quasi-spherical ice particles, also known as isometric, induce low values of  $Z_h$ ,  $Z_{DR}$ , and  $K_{DP}$  and high value of  $\rho_{hv}$ . In contrast, ice particles with platelike habits induce an increase in  $Z_{DR}$  and a decrease in  $\rho_{hv}$ . The authors claimed that such effects result from high particle density, very anisotropic shape, and a diversity of shapes and orientations. It was also shown that aggregation of particles leads to a decrease in differential reflectivity while radar reflectivity, correlation coefficient, and specific differential phase shift were increasing. Based on a sensitivity analysis, the authors emphasized that the used model cannot accurately reproduce all four parameters.

Based on the differential reflectivity and the correlation coefficient, *Melnikov and Straka* [2013] performed quantitative estimations of shape and orientation of ice particles. The authors modeled these polarimetric variables using the spheroidal approximation of scatterers. Applying a best-fit algorithm, the axis ratios and standard deviations of canting angles, i.e. the angles at which particles are wobbling along their horizontal axis, were estimated. Analyzing three cases collected by the dual-polarization S-band weather radar WSR-88D in Norman, Oklahoma, US, the authors retrieved axis ratios and standard deviations of canting angles in the range from 0.15 to 0.4 (oblate particles) and from  $2^\circ$  to  $20^\circ$ , respectively. It was assumed that the observed particles consisted of pure ice. However, this retrieval technique cannot be used to discriminate between oblate and prolate particles, and can therefore only be applied when  $Z_{DR}$  values are higher than 4 dB because, as it was mentioned before, such values can only be produced by oblate particles. The authors highlighted that the accurate determination of shape requires scans in elevation direction which were not available for their study.

In spite of the effort put by the weather radar community into the development of new retrieval methods, their improvement is often limited by strict operational modes of the radars. For instance, elevation scans are usually restricted to several degrees close to the ground. Fast azimuthal rotation rates limit the Doppler resolution of the retrieved spectra. These problems can be overcome with cloud radars which are not widely used for weather monitoring but usually employed at research facilities for microphysical studies of cloud particles. Therefore, the operational strategies including scanning regimes are much more flexible in the latter case.

### 2.3.2 Polarimetry in cloud radars

Cloud radar is an important tool for active remote sensing of atmospheric hydrometeors. Measurements from cloud radars, which are typically operated at Ka- ( $\sim 35$  GHz) or W-band ( $\sim 94$  GHz) frequencies, are nowadays widely used, often in combination with other active and

---

passive remote-sensing instruments, for retrieving cloud microphysical and macrophysical properties [Illingworth *et al.*, 2007; Kollias *et al.*, 2007; Shupe *et al.*, 2008]. Main advantages of cloud radars are defined by their short operational wavelength [Kollias *et al.*, 2007]. A high sensitivity of cloud radars is caused by the  $\lambda^{-4}$  proportionality of the particle's radar cross section. At shorter wavelengths a smaller antenna is required to get a certain gain and beam-width. In addition, cloud radars typically sense the atmosphere at distances shorter than 15 km. At such ranges even signal generators with 1–30 W of mean power permit achieving high sensitivity at Ka and W-band. Having respectively low mass and geometrical dimensions, cloud radars are often employed at mobile platforms and satellites.

As it was mentioned before, polarimetric radar methods have shown their efficiency in meteorological studies. Modern cloud radars often have polarization capabilities. Many commercially produced cloud radars operate in the linear-depolarization-ratio (LDR) mode. In this mode the radar transmits electromagnetic waves with a horizontal polarization state and receives both horizontal and vertical polarization components of the scattered wave in the co- and cross-channel, respectively. LDR is calculated using received powers  $P_c$  and  $P_x$  in the co- and cross-channel, respectively:

$$\text{LDR} = \frac{P_x}{P_c}. \quad (2.9)$$

Zenith observations in LDR mode permit a reliable detection of the melting layer [Zrnica *et al.*, 1994; Lohmeier *et al.*, 1997; Di Girolamo *et al.*, 2012] and multiple-scattering effects [Battaglia *et al.*, 2007, 2010], and distinguishing between cloud and insect echoes [Martner and Moran, 2001]. When measurements of the phase relations between signals in the radar polarimetric channels in the LDR mode are available, a cross-correlation coefficient  $\rho_{cx}$  can be calculated:

$$\rho_{cx} = \frac{|\langle \dot{E}_c \dot{E}_x^* \rangle|}{\left( \langle \dot{E}_c \dot{E}_c^* \rangle \langle \dot{E}_x \dot{E}_x^* \rangle \right)^{1/2}}, \quad (2.10)$$

where  $\dot{E}_c$  and  $\dot{E}_x$  are the complex amplitudes of the received signals in the co- and cross-channel, respectively. This parameter (denoted as the co-cross-correlation coefficient in Ryzhkov [2001]) contains additional information about meteorological scatterers such as the mean axis ratio and parameters describing the orientation distribution of the scatterers [Ryzhkov, 2001]. However, the cross-correlation coefficient  $\rho_{cx}$  is also influenced by the polarimetric properties of the radar hardware [Galletti *et al.*, 2014b]. At the same time the applicability of the LDR mode for the shape estimation is limited because of its high sensitivity to the orientation of cloud particles [Matrosov *et al.*, 2001]. Based on modeling results the author claims that LDR can vary by up to 10 dB solely due to a variation of the canting angle for a given shape.

---

*Pazmany et al.* [1994] used a ground-based W-band cloud radar with agile polarization mode. In this mode a radar transmits pulses with vertical and horizontal polarization consecutively and receives both vertical and horizontal components of the returned signal simultaneously. This configuration allowed the authors to measure polarimetric variables such as differential reflectivity, correlation coefficient, degree of polarization, and linear depolarization ratio. *Galloway et al.* [1997] conducted the first airborne measurements using an agile-mode W-band cloud radar. The radar was installed on board the King Air research aircraft of the University of Wyoming. The authors presented polarimetric observations for the melting layer, needle-shaped ice crystals, and a snowstorm case. It was reported that interpretation of the set of polarimetric variables can be useful for the estimation of ice particle shape and orientation. Polarimetric observations and in situ measurements from the research aircraft were later used by *Aydin and Singh* [2004] for the development of an ice classification algorithm. Based on radar reflectivity, differential reflectivity, and linear depolarization ratio, the authors classified ice particles into five categories: columnar crystal, planar crystals, mixture of small planar, aggregates, and rimed particles, medium to large aggregates, and graupel. A validation of the retrieval algorithm with imaging probes showed  $\sim 90\%$  agreement. Even though the agile polarization configuration showed high efficiency for ice typing, its implementation is more expensive in comparison with other configurations.

*Reinking et al.* [2002] evaluated a ground-based W-band cloud radar with slanted LDR configuration (SLDR) which was implemented based on the conventional LDR mode by  $45^\circ$  rotation of the antenna system around the emission direction. The authors highlight easy implementation of this mode, several dB higher signal in the cross-channel, and low sensitivity to orientation of particles. *Matrosov et al.* [2012] showed the applicability of the SLDR mode for the classification of ice crystals in winter clouds. The authors presented elevation scans of SLDR and their interrelation to the ice crystals observed in situ at the ground. Analyzed cases included drizzle, graupel, dendrites, rimed ice particles, and aggregates.

A number of studies was devoted to cloud radars with circular depolarization mode [*Matrosov*, 1991a; *Martner and Moran*, 2001; *Galletti et al.*, 2014a]. The main advantage of this polarimetric configuration is that the measured circular depolarization ratio is not significantly influenced by the mean orientation angle of aligned scatterers such as insects or ice crystals in electrified clouds [*Galletti et al.*, 2014a]. *Matrosov and Kropfli* [1993] showed the applicability of elliptical polarization of the transmitted signal for the investigation of ice particle shape and common orientation.

In this work a cloud radar with hybrid polarization configuration was used. This mode allows for changing the polarization of the transmitted signal. By adjusting phase relations between the transmitting channels, it is possible to implement  $45^\circ$  linear, circular, and elliptical polarizations. Details about the utilized cloud radar are given in Chapter 4.

---

### 2.3.3 Polarization coupling

One of the main challenges for polarimetric observations in all polarimetric configurations is the polarization coupling (or leakage) which occurs in the waveguide transmission line, the orthomode transducer, and the antenna (further all the mentioned parts are denoted as the antenna system) because radar hardware is never ideal. A fraction of the signal received in a polarization channel leaks into another one and vice-versa. This effect determines biases in polarimetric variables which vary from radar to radar depending on hardware characteristics [Chandrasekar and Keeler, 1993; Mudukutore *et al.*, 1995]. This leads to the fact that polarimetric variables, which are observed from hydrometeor populations with the same microphysical properties, will differ for different radars. Thus, the polarization coupling complicates the interpretation and intercomparison of polarimetric measurements [Zrnić *et al.*, 2010].

The antenna system influence on radar polarimetric measurements has been investigated in a number of studies. For instance, Chandrasekar and Keeler [1993] performed a theoretical study of the errors introduced by complex antenna patterns on the measurements of LDR, differential reflectivity, and differential phase shift. These authors, however, considered only measurements of the amplitude antenna patterns and defined the accuracy bounds for the radar variables mentioned above. Mudukutore *et al.* [1995] described a technique for measurements of the differential-phase antenna pattern and investigated the influence of this pattern on the differential phase shift and the correlation coefficient measured with weather radars that operate with pulse-to-pulse switching of the transmitted polarization state [Bringi and Chandrasekar, 2001]. Bringi and Chandrasekar [2001] provide a review of different studies focusing on antenna influences on polarimetric variables in different radar configurations. Zrnić *et al.* [2010] considered the influence of a bias in  $Z_{DR}$  produced by the antenna on rain-rate estimations. Frech *et al.* [2013] conducted measurements of amplitude and phase antenna patterns in order to estimate the influence of a radome on polarimetric observations with weather radars.

It was shown in Kanareykin *et al.* [1968] that the basis of the electromagnetic wave coherency matrix can be changed by applying the unitary matrix transformation in such a way that the orthogonal components of the wave are not correlated. This transformation is known as the second specific basis of the coherency matrix [Kanareykin *et al.*, 1968]. The effectiveness of this transformation for the correction of the coherent coupling was recently shown [Galletti, 2013; Galletti *et al.*, 2014b]. It is noted that non-coherent leakage cannot be removed with this method.

---

## 2.4 Aims and scientific questions

The literature review given in this chapter showed that polarimetric cloud radars provide the potential for a continuous quantitative characterization of ice particles' shape. However, an accurate shape retrieval requires radar-related studies. First, biases associated with the polarimetric performance of the antenna system have to be investigated. Chapter 3 covers comprehensive antenna pattern measurements, which are necessary to understand the nature of the biases, and for the development of a correction algorithm. Second, a cloud radar with a new polarimetric scheme is necessary in order to get polarimetric variables, based on which the shape retrieval can be developed. Implementation of the new cloud radar and its calibration for the polarization coupling and differences in amplification and electrical path lengths of polarization channels are described in Chapter 4. Third, based on corrected polarimetric variables, a technique for the shape characterization is established in Chapter 5.

Analysis of ice particles observed remotely in the atmosphere and those grown under laboratory conditions allows for answering the following questions:

1. Is there a way to compare microphysical properties such as shape and apparent density of ice crystals grown in the atmosphere and under laboratory conditions?
2. Are temperature dependencies of the shape and apparent ice density of ice crystals grown at water saturation in the atmosphere similar to those found under laboratory conditions (see Sec. 2.2)?
3. Can ice crystals at the top of mixed-phase clouds be considered as pristine?

Addressing these questions requires observations of mixed-phase clouds not only with the cloud radar but also with a variety of other active and passive instruments. In Chapter 6 a detailed analysis of distinctive cases obtained during the ACCEPT campaign is shown and the comparison of remote observations with laboratory findings is presented.

---

## Chapter 3

# Effects of antenna patterns on cloud radar polarimetric measurements

As it was mentioned in the previous chapter the polarization coupling is an important problem in radar polarimetry. Accurate and reliable retrieval techniques as well as comparability can only be based on variables corrected for the coupling effects. This chapter is based on the published paper of *Myagkov et al.* [2015] and presents an experimental analysis of antenna system effects on polarimetric measurements conducted with cloud radars operating in the LDR mode. Notations were adapted to this thesis. The chapter is organized as follows. Section 3.1 contains theoretical considerations to describe the antenna system patterns, the description of the instrumentation, and the measurement results. The application of the coherency matrix for the correction of LDR and the cross-correlation coefficient is shown in section 3.2. Discrimination between point and volume-distributed targets using the cross-correlation coefficient is presented in section 3.3.

### 3.1 Measurements of complex antenna patterns

For this study cloud radars of the type MIRA-35 were used. MIRA-35 is a magnetron-based 35-GHz cloud radar produced by METEK GmbH, Elmshorn, Germany. Several measurement sites in Europe operate radars of this type in the framework of Cloudnet, which is part of the “Aerosols, Clouds and Trace gases Research Infrastructure” (ACTRIS), because of their high sensitivity and reliability [*Illingworth et al.*, 2007; *Martucci and O’Dowd*, 2011; *Di Girolamo et al.*, 2012; *Bühl et al.*, 2013; *Löhnert et al.*, 2015]. *Görsdorf et al.* [2015] describe the technical implementation of MIRA-35. Recently, a MIRA-35 was installed on board of the research aircraft HALO [*Mech et al.*, 2014]. Main operational parameters of MIRA-35 are listed in Table 3.1.

---

**Table 3.1:** Parameters of MIRA-35 used in the operational mode. FFT is Fast Fourier Transformation.

Peak power [kW]	30
Pulse length [ns]	200
Pulse repetition frequency [kHz]	5
Minimum range [km]	0.15
Maximum range [km]	15
Range resolution [m]	30
Number of pulses for FFT	256
Number of spectra for averaging	200
Sensitivity at 5 km [dBZ]	-55

### 3.1.1 Problem definition

Any polarization analysis requires a choice of the reference polarization basis. Usually, the orthogonal linear basis formed by two unit vectors defined by the antenna feeders is used. Generally, unit vectors of the basis correspond to the horizontal and vertical polarization states. Figure 3.1 illustrates the polarization basis ( $\mathbf{e}_h$   $\mathbf{e}_v$ ) used throughout the thesis. Indexes  $h$  and  $v$  denote horizontal and vertical directions, respectively.

In the LDR mode used by many cloud radars, the horizontal component of the wave is received in the co-channel of the radar and the vertical one is received in the cross-channel.

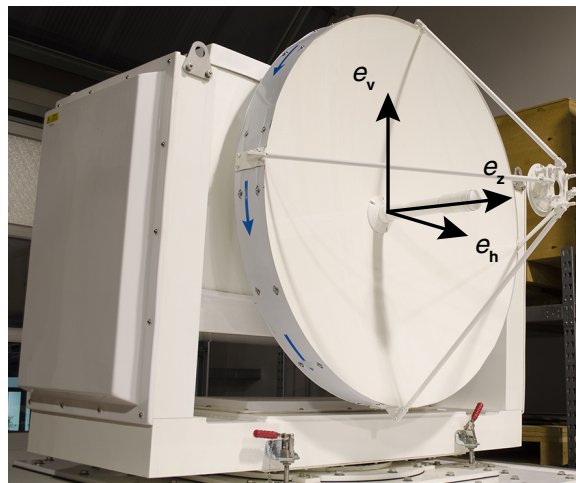


**Figure 3.1:** Antenna of the MIRA-35 system mounted on the scanning unit. The description polarization basis is shown. The unit vector  $\mathbf{e}_z$  shows the propagation direction of the transmitted radiation.



Further, the co- and cross-channels are denoted by indexes  $c$  and  $x$ , respectively. The complex amplitudes of the received pulses in the co- and cross-channels can be described by:

$$\dot{E}_c = E_c \exp(i\Phi_c), \quad (3.1)$$

$$\dot{E}_x = E_x \exp(i\Phi_x), \quad (3.2)$$

where  $E_c$ ,  $\Phi_c$  and  $E_x$ ,  $\Phi_x$  are amplitudes and phases of the received pulses in the co- and cross-channels, respectively. The dot over an identifier letter hereafter represents a complex quantity.

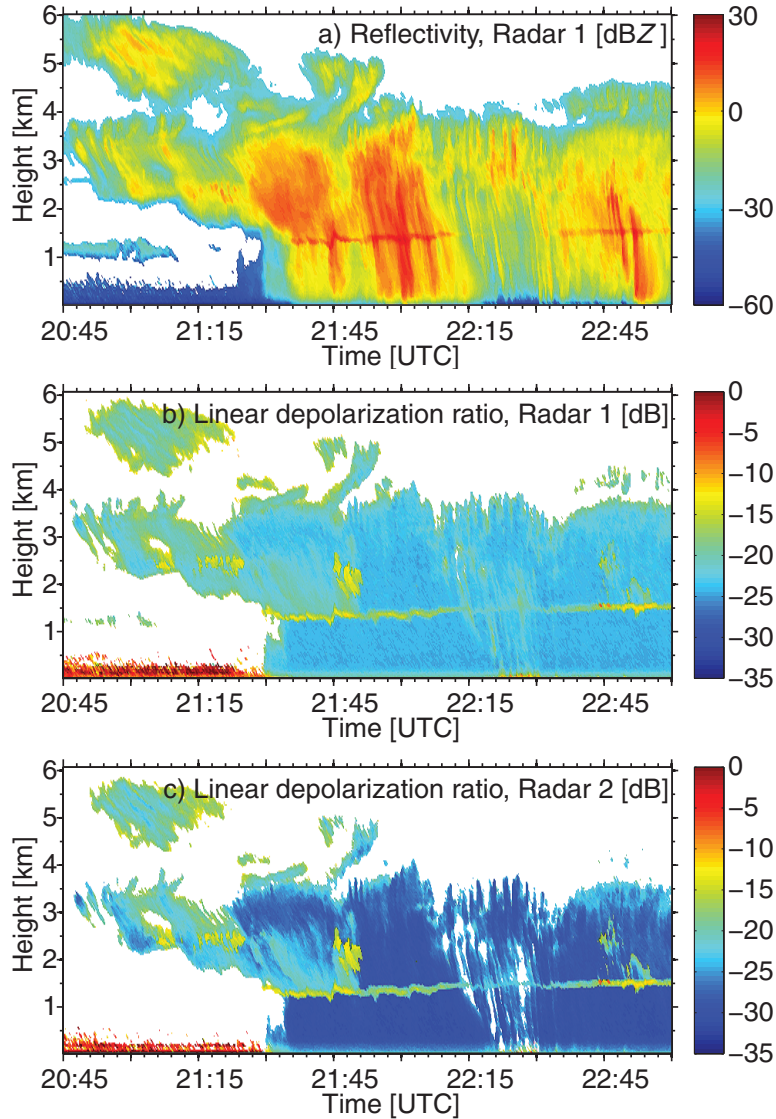
The polarimetric parameter LDR introduced in Eq. (2.9) can be written as follows:

$$\text{LDR} = \frac{\langle E_x^2 \rangle}{\langle E_c^2 \rangle}. \quad (3.3)$$

In the following, linear scales of LDR are applied in equations, while logarithmic scales expressed in decibels are used for values in figures and discussion. Scatterers with the unity backscattering matrix are denoted as isotropic particles. Note, that not only spherical scatterers but also horizontally aligned oblate spheroids and plates can be considered as isotropic when observed by a vertically pointed radar. Even though the theoretical value of LDR in the logarithmic scale for isotropic particles is  $-\infty$ , the measured values are always finite and depend on radar hardware and noise.

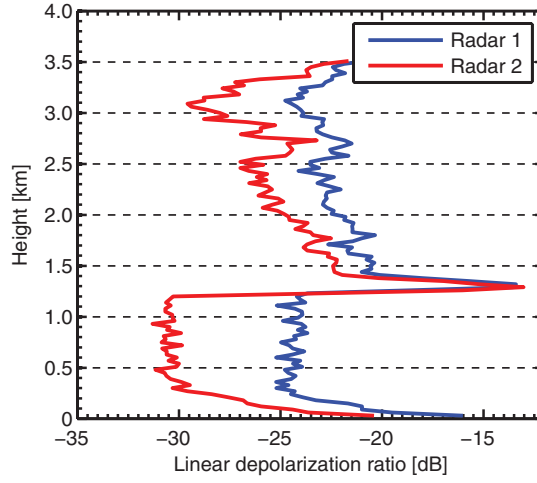
Fig. 3.2 shows the radar reflectivity and LDR obtained with two co-located vertically pointed MIRA-35 cloud radars that were tested at the METEK site. We denote these radars as “Radar 1” and “Radar 2”. The distance between the radars was about 30 meters. A precipitating cloud system which passed over the METEK site was simultaneously observed by both radars. The melting layer, indicated by a region of increased reflectivity and LDR, can be seen at heights between 1.3 and 1.5 km when clouds were present. Reflectivity values of approximately 30 dBZ observed below the melting layer correspond to light rain [Straka *et al.*, 2000]. For vertically viewing cloud radars, the polarimetric variables of raindrops can be described by a population of particles with isotropic polarimetric scattering properties. Therefore, this measurement case was chosen for the comparison of minimal LDR values.

Fig. 3.2-b and c show similar patterns of LDR for both radars. Nevertheless, the values of LDR are significantly different. In Fig. 3.3 the vertical profiles of LDR measured by both radars at 21:40 UTC are presented. It can be seen that the antenna system of Radar 1 results in minimal LDR values of about  $-25$  dB and that the antenna system of Radar 2 causes minimal LDR values of approximately  $-31$  dB. Below, the antennas of Radar 1 and Radar 2 will be denoted as “bad” and “good”, respectively. It can also be noticed that even though the minimal LDR differs for both systems, the LDR produced by the melting layer is approximately the same, because the signal in the cross-channel in this layer is mostly determined by scattering from melting particles and not by the polarization leakage.



**Figure 3.2:** Time-height cross sections of observed parameters, (a) reflectivity for Radar 1, (b) linear depolarization ratio for Radar 1, and (c) linear depolarization ratio for Radar 2, taken at Elmshorn, Germany, on 8 Nov 2013. The amount of data points in panel (c) is less in comparison with (b) because of lower sensitivity of Radar 2.

Another example of the antenna system influence on the polarimetric measurements is given by *Matrosov et al.* [2012] who evaluated the implementation of the slanted LDR mode (SLDR mode) into a cloud radar. The SLDR mode can be implemented starting from LDR mode by rotation of the radar antenna by  $45^\circ$ . The authors noticed that due to the antenna rotation the minimal LDR value increased compared to the minimal LDR value observed in LDR mode. Increased values of minimal LDR can mask less-pronounced depolarizing



**Figure 3.3:** Vertical profiles of the linear depolarization ratio for Radar 1 and Radar 2 on 8 Nov 2013, 21:40 UTC (the same case as in Fig. 3.2).

structures in the data. In addition, variations in the minimal LDR of different radar systems reduce the comparability of respective measurements of LDR.

In general, the full set of receiving antenna patterns can be presented in the matrix form:

$$\mathbf{F}(\theta, \phi) = \begin{pmatrix} \dot{f}_{cc}(\theta, \phi) & \dot{f}_{xc}(\theta, \phi) \\ \dot{f}_{cx}(\theta, \phi) & \dot{f}_{xx}(\theta, \phi) \end{pmatrix}, \quad (3.4)$$

where  $\dot{f}_{mn}(\theta, \phi)$  are complex antenna patterns. The first index  $m$  describes the polarization state of the wave incident on the antenna (either co- or cross-polarized), the second index  $n$  describes the polarization of the receiving channel, and  $\theta$  and  $\phi$  represent the azimuth and elevation angles, respectively, of the received wave with respect to the maximum of the radar beam.

The minimal LDR value for a particular radar is sometimes denoted as the integrated cross-polarization ratio (ICPR). *Chandrasekar and Keeler [1993]* showed that ICPR can be calculated from the antenna patterns. In terms of the receiving antenna patterns (Eq. (3.4)) ICPR can be written as follows:

$$\text{ICPR} = \frac{\int |\dot{f}_{cc}(\theta, \phi)\dot{f}_{cx}(\theta, \phi) + \dot{f}_{xc}(\theta, \phi)\dot{f}_{xx}(\theta, \phi)|^2 d\Omega}{\int |\dot{f}_{cc}^2(\theta, \phi) + \dot{f}_{xc}^2(\theta, \phi)|^2 d\Omega}, \quad (3.5)$$

where  $d\Omega$  is the elemental solid angle and the integration is performed over the  $4\pi$  solid angle.

Eq. (3.5) can be represented as the integral over a sum of three components:

$$H_1 = \frac{|\dot{f}_{cc}(\theta, \phi)|^2 |\dot{f}_{cx}(\theta, \phi)|^2}{\int |\dot{f}_{cc}^2(\theta, \phi) + \dot{f}_{xc}^2(\theta, \phi)|^2 d\Omega}, \quad (3.6)$$

$$H_2 = \frac{|\dot{f}_{xc}(\theta, \phi)|^2 |\dot{f}_{xx}(\theta, \phi)|^2}{\int |\dot{f}_{cc}^2(\theta, \phi) + \dot{f}_{xc}^2(\theta, \phi)|^2 d\Omega}, \quad (3.7)$$

$$H_3 = \frac{2\text{Re} \left( \dot{f}_{cc}(\theta, \phi) \dot{f}_{cx}^*(\theta, \phi) \dot{f}_{xc}(\theta, \phi) \dot{f}_{xx}^*(\theta, \phi) \right)}{\int |\dot{f}_{cc}^2(\theta, \phi) + \dot{f}_{xc}^2(\theta, \phi)|^2 d\Omega}, \quad (3.8)$$

It can be seen from Eqs. (3.6) and (3.7) that the calculation of the components  $H_1$  and  $H_2$  does not require complex antenna patterns. The phase relations appear only in  $H_3$ .

Using the approach of *Chandrasekar and Keeler* [1993] and taking into account that  $|\dot{f}_{xc}(\theta, \phi)| \ll |\dot{f}_{cc}(0, 0)|$  the bias in the correlation coefficient due to the polarization leakage can be written as follows:

$$\rho_b = \frac{\left| \int \left[ \dot{f}_{cc}(\theta, \phi)^3 \dot{f}_{cx}(\theta, \phi) + \dot{f}_{cc}(\theta, \phi)^2 \dot{f}_{xc}(\theta, \phi) \dot{f}_{xx}(\theta, \phi) \right] d\Omega \right|}{\left[ \int |\dot{f}_{cc}(\theta, \phi) \dot{f}_{cx}(\theta, \phi) + \dot{f}_{xc}(\theta, \phi) \dot{f}_{xx}(\theta, \phi)|^2 d\Omega \int |\dot{f}_{cc}^2(\theta, \phi)|^2 d\Omega \right]^{1/2}}. \quad (3.9)$$

We further introduce the following parameters:

$$R_1 = \frac{\text{Re} \left\{ \left[ \dot{f}_{cc}(\theta, \phi)^3 \dot{f}_{cx}(\theta, \phi) + \dot{f}_{cc}(\theta, \phi)^2 \dot{f}_{xc}(\theta, \phi) \dot{f}_{xx}(\theta, \phi) \right] \right\}}{\left[ \int |\dot{f}_{cc}(\theta, \phi) \dot{f}_{cx}(\theta, \phi) + \dot{f}_{xc}(\theta, \phi) \dot{f}_{xx}(\theta, \phi)|^2 d\Omega \int |\dot{f}_{cc}^2(\theta, \phi) + \dot{f}_{xc}^2(\theta, \phi)|^2 d\Omega \right]^{1/2}}, \quad (3.10)$$

$$R_2 = \frac{\text{Im} \left\{ \left[ \dot{f}_{cc}(\theta, \phi)^3 \dot{f}_{cx}(\theta, \phi) + \dot{f}_{cc}(\theta, \phi)^2 \dot{f}_{xc}(\theta, \phi) \dot{f}_{xx}(\theta, \phi) \right] \right\}}{\left[ \int |\dot{f}_{cc}(\theta, \phi) \dot{f}_{cx}(\theta, \phi) + \dot{f}_{xc}(\theta, \phi) \dot{f}_{xx}(\theta, \phi)|^2 d\Omega \int |\dot{f}_{cc}^2(\theta, \phi) + \dot{f}_{xc}^2(\theta, \phi)|^2 d\Omega \right]^{1/2}}. \quad (3.11)$$

Integrating the components  $H_{1,2,3}$  and  $R_{1,2}$  over specific areas of the antenna patterns can indicate where most of the coupling between the co- and cross-channel comes from.

Antenna manufacturers usually provide only information about two amplitude cut planes,  $|\dot{f}_{cc}(\theta, 0)|$  and  $|\dot{f}_{cc}(0, \phi)|$ , which is not sufficient for the analysis of the antenna system influence on polarimetric variables. Therefore, measurements of the complex antenna pattern were performed for two different antennas with good and bad polarimetric characteristics, respectively.

### 3.1.2 Measurement description

The antenna pattern measurements were performed as described by *Chandrasekar and Keeler* [1993] and *Mudukutore et al.* [1995]. The field experiment was conducted at the Hungriger Wolf airport near Hohenlockstedt (53.993°N, 9.577°E), Germany, during the period from 28 January 2014 to 1 February 2014. The cloud radar MIRA-35, denoted as Radar 1 in Subsection 3.1.1, was used for the measurements. The radar was equipped with a scanning



**Figure 3.4:** The MIRA-35 cloud radar with the scanning unit at METEK GmbH. The photo was provided by METEK GmbH.

unit (Fig. 3.4) based on drives of type Aerotech AGR200 with high gear ratio. The scanning unit allows changing the azimuth angle between  $0^\circ$  and  $360^\circ$  and the elevation angle between  $0^\circ$  and  $180^\circ$  with a resolution of  $0.034^\circ$ . Two different Cassegrain dual reflector antennas were taken for the measurements. They were denoted as “bad” and “good” antennas in Subsection 3.1.1. Both antennas were installed to the same transceiver unit of Radar 1. The antenna specifications as provided by the manufacturer are listed in Table 3.2.

In general, the moments of the Doppler spectra measured with MIRA-35 are used to de-

**Table 3.2:** Specification of used antennas. OMT is an orthomode transducer

Type	Cassegrain
Dish	Parabolic
Feed design	Center-fed
Number of struts	4
Diameter [m]	1
Weight [kg]	21.5
Operation band [GHz]	35.1 – 35.3
Gain [dB]	49.2
Beam width [°]	0.6
Sidelobes [dB]	$< -18$
Voltage standing wave ratio	$< 1.33$
OMT coupling [dB]	$-36$

rive information about cloud properties. The phase relations between co- and cross-channels are not saved. Nevertheless, the receiver unit of the radar allows saving in-phase ( $I$ ) and quadrature ( $Q$ ) components of the received signal in both polarization channels. The quadrature components make it possible to obtain not only the amplitude of the signals but also their phase. Therefore, during the antenna pattern measurements the radar was operating in the receiving mode (the transmitter unit was turned off) and the receiving antenna patterns were measured, by means of the  $I/Q$  components, consecutively with the good and the bad antennas.

A custom-made test transmitter was used for generation of the continuous wave at Ka-band. The test transmitter consists of a continuous-wave X-band generator with software-based frequency control, a 4-times frequency multiplier, and an antenna system based on a pyramidal horn antenna. The horn antenna forms a linearly polarized wave. As the antenna system of the test transmitter allows for rotation of the horn, it is possible to change manually the orientation angle  $\beta$  in the polarization plane of the transmitted wave with respect to the unit vector  $\mathbf{e}_h$  of the radar polarization basis. The output power of the test transmitter is 4 mW.

Basically, the bi-static measurements of the absolute phase require high stability of the local oscillators of transmitter and receiver. The local oscillators that are used in the radar receiver and the test transmitter are based on quartz resonators and cannot be used for long-term phase measurements due to the frequency drift. The short-term stability (Allan deviation over 1 s) of quartz resonators is of the order of  $10^{-9}$  [Vig, 1992], which allows performing phase measurements only for short time periods as the local oscillators can be assumed coherent in this case. Therefore, only the phase differences between polarization channels were calculated in addition to the amplitudes. Moreover, the absolute phases are not necessary for the modeling of scattering properties of meteorological scatterers because scattering is non-coherent in this case. The antenna measurement at  $\beta = 0^\circ$ , when the transmitted wave is horizontally polarized, gives the information about amplitude and phase relations between the elements  $\dot{f}_{cc}(\theta, \phi)$  and  $\dot{f}_{cx}(\theta, \phi)$ . The information about the elements  $\dot{f}_{xc}(\theta, \phi)$  and  $\dot{f}_{xx}(\theta, \phi)$  can be obtained at  $\beta = 90^\circ$ . As the measurements are not coherent over long time periods, a third measurement at  $\beta = 45^\circ$  is necessary to get the correct phase difference between the measurements at  $\beta = 0^\circ$  and  $\beta = 90^\circ$ .

The test transmitter was mounted at the airport tower at about 12 m height above ground. To minimize reflections from the tower the antenna of the test transmitter was installed 1 m away from the tower walls by mounting it on a wooden bar. The radar was placed 600 m away from the tower to ensure that the test transmitter was within the far field of the radar antenna, which starts at 235 m distance. Before the measurements, the radar antenna angular position with the maximum received power was determined. At this position it is assumed that  $\theta = 0^\circ$  and  $\phi = 0^\circ$ . Then the test transmitter horn was manually

---

rotated to the position where the measured LDR was minimal. This angular position of the horn was assumed to correspond to  $\beta = 0^\circ$ . The frequency of the test transmitter was set to 35.15 GHz, which corresponds to the operating frequency of the radar magnetron. To receive maximum SNR the local oscillators of the radar were adjusted so that the center of the receiving bandwidth of the radar matches 35.15 GHz. The frequency was tuned in steps of 1 MHz and the maximum of SNR was found at a 1-MHz offset. Such an offset is within the uncertainty of the frequency synthesizers, which are mainly optimized for spectral purity and not for accurate frequency matching.

The scanning regime can be described as follows. The radar was scanning over the azimuth in the range from  $-4^\circ$  to  $4^\circ$  with respect to the maximum position with an angular speed  $0.5^\circ \text{ s}^{-1}$ . The elevation angle was changed by  $0.1^\circ$  after every azimuth cycle. To avoid effects of the ground on signal propagation, the pattern measurements were performed in two steps. First, the lower half of the antenna pattern was measured. Then the antenna was rotated in both azimuth and elevation by  $180^\circ$  to measure the second half of the pattern in the same relative position to the ground. The overlap in elevation between these two measurements was  $2^\circ$ . The same procedure was done for  $\beta = 45^\circ$  and  $\beta = 90^\circ$ . The  $\beta = 45^\circ$  and  $\beta = 90^\circ$  orientations were set with respect to the position with  $\beta = 0^\circ$  by using a spirit level.

The processing of the raw data with quadrature components of the received signal includes the calculation of the following parameters:

$$F_{cc}(\theta, \phi) = \frac{\langle |\dot{f}_{cc}(\theta, \phi)| \rangle}{\langle |\dot{f}_{cc}(0, 0)| \rangle}, \quad (3.12)$$

$$F_{cx}(\theta, \phi) = \frac{\langle |\dot{f}_{cx}(\theta, \phi)| \rangle}{\langle |\dot{f}_{cc}(0, 0)| \rangle}, \quad (3.13)$$

$$F_{xc}(\theta, \phi) = \frac{\langle |\dot{f}_{xc}(\theta, \phi)| \rangle}{\langle |\dot{f}_{cc}(0, 0)| \rangle}, \quad (3.14)$$

$$F_{xx}(\theta, \phi) = \frac{\langle |\dot{f}_{xx}(\theta, \phi)| \rangle}{\langle |\dot{f}_{cc}(0, 0)| \rangle}, \quad (3.15)$$

$$\alpha_1(\theta, \phi) = \langle \arg(\dot{f}_{cc}(\theta, \phi)) - \arg(\dot{f}_{cx}(\theta, \phi)) \rangle, \quad (3.16)$$

$$\alpha_2(\theta, \phi) = \langle \arg(\dot{f}_{xc}(\theta, \phi)) - \arg(\dot{f}_{xx}(\theta, \phi)) \rangle, \quad (3.17)$$

$$\alpha_3(\theta, \phi) = \langle \arg(\dot{f}_{cc}(\theta, \phi)) - \arg(\dot{f}_{xx}(\theta, \phi)) \rangle. \quad (3.18)$$

In Eqs. (3.12) – (3.18)  $F_{mn}$  are the normalized amplitude patterns and  $\alpha_{1,2,3}$  are the phase differences between the respective complex antenna patterns. The averaging interval was 0.2 s. The resulting apparent azimuth resolution of the antenna patterns is  $0.1^\circ$ . The

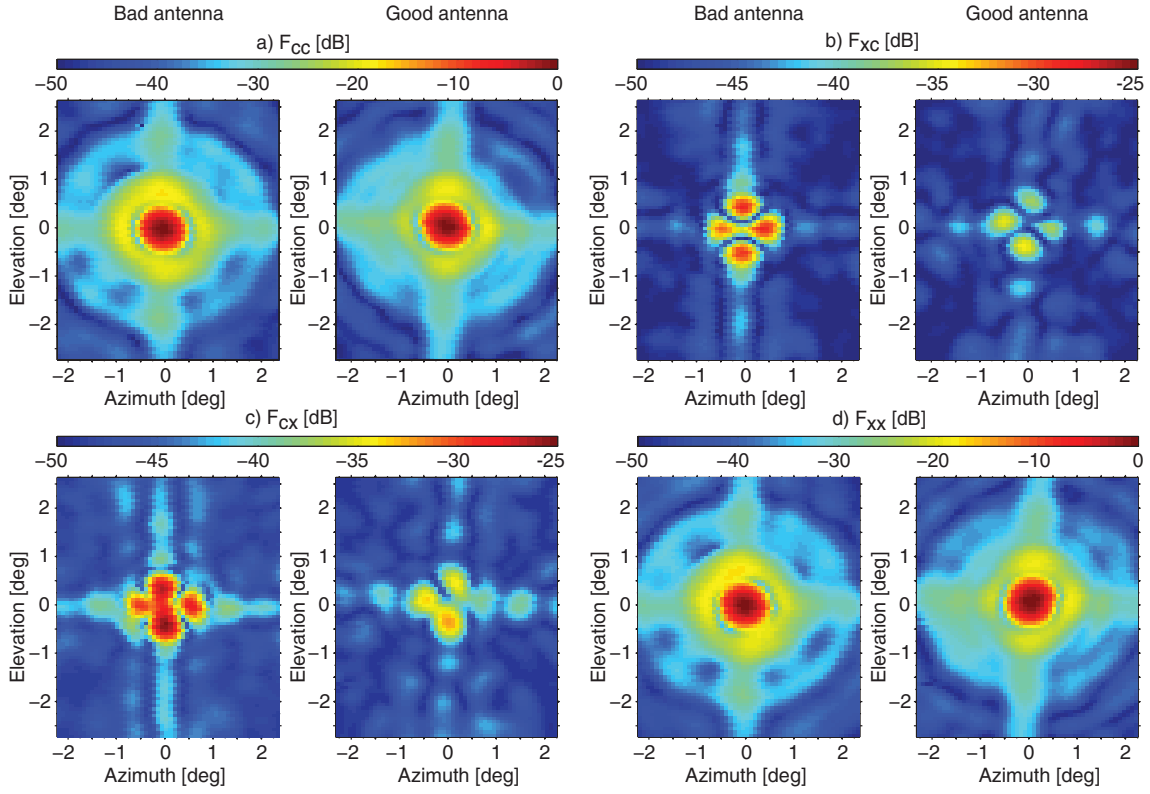


**Figure 3.5:** Normalized amplitude antenna patterns for the bad (first and third columns) and good (second and fourth columns) antenna. Note that scales for (a) and (d) differ from (b) and (c).

normalized antenna patterns can be written in the matrix form:

$$\mathbf{F}'(\theta, \phi) = \begin{pmatrix} F_{cc}(\theta, \phi) & F_{xc}(\theta, \phi)e^{i(\alpha_2(\theta, \phi) - \alpha_3(\theta, \phi))} \\ F_{cx}(\theta, \phi)e^{-i\alpha_1(\theta, \phi)} & F_{xx}(\theta, \phi)e^{-i\alpha_3(\theta, \phi)} \end{pmatrix}. \quad (3.19)$$

### 3.1.3 Results of antenna pattern measurements

The results of the receiving-pattern measurements for both antennas are shown in Figs. 3.5 – 3.7. The measured patterns are typical for a center-fed parabolic reflector [Zrnić *et al.*, 2010]. In Fig. 3.5 it can be seen that the patterns of  $F_{cc}(\theta, \phi)$  and  $F_{xx}(\theta, \phi)$  are almost identical for both antennas. The main beams are symmetrical in the azimuth and elevation plane and their width at the half-power level is about 0.7 degrees (Fig. 3.7), which is in good agreement with the technical documentation of the antennas. Visible are also two adjacent sidelobes with amplitudes of  $-18$  and  $-27$  dB, respectively. The second and following sidelobes have negligibly low amplitudes and do not have a significant influence on the resulting signal.

Table 3.3 shows the ICPR components  $H_{1,2,3}$  integrated over different areas of the antenna patterns. The areas are illustrated in Fig. 3.8. The results indicate that the fraction of ICPR induced in the area outside of the main beam does not exceed 10 % for both antennas. The



combined analysis of the co-polarized and cross-polarized antenna patterns shows that the polarization leakage in the center of the main beam is very low. The ratio of the cross-polarized signal to the co-polarized signal yields values of about  $-45$  and  $-35$  dB for the good and bad antenna, respectively. It should be noted that the real values of the coupling in the beam centers can be even lower. The measured values depend not only on the quality of the horn antenna of the test transmitter, but also on the accuracy of the positioning of this transmitter. Nevertheless, lower coupling values in the beam center will not change the results significantly. Such low coupling values explain the small contribution of the beam center to ICPR (zone I in Table 3.3). The largest contribution to ICPR for both antennas comes from zones II and III (Table 3.3). These zones correspond to the periphery of the main beam. Within zones II and III there are four areas with an increased leakage (the mean ratios of the cross-polarized signal to the co-polarized signal are  $-13$  dB and  $-8$  dB for the good and bad antenna, respectively). These areas are formed by the struts [Chandrasekar and Keeler, 1993] holding the antenna sub-reflector (Fig. 3.4), which causes an increase in ICPR.

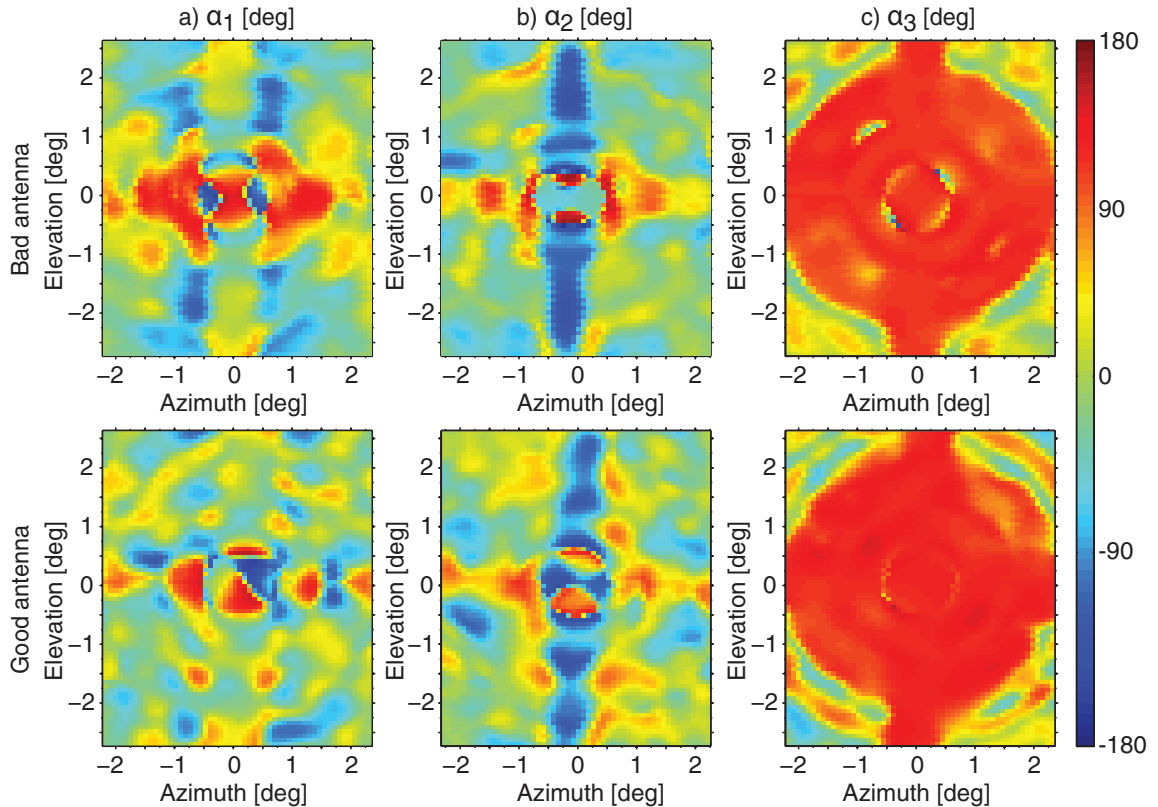


**Figure 3.6:** Patterns of the phase differences for the bad (upper row) and good (lower row) antenna, respectively.

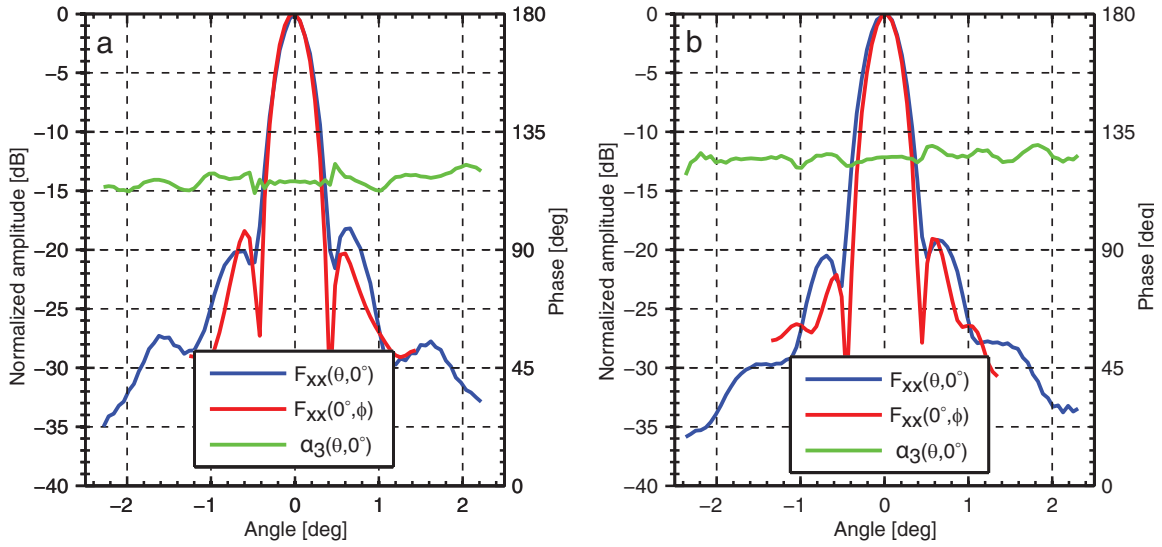


**Figure 3.7:** Cut planes of  $F_{xx}$  over the azimuth, of  $F_{xx}$  over the elevation, and of  $\alpha_3$  over the azimuth for the bad (a) and good (b) antenna.

Table 3.3 also demonstrates the dominance of the components  $H_1$  and  $H_2$  in ICPR for the bad antenna. The total contribution of  $H_3$  for the bad antenna is negligibly small, because negative values in the center of the main beam and positive values at the periphery of the

**Table 3.3:** Components  $H_{1,2,3}$  of ICPR calculated from the measured complex antenna patterns. Values in columns I-V correspond to different integration areas (Fig. 3.8). All values are given in linear units.

Integrated parameter	I	II	III	IV	V	Total
<i>Bad antenna</i>						
$H_1 \times 10^4$	2.01	4.30	3.62	0.66	0.39	10.98
$H_2 \times 10^4$	5.28	10.03	4.85	0.77	0.29	21.22
$H_3 \times 10^4$	-4.45	-2.62	5.71	0.86	0.46	-0.04
$\sum_{i=1}^3 H_i \times 10^4$	2.84	11.71	14.18	2.30	1.14	32.17
<i>Good antenna</i>						
$H_1 \times 10^4$	0.10	0.44	0.48	0.09	0.04	1.16
$H_2 \times 10^4$	0.45	1.70	1.18	0.19	0.08	3.60
$H_3 \times 10^4$	-0.13	0.73	0.93	0.10	0.04	1.66
$\sum_{i=1}^3 H_i \times 10^4$	0.42	2.87	2.58	0.38	0.16	6.42

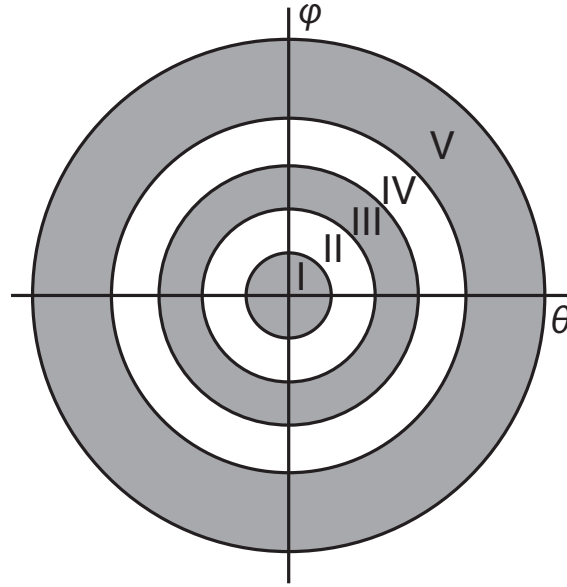


**Figure 3.8:** Integration areas. The areas I–V have outer radii of  $0.2^\circ$ ,  $0.4^\circ$ ,  $0.6^\circ$ ,  $0.8^\circ$ , and  $2.5^\circ$ , respectively, with respect to the position  $\theta = 0^\circ$  and  $\phi = 0^\circ$ .

main beam partially cancel out. Even though in the case of the good antenna  $H_2$  gives the largest contribution to ICPR, all the components have the same order of magnitude. Note, the  $H_3$  contribution exceeds the  $H_1$  contribution and cannot be neglected as in the case of the bad antenna.

From Fig. 3.7 it can be concluded that the phase difference  $\alpha_3(\theta, \phi)$  is constant in the main beam. The standard deviation of  $\alpha_3(\theta, \phi)$  within the two sidelobes is  $8^\circ$  and  $18^\circ$  for the good and bad antennas, respectively. The value of  $\alpha_3(\theta, \phi)$  is thus mostly defined by the different path lengths of the co- and cross-channel.

The evaluation of  $\alpha_{1,2}(\theta, \phi)$ , based on Fig. 3.6, shows that the phase difference between the cross-polarized and co-polarized signals is not constant over the whole antenna pattern especially in zones II and III which produce up to 80 % of the polarization leakage.

Using the measured antenna patterns, ICPR can be calculated from Eqs. (3.5) and (3.19). These calculations yield ICPR values of  $-24.9$  and  $-31.9$  dB for the bad and good antenna, respectively. As it was shown in Sec. 3.1.1, the corresponding ICPR values measured with a vertically-aligned beam in light-rain conditions were about  $-25$  and  $-31$  dB, respectively. Thus it is concluded that there is a relatively good agreement between the calculated and measured ICPR values.

In order to assess the impact of the phase differences on the estimate of ICPR this estimate was compared with the upper bound of ICPR calculated only from amplitude

**Table 3.4:** Components  $R_{1,2}$  of  $\rho_b$  calculated from the measured complex antenna patterns. Integration areas are the same as in Table 3.3.

	I	II	III	IV	V	Total
<i>Bad antenna</i>						
$R_1 \times 10^2$	4.26	10.04	4.20	0.23	-0.15	18.58
$R_2 \times 10^2$	-16.77	-18.06	-1.43	0.36	0.11	-35.81
<i>Good antenna</i>						
$R_1 \times 10^2$	1.80	3.89	3.50	0.22	-0.12	9.28
$R_2 \times 10^2$	6.91	-1.46	-6.65	0.03	0.07	-1.09

antenna patterns [Chandrasekar and Keeler, 1993]:

$$\text{ICPR}_{ub} = \frac{\int [F_{cc}(\theta, \phi)F_{cx}(\theta, \phi) + F_{xc}(\theta, \phi)F_{xx}(\theta, \phi)]^2 d\Omega}{\int [F_{cc}(\theta, \phi)^2 - F_{xc}(\theta, \phi)^2]^2 d\Omega}. \quad (3.20)$$

Calculated values of  $\text{ICPR}_{ub}$  are  $-22.3$  dB and  $-30.8$  dB for the bad and good antenna, respectively. The  $\text{ICPR}_{ub}$  value of the bad antenna is about 2.5 dB higher than the ICPR value estimated in light rain and the ICPR calculated from the antenna patterns. The  $\text{ICPR}_{ub}$  value of the good antenna is 0.2 and 1.1 dB higher than the ICPR value estimated in light rain and the one calculated from the antenna patterns, respectively.

Analysis of Table 3.4 data shows that the components of the bias in the correlation coefficient are mainly formed in the main antenna beam (zones I-III). Values of  $\rho_b$  calculated from the antenna patterns are 0.4 and 0.1 for the good and bad antenna, respectively. Those measured in light rain are 0.37 and 0.17, respectively.

The values of ICPR and  $\rho_b$  allow for an estimation of the degree of polarization [Galletti et al., 2012]:

$$\mu = \left[ 1 - \frac{4\text{ICPR}}{(1 + \text{ICPR})^2} (1 - \rho_b^2) \right]^{1/2}. \quad (3.21)$$

The degree of polarization  $\mu$  in the case of isotropic scatterers should be strictly equal to 1, i.e. the received wave should be fully polarized [Galletti et al., 2012]. Nevertheless,  $\mu$  calculated for isotropic particles using the antenna patterns are 0.9946 and 0.9987 for the bad and good antenna, respectively. This indicates that the received wave has a non-polarized component that is produced by the antenna system and requires a correction in order to get accurate polarimetric variables.

In the next section an approach for the correction of polarimetric variables obtained in the LDR mode is presented. The approach is based on a decomposition of the coherency matrix into non-polarized and fully-polarized parts.

## 3.2 Correction of LDR measurements

Electromagnetic waves with  $0 < \mu < 1$  are denoted as partly polarized waves. The polarization state of a partly polarized wave can be characterized statistically by the  $2 \times 2$  coherency matrix [Kanareykin *et al.*, 1966, 1968; Born and Wolf, 1975]:

$$\mathbf{J} = \begin{pmatrix} J_{cc} & \dot{J}_{cx} \\ \dot{J}_{xc} & J_{xx} \end{pmatrix}. \quad (3.22)$$

The elements of the coherency matrix  $\mathbf{J}$  can be calculated as follows [McCormick and Hendry, 1975]:

$$J_{cc} = \langle \dot{E}_c \dot{E}_c^* \rangle, \quad (3.23)$$

$$\dot{J}_{cx} = \langle \dot{E}_c \dot{E}_x^* \rangle, \quad (3.24)$$

$$\dot{J}_{xc} = \langle \dot{E}_x \dot{E}_c^* \rangle, \quad (3.25)$$

$$J_{xx} = \langle \dot{E}_x \dot{E}_x^* \rangle. \quad (3.26)$$

The complex amplitudes  $\dot{E}_c$  and  $\dot{E}_x$  for every received pulse are expressed using the  $I$  and  $Q$ -components measured by the radar:

$$\dot{E}_c = I_c + iQ_c, \quad (3.27)$$

$$\dot{E}_x = I_x + iQ_x. \quad (3.28)$$

The elements  $J_{cc}$  and  $J_{xx}$  are real quantities describing the received powers in the co- and cross-channel, respectively. The complex element  $\dot{J}_{cx}$  defines the covariance between the signals in the co- and cross-channels. It is necessary to note that  $\dot{J}_{cx} = \dot{J}_{xc}^*$ . In terms of the coherency matrix elements, LDR can be written in the following form:

$$\text{LDR} = \frac{J_{xx}}{J_{cc}}. \quad (3.29)$$

It should be emphasized that Eq. (3.29) is only valid when the coherency matrix is specified in the polarimetric basis formed by horizontal and vertical unit vectors (see Fig. 3.1).

The link between the coherency matrix elements for the case of scattering from distributed isotropic particles and corresponding antenna patterns can be found in Chandrasekar and Keeler [1993]. It is shown in Kanareykin *et al.* [1966] that the probability density function

of the phase shift between the orthogonal components  $W(\Delta\Phi)$  is defined by two parameters:  $\gamma = \arg(\dot{J}_{cx})$ , which specifies the mean value of  $\Delta\Phi$ , and the correlation coefficient

$$\rho_{cx} = |\dot{J}_{cx}| / \sqrt{J_{cc}J_{xx}}, \quad (3.30)$$

which defines the width of  $W(\Delta\Phi)$ , see Fig. 3.9.

The coherency matrix of a partly polarized wave can be represented as the sum of two components [Kanareykin *et al.*, 1966; Born and Wolf, 1975]:

$$\mathbf{J} = A_L \mathbf{I} + \begin{pmatrix} B_L & \dot{D}_L \\ \dot{D}_L^* & C_L \end{pmatrix}, \quad (3.31)$$

with the condition:

$$B_L C_L - |\dot{D}_L|^2 = 0, \quad (3.32)$$

where  $\mathbf{I}$  is a  $2 \times 2$  unit matrix.  $A_L$ ,  $B_L$ ,  $C_L$ , and  $\dot{D}_L$  can be calculated with the following equations [Kanareykin *et al.*, 1966; Born and Wolf, 1975]:

$$A_L = \frac{1}{2} \left[ \text{Sp} \mathbf{J} - (\text{Sp}^2 \mathbf{J} - 4 \det \mathbf{J})^{1/2} \right], \quad (3.33)$$

$$B_L = \frac{1}{2} \left[ J_{cc} - J_{xx} + (\text{Sp}^2 \mathbf{J} - 4 \det \mathbf{J})^{1/2} \right], \quad (3.34)$$

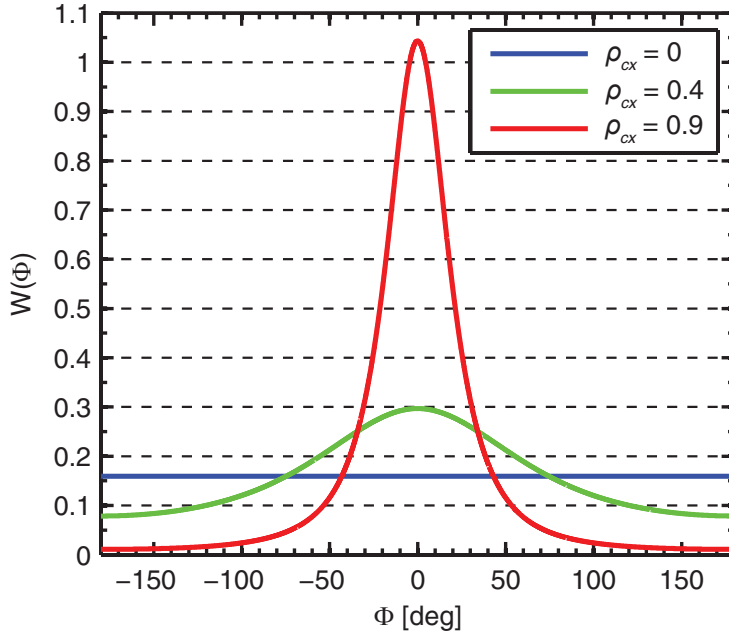


**Figure 3.9:** Centralized probability density function  $W(\Phi)$ , where  $\Phi = \Delta\Phi - \gamma$ . Adopted from Kanareykin *et al.* [1966].

$$C_L = \frac{1}{2} \left[ J_{xx} - J_{cc} + (\text{Sp}^2 \mathbf{J} - 4 \det \mathbf{J})^{1/2} \right], \quad (3.35)$$

$$\dot{D}_L = \dot{J}_{cx}. \quad (3.36)$$

Here  $\text{Sp}$  is the matrix trace and  $\det$  is the matrix determinant.

In Eq. (3.31) the first and second components describe the non-polarized and fully-polarized parts of the electromagnetic wave, respectively, i.e., the received electromagnetic wave can be presented as a sum of non-polarized and fully-polarized waves. The non-polarized part does not have a major polarization state and the phase shift between its orthogonal components is uniformly distributed, so that the cross-correlation coefficient of the non-polarized wave is 0. The fully-polarized part is characterized by a constant polarization state. The correlation coefficient of the fully-polarized wave is 1.

In the case of vertical sensing of hydrometeors consisting of drizzle or light rain the scattering volume can be assumed to be isotropic. Under this condition the parameters  $A_i$ ,  $B_i$ , and  $C_i$  (the index  $i$  marks the case of isotropic scattering only) can be calculated from the  $I/Q$ -measurements using Eqs. (3.22)–(3.28) and (3.33)–(3.35). Further, the leakage from the cross-channel into the co-channel is neglected and the normalized parameters are introduced:

$$A'_i = \frac{A_i}{B_i}, \quad (3.37)$$

$$C'_i = \frac{C_i}{B_i}. \quad (3.38)$$

The parameter  $A'_i$  describes the power of the non-coherent leakage from the co-channel into the cross-channel that is formed by the antenna system. The parameter  $C'_i$  describes the power of the coherent leakage that is produced by the antenna system. As isotropic particles do not change the polarization state of the scattered wave, the polarimetric properties of the received wave are defined by the antenna system of the radar.  $A'_i$  and  $C'_i$  are stable in time under the assumption that the radar characteristics are constant. For Radar 1 equipped with the bad antenna, mean values of  $A'_i$  and  $C'_i$  found from vertical measurements in light rain using Eqs. (3.33)–(3.35) are  $-25.3$  and  $-32.9$  dB, respectively. Those for Radar 2 with the good antenna are  $-30.9$  and  $-47.6$  dB, respectively.

The LDR for isotropic scatterers can be presented in terms of the decomposed coherency matrix elements:

$$\text{LDR}_i = \text{ICPR} = \frac{A'_i + C'_i}{A'_i + 1}. \quad (3.39)$$

As shown previously, the ICPR of a given radar system can be either calculated using measurements of complex antenna patterns and Eqs. (3.5) and (3.19), or it can be measured in drizzle or light rain as shown in Sec. 3.1.1. Measurements in drizzle were used previously to

determine ICPR for cloud radars of NOAA and the U.S. Department of Energy as described in *Matrosov et al.* [2001] and *Matrosov et al.* [2012].

For anisotropic scatterers the fully-polarized and non-polarized parts of the backscatter signals depend not only on the radar hardware properties, but also on the scattering properties of the scatterers. As it was mentioned above, the correlation coefficient  $\rho_{cx}$ , which also influences the fully-polarized and non-polarized fraction of the received wave [*Galletti et al.*, 2012], depends on shape, orientation, and dielectric properties of the scatterers.

Hydrometeors are usually assumed to have a linear Eigen polarization basis [*Bringi and Chandrasekar*, 2001]. The polarimetric properties of backscatter signals produced by such scatterers can be decomposed into isotropic and anisotropic parts [*Tatarinov and Tatarinov*, 2011]. Taking this into account, the expressions for the elements  $A_L$  and  $C_L$  of the coherency matrix can be rewritten in the following form:

$$A_L = A_i + A_a, \quad (3.40)$$

$$C_L = C_i + C_a, \quad (3.41)$$

where  $A_a$  and  $C_a$  are the non-polarized and fully-polarized components of the received signals produced by anisotropic scattering in the cross-channel, respectively. As it was shown previously, the isotropic part of the signal in the cross-channel is defined by the radar hardware. Using Eqs. (3.30) – (3.32), (3.40), and (3.41), LDR and  $\rho_{cx}$  can be presented as follows:

$$\text{LDR} = \frac{A_i + A_a + C_i + C_a}{A_i + A_a + B_L}, \quad (3.42)$$

$$\rho_{cx} = \frac{\sqrt{B_L(C_i + C_a)}}{\sqrt{(A_i + A_a + B_L)(A_i + A_a + C_i + C_a)}}. \quad (3.43)$$

The corrected values of  $A_L$ ,  $B_L$ , and  $C_L$ , i.e., the values that would be observed in case of an ideal radar, can be written as:

$$A_{cor} = \begin{cases} A_L - \langle A'_i \rangle B_L, & \text{if } A_L/B_L > \langle A'_i \rangle + 3\sigma(A'_i) \\ 0, & \text{otherwise,} \end{cases} \quad (3.44)$$

$$B_{cor} = B_L(1 + \langle A'_i \rangle + \langle C'_i \rangle), \quad (3.45)$$

$$C_{cor} = \begin{cases} C_L - \langle C'_i \rangle B_L, & \text{if } C_L/B_L > \langle C'_i \rangle + 3\sigma(C'_i) \\ 0, & \text{otherwise.} \end{cases} \quad (3.46)$$

In Eqs. (3.44) and (3.46)  $\sigma$  is the standard deviation. The averages and standard deviations in Eqs. (3.44)–(3.46) are taken from the regions where rain or drizzle is observed. The conditions introduced in Eqs. (3.44) and (3.46) are necessary to reduce the errors caused by

---



noise. Then, the corrected values of LDR and  $\rho_{cx}$  can be obtained by using Eqs. (3.44) – (3.46):

$$\text{LDR}_{cor} = \frac{A_{cor} + C_{cor}}{A_{cor} + B_{cor}}, \quad (3.47)$$

$$\rho_{cor} = \frac{\sqrt{B_{cor}C_{cor}}}{\sqrt{(A_{cor} + B_{cor})(A_{cor} + C_{cor})}}. \quad (3.48)$$

For isotropic particles both  $A_{cor}$  and  $C_{cor}$  are equal to 0. Thus, Eq. (3.48) contains the indeterminate form 0/0 and the value of  $\rho_{cor}$  is undefined [Galletti *et al.*, 2012]. In this case the value of  $\rho_{cor}$  is replaced by the limit:

$$\lim_{J_{xx} \rightarrow 0} \frac{|\dot{J}_{cx}|}{\sqrt{J_{cc}J_{xx}}}. \quad (3.49)$$

In the case of reflection symmetry (e.g., randomly oriented particles)  $|\dot{J}_{cx}| = 0$  [Nghiem *et al.*, 1992; Ryzhkov, 2001]. Under this condition the limit in Eq. (3.49) becomes 0.

It is assumed that large cloud particles in a low-turbulence environment are mostly oriented with their major dimensions in the horizontal plane [Matrosov *et al.*, 2012]. In this case, for the LDR mode,  $A_L$  and  $C_L$  are several orders of magnitude smaller than  $B_L$ , so  $A'_i \ll 1$  and  $C'_i \ll 1$ , and Eqs. (3.47) and (3.48) can be simplified as follows:

$$\text{LDR}_{cor} \approx \text{LDR} - \text{ICPR}, \quad (3.50)$$

$$\rho_{cor} \approx \sqrt{\frac{C_L - C'_i B_L}{B_L(\text{LDR} - \text{ICPR})}}. \quad (3.51)$$

A result similar to Eq. (3.50) was previously obtained by Ryzhkov *et al.* [2002].

As an example, the results of the LDR correction based on Eq. (3.47) for the vertical profiles shown in Fig. 3.3 are depicted in Figs. 3.10 and 3.11. The minimum value of corrected LDR was limited to  $-40$  dB to make the figures more illustrative. It can be seen from Fig. 3.10 that the correction procedure lowered LDR values in the rain regions by more than 7 dB for both radars. The correction results are also noticeable in the ice region that was present above about 1.5 km height. Observed and corrected LDR values for the melting layer are approximately the same. Even though the difference between the corrected LDR of Radar 1 and Radar 2 can reach several decibels, the values are on average similar (Fig. 3.11). The data scatter in Fig. 3.11, which generally increases with decreasing LDR, provides a measure for uncertainty in the LDR correction. For very low LDR ( $< -35$  dB), measurement noise is already playing a major role. For such low values differences in corrected LDR are considered to be mostly due to noise and correction uncertainties.

The results of the correction of the correlation coefficient are shown in Fig. 3.12. The height-time cross-sections of the observed (i.e., not corrected) correlation coefficient  $\rho_{cx}$  for

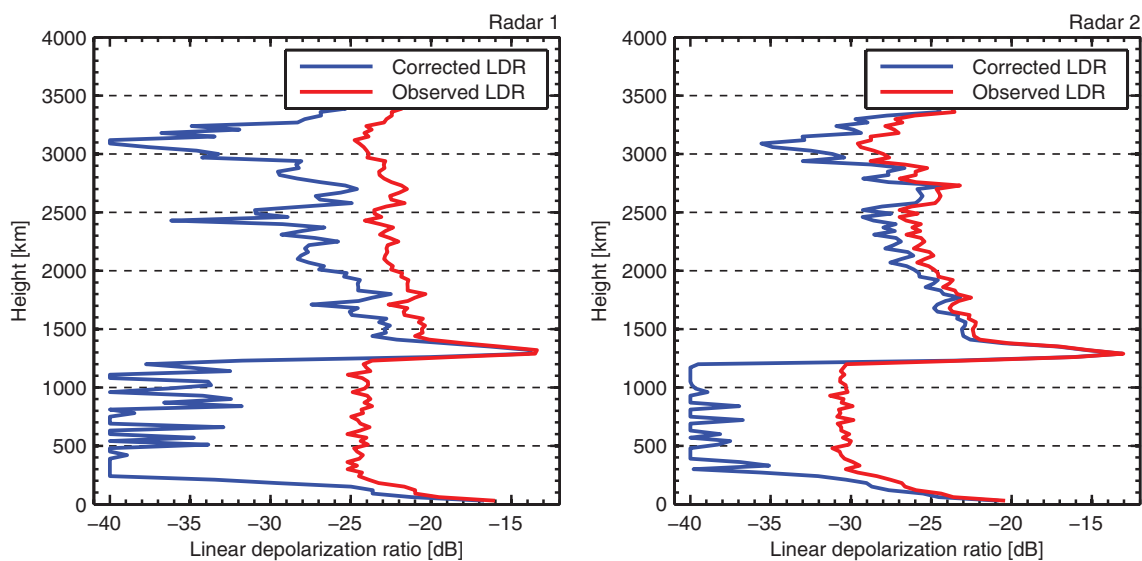


**Figure 3.10:** Vertical profiles of linear depolarization ratios for Radar 1 and Radar 2 for the same case as in Fig. 3.3.

Radar 1 and Radar 2, respectively, are presented in 3.12a and b. As it was mentioned in Sec. 3.1.1, the melting layer was located at 1.5 km height. Particles in this layer have strongly non-spherical shapes and their orientation is random in the polarization plane. Therefore, the observed values of the correlation coefficient for the melting layer are close to 0, because the non-polarized component of the received signals is mostly defined by the scattering

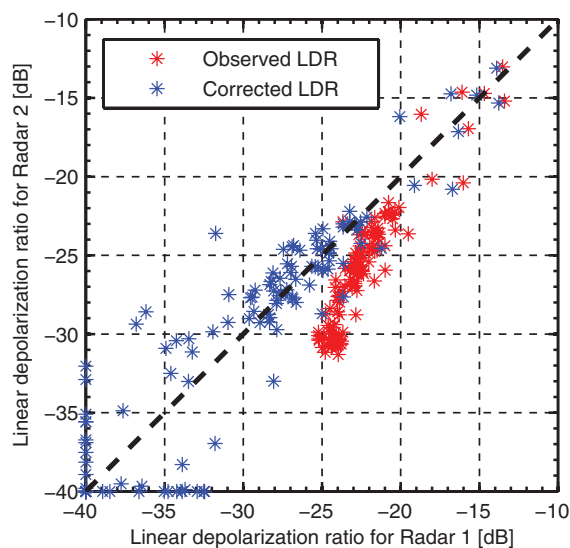


**Figure 3.11:** Scatter plot of observed (red dots) and corrected (blue dots) values of linear depolarization ratio for Radar 1 and Radar 2 for the same case as in Fig. 3.10.

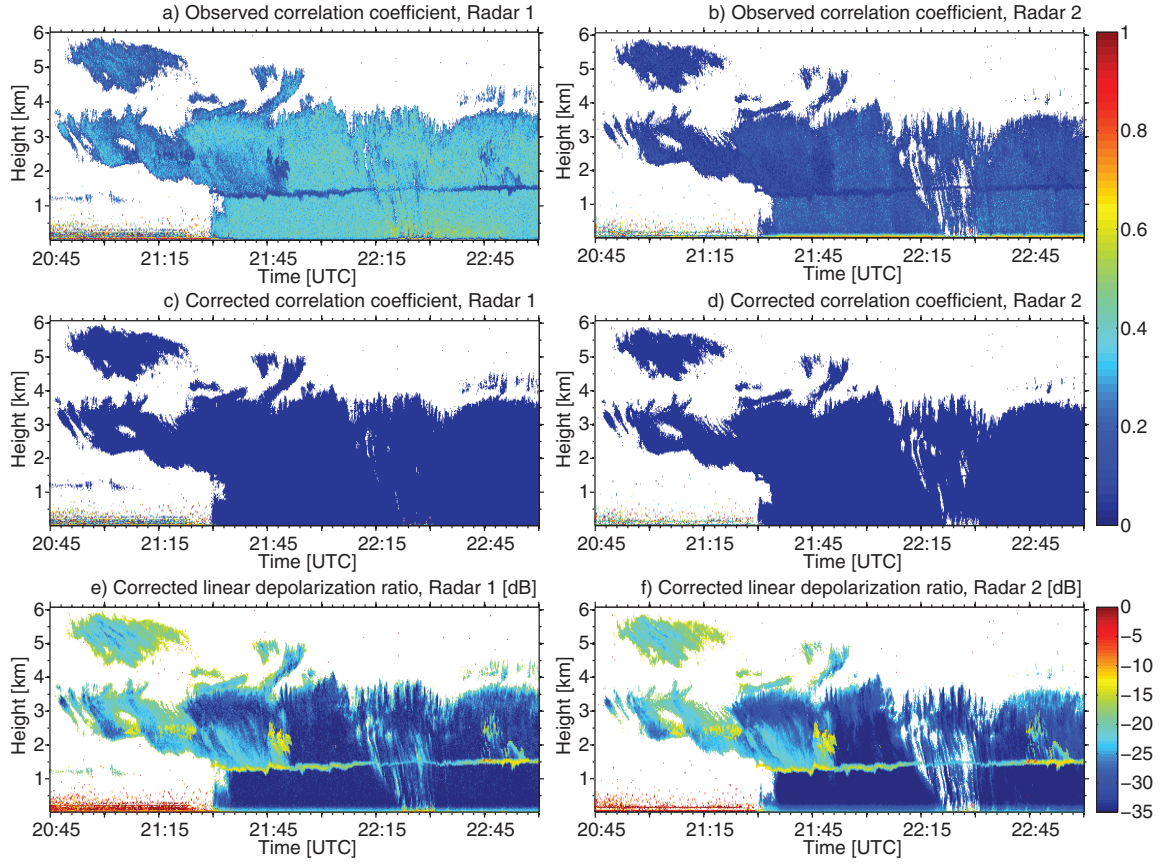


**Figure 3.12:** Observed correlation coefficient for Radar 1 (a), observed correlation coefficient for Radar 2 (b), corrected correlation coefficient for Radar 1 (c), corrected correlation coefficient for Radar 2 (d), corrected linear depolarization ratio for Radar 1 (e), and corrected linear depolarization ratio for Radar 2 (f) for the same case as in Fig. 3.2.

characteristics of the particles and not by the radar hardware properties. The values of the observed correlation coefficient  $\rho_{cx}$  in rain for Radar 1 are in the range of 0.3–0.4 while for Radar 2 those values are about 0.1–0.2. The values of observed  $\rho_{cx}$  for the rain are mostly defined by the radar hardware, and they are different for every radar. Above the melting layer some areas with decreased values of observed  $\rho_{cx}$  can be clearly seen in Fig. 3.12a. Ice particles in these areas are not isotropic scatterers. For instance, this can occur when some columnar shaped particles are present or non-spherical particles have a wide distribution in canting angle [Matrosov, 1991a]. Both cases lead to increased corrected values of LDR that can be apparently seen in Figs. 3.12e and f.

In Fig. 3.12c and 3.12d the height-time cross-sections of the corrected correlation coefficient  $\rho_{cor}$  are shown. It can be seen that for the whole cloud system  $\rho_{cor}$  is close to 0. This finding indicates that particles are either isotropic or non-spherical with random orientation

in the polarization plane [Ryzhkov, 2001; Ryzhkov et al., 2002] such as particles in the melting layer.

### 3.3 Discrimination between insects and clouds

A detailed analysis of the phase antenna patterns shown in Fig. 3.6 allowed for the development of a basis for a separation of insects and clouds. The approach is based on utilization of the cross-correlation coefficient. As it was shown in Sec. 3.2, clouds are volume distributed targets and characterized by low values of  $\rho_{cor}$  when a cloud radar is pointed vertically. In contrast, it is known that insects can be considered as point scatterers that produce strong depolarization [Martner and Moran, 2001]. In this case, the antenna system produces a narrow distribution of the phase difference between the co- and cross-channel signals (Fig. 3.6c) which leads to the high values of  $\rho_{cx}$ . Fig. 3.13 shows height-time cross sections of observed and corrected correlation coefficients and corrected LDR for the event from 12 September 2013. The melting layer, characterized by low values of both observed and corrected correlation coefficients and LDR of  $-15$  dB, was observed at about 1.7 km height. Above the melting layer, falling ice particles were observed, while below the melting layer light rain occurred. The echoes with high values of observed  $\rho_{cx}$  and LDR near the ground below 800 m correspond to insects. It can be seen that for insects observed and corrected correlation coefficients do not differ significantly. This fact indicates that the co- and cross-polarized components of the received signal are highly correlated either due to preferred orientation of insects, in agreement with other observations [Zrnica and Ryzhkov, 1998], or by low concentration of insects in the resolution volume, or both. The difference in the cross-correlation coefficient can be used for the separation of insects (point scatterers) and clouds (distributed scatterers). This can be especially useful for cases, when insects are present close to a melting layer, i.e. when LDR measurements cannot provide a reliable discrimination.

---

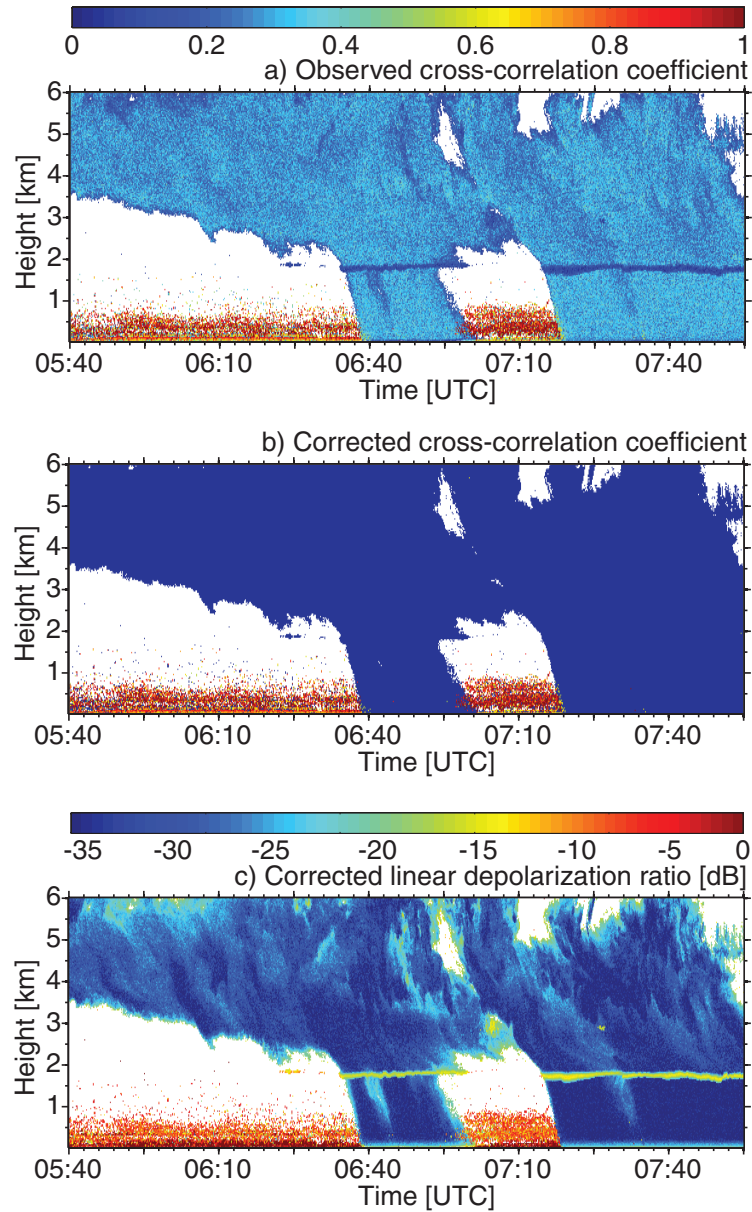


**Figure 3.13:** Observed (a) and corrected (b) correlation coefficient and corrected linear depolarization ratio (c) for the measurement taken with Radar 1 at Elmshorn, Germany, on 12 September 2013.



## Chapter 4

# Cloud radar MIRA-35 with hybrid mode

In the previous chapter, the approach of the correction of polarimetric variables for the polarization coupling was presented. The approach was applied to LDR and  $\rho_{cx}$  measured with the LDR-mode cloud radar. The developed approach is a prerequisite for the current chapter, which is devoted to a newly developed 35-GHz cloud radar MIRA-35 with hybrid polarimetric configuration and scanning capabilities. The material was published in *Myagkov et al.* [2016a]. The full procedure chain of the technical implementation and the realization of the setup of the hybrid-mode cloud radar are presented. The chapter is organized as follows. In Sec. 4.1 the implementation of the horizontal and vertical channel of the radar is presented and the phase adjustment procedure is described. An overview of the general data processing is given in Sec. 4.2. The correction of the data for the differences of amplifications and electrical path lengths in the horizontal and vertical channel is discussed in Sec. 4.3. The representation of the measured data in a 45°-rotated polarization basis, which permits the retrieval of the depolarization ratio, is presented in Sec. 4.4. Based on the findings from Chapter 3, in Sec. 4.5 it is explained how antenna effects on polarimetric measurements are corrected using the results obtained in the previous chapter. The spectral polarimetric variables are derived in Sec. 4.6. The approach applied to increase the signal-to-noise ratio in the hybrid mode is presented in Sec. 4.7.

### 4.1 Implementation and phase adjustment

Typically, cloud radars of type MIRA-35 emit linearly polarized waves in one of the channels. The corresponding operation mode is denoted as LDR mode. When the LDR correction described in Chapter 3 is applied, LDR measurements from different sites can be intercompared. Often, LDR measurements taken with vertically pointed cloud radars are used for

---

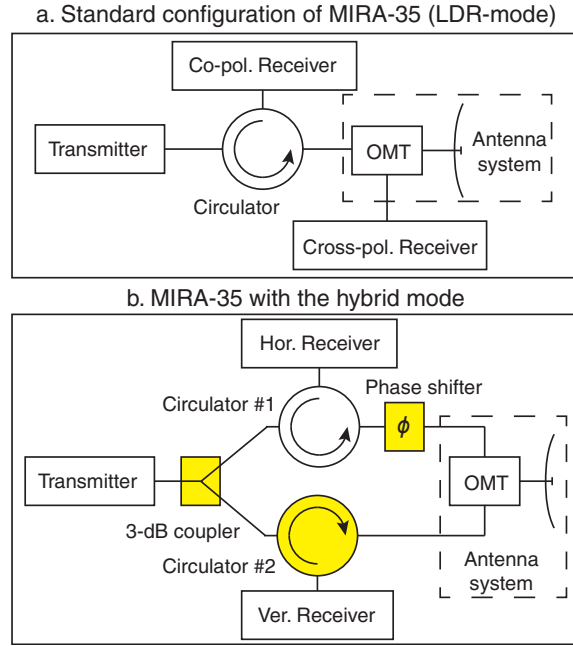


**Figure 4.1:** Simplified block diagrams of typical LDR (a) and hybrid (b) modes of MIRA-35. Components added for the implementation of the hybrid mode from the LDR mode are shown in yellow color.

clutter filtering [Görsdorf *et al.*, 2015] and a reliable detection of the melting layer [Lohmeier *et al.*, 1997]. At the same time, the applicability of the LDR mode for shape estimation is limited because of its high sensitivity to the orientation of cloud particles [Matrosov *et al.*, 2001].

For the shape studies presented in this thesis the hybrid mode is used. This mode is also known as Simultaneous Transmission and Simultaneous Reception (STSR) mode and is often used in weather radars [Ryzhkov *et al.*, 2005a]. In hybrid mode a radar transmits horizontal and vertical components of the signal simultaneously. Thus, expensive high-pulse-power polarization switching is not required. As will be shown in Chapter 5, the hybrid mode is capable of providing polarimetric parameters that allow for a quantitative estimate of particle shape and orientation characteristics of cloud hydrometeors.

The implementation of the hybrid mode was based on a standard scanning MIRA-35 cloud radar configured for the LDR mode. Simplified schemes of the traditional LDR mode and the implemented hybrid-mode configuration are shown in Fig. 4.1. In the hybrid mode, high-frequency power, generated by the magnetron-based transmitter, is split into two channels by a 3-dB coupler. A second circulator is added to decouple the high-power transmission line from the sensitive receiver in the vertical channel.

It is known that the exact polarization state of the transmitted radiation depends on the



phase shift between the orthogonal components of the transmitted signal  $\Delta\varphi_T$  (transmission phase difference). Often, polarimetric weather radars use an arbitrary elliptical polarization as the transmission phase difference  $\Delta\varphi_T$  is not adjusted to a certain value.

First, it was decided to evaluate the hybrid mode with the transmission phase difference  $\Delta\varphi_T$  adjusted to  $0^\circ$ , i.e., linear polarization of the transmitted radiation. In the future, a circular or elliptical polarization state of the transmitted signal can be easily implemented by shifting  $\Delta\varphi_T$ . Adjustable ferrite phase shifters for the peak power of 15 kW at Ka-band are expensive and, in addition, introduce extra power losses, which will result in worse sensitivity. Instead, in order to adjust the phase shift, the path length of the horizontal channel was slightly changed by inserting throttle plates (see Fig. 4.2) between the waveguide flanges. Changing of the transmission phase shift  $\Delta\varphi_T$  only requires to insert throttle plates right after the 3-dB coupler. In MIRA-35 the 3-dB coupler is installed inside the receiver unit and cannot be easily reached. Thus, due to the construction design of MIRA-35, throttle plates were inserted after the circulator #1 (see Fig. 4.1b). Introducing the additional phase shift after the circulator leads to changes of the phase shift also in the receiving path  $\Delta\varphi_R$  (reception phase difference). The reception phase difference  $\Delta\varphi_R$  can be removed during processing (Sec. 4.3).

To characterize phase shifts induced by the radar hardware, a polarization basis should be defined. In the description basis, the total phase difference between the horizontal and vertical channels  $\Delta\varphi_\Sigma$  measured in the configuration shown in Fig. 4.1b can be represented as follows:

$$\Delta\varphi_\Sigma = \underbrace{\Delta\varphi_{tp} + \Delta\varphi_{ps}}_{\Delta\varphi_T} + \Delta\varphi_{bs} + \underbrace{\Delta\varphi_{rp} + \Delta\varphi_{ps}}_{\Delta\varphi_R}, \quad (4.1)$$

where  $\Delta\varphi_{tp}$  is the phase shift caused by the difference in the electrical path lengths between the transmission channels,  $\Delta\varphi_{ps}$  is the phase shift introduced by the phase shifter,  $\Delta\varphi_{bs}$  is

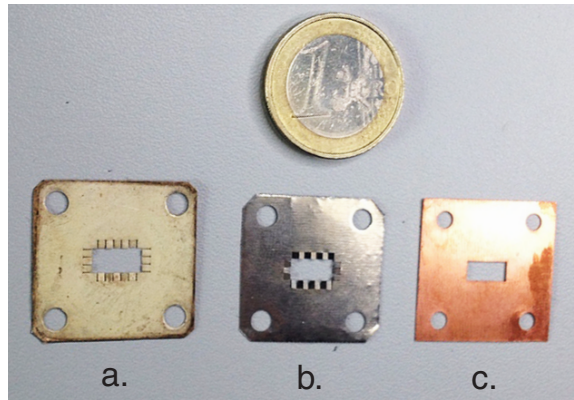


**Figure 4.2:** Throttle plates used for the phase adjustment. The thickness of the plates is 0.05 mm (a), 0.1 mm (b), and 0.28 mm (c). The introduced phase shift is  $1.8^\circ$  (a),  $3.4^\circ$  (b), and  $9.1^\circ$  (c).

the phase shift produced by atmospheric scatterers, and  $\Delta\varphi_{rp}$  is the phase shift caused by differences in the electrical path lengths of the reception channels.

The phase shift  $\Delta\varphi_{rp}$  was estimated based on previously documented antenna measurements (see Chapter 3). For the measurements the external test transmitter described in Chapter 3 was used. The test transmitter generates continuous linearly polarized radiation. The frequency of the test transmitter was set close to the operational frequency of the radar transmitter. The frequency of the radar local oscillator was adjusted to center the receiver bandwidth to the signal of the test transmitter. The rotatable antenna system of the test transmitter permits the change of the orientation  $\beta$  of the transmitted polarization with respect to the unit vector  $\mathbf{e}_h$  of the description basis. The radar was placed approximately 40 m away from the test transmitter and was operated in the receiving-only mode. The antennas of the radar and the test transmitter were pointed to each other. The measurement procedure was the same as described in Chapter 3. The phase difference  $\Delta\varphi_{rp}$  corresponds to  $\alpha_3(0, 0)$  (see Eq. (3.18)). The measurement showed  $\Delta\varphi_{rp}$  to be  $-2^\circ$ . Note that these measurements were performed before introducing throttle plates.

Knowing  $\Delta\varphi_{rp}$ , throttle plates were added into the horizontal channel in order to measure the introduced phase shift. Plates with thicknesses of 0.28 mm, 0.1 mm, and 0.05 mm (see Fig. 4.2) introduced phase shifts of  $9.1^\circ$ ,  $3.4^\circ$ , and  $1.8^\circ$ , respectively. It should be noted that the wavelength in the waveguide  $\lambda_g$  is 10.8 mm, which is longer than the one in vacuum [Marcuvitz, 1965, Ch. 2.2]. Calculated values of  $\Delta\varphi_{ps}$  for  $\lambda_g$  are  $9.3^\circ$ ,  $3.3^\circ$ , and  $1.7^\circ$ , respectively.

It is known that randomly oriented particles do not produce a backscattering differential phase shift [Trömel *et al.*, 2013]. Therefore, for vertical observations of clouds without electrical activity  $\Delta\varphi_{bs} = 0$  can be assumed. In this case,  $\Delta\varphi_{tp}$  can be estimated from the measured total phase difference  $\Delta\varphi_\Sigma$  observed by the vertically pointed radar using Eq. (4.1). Measurements performed without installed throttle plates resulted in  $\Delta\varphi_\Sigma = -21.6^\circ$  and, thus,  $\Delta\varphi_{tp} = -19.6^\circ$ . In order to adjust the transmission phase difference  $\Delta\varphi_T$  as close to  $0^\circ$  as possible several throttle plates with a total thickness of  $\sim 0.6$  mm were inserted into the horizontal channel. This introduced  $20.5^\circ$  of additional phase shift  $\Delta\varphi_{ps}$  and resulted in the transmission phase difference  $\Delta\varphi_T = -0.9^\circ$  and the reception phase difference  $\Delta\varphi_R = 18.5^\circ$ .

During the operation the frequency of the magnetron can vary with temperature within  $\pm 1$  MHz. Such variations of the operational frequency cause changes of  $\Delta\varphi_\Sigma$ . Measured changes of  $\Delta\varphi_\Sigma$  due to the frequency variation of the magnetron do not exceed  $\pm 1^\circ$ , which can be considered as not significant. Nevertheless, during long-term operation variations in ambient conditions led to changes of  $\pm 8^\circ$  in  $\Delta\varphi_{rp}$ . Significant changes in  $\Delta\varphi_{rp}$  usually took several days. To account for these changes, periodical vertical observations in light rain ( $\Delta\varphi_{bs} = 0^\circ$ ) are required. Then, assuming  $\Delta\varphi_{tp}$  and  $\Delta\varphi_{ps}$  to be constant,  $\Delta\varphi_{rp}$  can be found using Eq. (4.1).

## 4.2 Processing of the coherency matrix

MIRA-35 is a coherent cloud radar. Two receivers calculate in-phase ( $I$ ) and quadrature ( $Q$ ) parts for vertical and horizontal components of the returned signal. Below, the horizontal and vertical components are denoted by indexes  $h$  and  $v$ , respectively.  $I_h$ ,  $I_v$ ,  $Q_h$ , and  $Q_v$  components are obtained for every pulse cycle and range gate. FFT over  $I_h + iQ_h$  and  $I_v + iQ_v$ , calculated from  $N_F$  pulses, is used to estimate discrete complex spectra  $\dot{S}_h(\omega_k)$  and  $\dot{S}_v(\omega_k)$ , respectively. Here  $\omega_k$  denotes a Doppler frequency of a spectral component  $k = 0, \dots, N_F - 1$ :

$$\omega_k = \frac{k f_r \pi}{N_F}, \quad (4.2)$$

where  $f_r$  is the pulse repetition frequency. Details of the  $I/Q$  and spectrum computation in MIRA-35 data processing are given by *Görsdorf et al.* [2015].

Using  $N_s$  complex spectra  $\dot{S}_h(\omega_k)$  and  $\dot{S}_v(\omega_k)$ , the spectral form of the  $2 \times 2$  coherency matrix can be written as

$$\mathbf{B}(\omega_k) = \begin{pmatrix} B_{hh}(\omega_k) & \dot{B}_{hv}(\omega_k) \\ \dot{B}_{vh}(\omega_k) & B_{vv}(\omega_k) \end{pmatrix}. \quad (4.3)$$

The elements of the coherency matrix  $\mathbf{B}(\omega_k)$  are calculated as follows:

$$B_{hh}(\omega_k) = \langle \dot{S}_h(\omega_k) \dot{S}_h(\omega_k)^* \rangle, \quad (4.4)$$

$$\dot{B}_{hv}(\omega_k) = \langle \dot{S}_h(\omega_k) \dot{S}_v(\omega_k)^* \rangle, \quad (4.5)$$

$$\dot{B}_{vh}(\omega_k) = \langle \dot{S}_v(\omega_k) \dot{S}_h(\omega_k)^* \rangle, \quad (4.6)$$

$$B_{vv}(\omega_k) = \langle \dot{S}_v(\omega_k) \dot{S}_v(\omega_k)^* \rangle, \quad (4.7)$$

where  $\langle \rangle$  denotes averaging over  $N_s$  spectra. The real elements  $B_{hh}(\omega_k)$  and  $B_{vv}(\omega_k)$  are the power spectra in the horizontal and vertical channels, respectively. In MIRA-35 with LDR mode these spectra represent the co- and cross-polarized components of the received signal, respectively, and are used for the calculation of the radar reflectivity factor at horizontal polarization  $Z_h$ , mean Doppler velocity, Doppler width, and LDR [*Görsdorf et al.*, 2015].

A recent modification of the MIRA-35 software permits one to additionally calculate and store the complex element  $\dot{B}_{hv}(\omega_k)$ . It is necessary to note that  $\dot{B}_{hv}(\omega_k) = \dot{B}_{vh}^*(\omega_k)$ . Therefore, storage of the element  $\dot{B}_{vh}(\omega_k)$  is not required. Storing the elements  $B_{hh}(\omega_k)$ ,  $\dot{B}_{hv}(\omega_k)$ , and  $B_{vv}(\omega_k)$  in usual operational mode (Table 3.1) requires approximately 700 MB/hr, which is about 100 times less than storing the  $I/Q$  data.

### 4.3 Correction of the coherency matrix for differences of channels

The spectral form of the coherency matrix  $\mathbf{B}(\omega_k)$  allows for the calculation of spectral polarimetric variables. Advantages of such a representation have been shown for weather radar applications [Spek *et al.*, 2008]. Before the calculation of polarimetric parameters the elements of the coherency matrix  $\mathbf{B}(\omega_k)$  were corrected for the effect of differential amplification in the horizontal and vertical channels.

The spectral components  $\omega_n$  ( $n \in k$ ) are defined where both  $B_{hh}(\omega_k)$  and  $B_{vv}(\omega_k)$  are at least 30 dB higher than the mean noise levels  $N_h$  and  $N_v$ , respectively. The mean noise levels can be determined by averaging the power spectra over the last range gates where no scatterers are present or by applying the Hildebrand-Sekhon algorithm [Hildebrand and Sekhon, 1974].

In order to correct for the difference in the amplifications a coefficient  $K_a$  is calculated:

$$K_a = \frac{B_{hh}(\omega_n) - N_h}{B_{vv}(\omega_n) - N_v}. \quad (4.8)$$

For the calculation of  $K_a$  rain observations with the vertically pointed radar are used. In this case, particles can be considered as spheres and do not change the polarization of the scattered wave. Data containing scattering from insects, which typically cause depolarization, should be avoided. For a rain event on 1 May 2014 a  $K_a$  value of  $1.46 \pm 0.02$  was calculated.

The effect of differences in the amplifications and the electrical path lengths on the components of Eq. (4.3) can be corrected as follows:

$$\dot{B}'_{hv}(\omega_k) = \sqrt{K_a} \dot{B}_{hv}(\omega_k) e^{-i\Delta\varphi_R}, \quad (4.9)$$

$$B'_{vv}(\omega_k) = K_a B_{vv}(\omega_k). \quad (4.10)$$

The additional phase shift, introduced in  $\dot{B}'_{hv}(\omega_k)$ , removes the reception phase difference  $\Delta\varphi_R$ . The spectra  $B_{hh}(\omega_k)$ ,  $B_{vv}(\omega_k)$ , and  $B'_{vv}(\omega_k)$  are shown in Fig. 4.3. The coherency matrix with the corrected elements is denoted as  $\mathbf{B}'(\omega_k)$ .

As mentioned in Sec. 4.1, the calibration of the receiver is slowly fluctuating during operation. This causes variations of  $\pm 0.06$  in  $K_a$ . The range of  $K_a$  can be constrained by performing recalibrations during light rain.

### 4.4 Representation of the coherency matrix in the slanted basis

As it was shown in Chapter 3, the antenna coupling produces biases in polarimetric variables. Such biases hamper shape and orientation retrievals. The antenna coupling can be directly determined in LDR-mode cloud radars from vertical measurements in light rain or drizzle when particles can be assumed to be spherical. In this case, the cross-polarized returned signal is caused only by the coupling [Chandrasekar and Keeler, 1993]. In cloud radars

with the hybrid mode the estimation of antenna effects is not straightforward as the major part of the returned signal in both channels is produced by scatterers. In this section the representation of the coherency matrix  $\mathbf{B}'(\omega_k)$  in the polarization basis rotated by  $45^\circ$  with respect to the description basis is shown. The Jones vector of a received signal in the description and slanted basis is shown in Fig. 4.4. Such a representation provides the co-polarized and cross-polarized components that would be measured by a cloud radar with slanted polarimetric basis. These components can be used for the correction algorithm proposed in Chapter 3. In addition, the change of the polarization basis makes it possible to calculate SLDR and the cross-correlation coefficient in the slanted basis, which cannot be directly measured in the hybrid mode.

The corrected coherency matrix  $\mathbf{B}'(\omega_k)$  can be represented in the linear basis rotated by  $45^\circ$  with respect to the description basis:

$$\mathbf{B}_S(\omega_k) = \mathbf{F}_R^T \mathbf{B}'(\omega_k) \mathbf{F}_R, \quad (4.11)$$

where  $T$  is the transpose sign and  $\mathbf{F}_R$  is the rotational operator:

$$\mathbf{F}_R = \frac{1}{\sqrt{2}} \begin{pmatrix} 1 & 1 \\ -1 & 1 \end{pmatrix}. \quad (4.12)$$

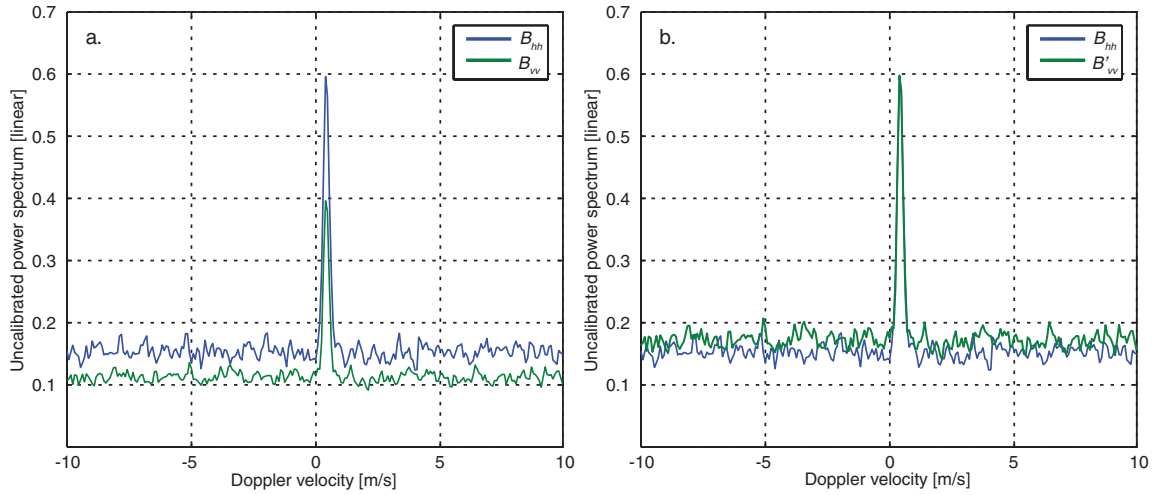


**Figure 4.3:** (a) Uncalibrated power spectra in the horizontal (blue line) and vertical (green line) channels. Displayed observations were obtained with the vertically pointed radar in light rain. (b) Uncalibrated power spectrum in the horizontal channel (blue line) and corrected power spectrum in the vertical channel (green line). The same data as in (a) are used. Mean noise levels of  $B_{hh}$  and  $B'_{vv}$ , estimated using the Hildebrand-Sekhon algorithm, are 0.153 and 0.169, respectively. Note, that this case was chosen to illustrate the correction. Due to low signal-to-noise ratios, such spectra were not used for the calculation of the coefficient  $K_a$  (see Sec. 4.6).

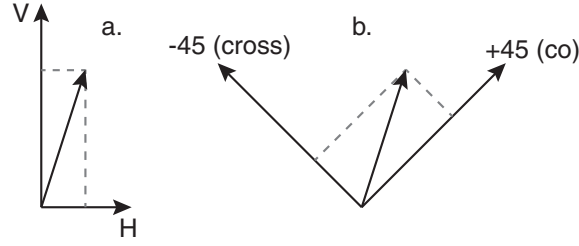


**Figure 4.4:** The Jones vector of a received signal represented in the description (a) and slanted (b) polarization basis.

The elements of  $\mathbf{B}_S(\omega_k)$  can be calculated as follows:

$$B_{xx}(\omega_k) = \frac{1}{2} \left\{ B_{hh}(\omega_k) + B'_{vv}(\omega_k) - 2\text{Re} \left[ \dot{B}'_{hv}(\omega_k) \right] \right\}, \quad (4.13)$$

$$\dot{B}_{xc}(\omega_k) = \frac{1}{2} \left\{ B_{hh}(\omega_k) - B'_{vv}(\omega_k) + 2i\text{Im} \left[ \dot{B}'_{hv}(\omega_k) \right] \right\}, \quad (4.14)$$

$$B_{cc}(\omega_k) = \frac{1}{2} \left\{ B_{hh}(\omega_k) + B'_{vv}(\omega_k) + 2\text{Re} \left[ \dot{B}'_{hv}(\omega_k) \right] \right\}. \quad (4.15)$$

In the slanted basis the indexes  $c$  and  $x$  are used to denote the co-polarized and cross-polarized components, respectively. Note that these components would be directly measured by a cloud radar with the slanted polarimetric basis.

The coherency matrix  $\mathbf{B}_S(\omega_k)$  can be considered as the coherency matrix measured in the slanted linear depolarization mode (SLDR mode), which was used for the shape classification by *Matrosov et al.* [2012]. In SLDR mode and hybrid mode with transmission phase difference  $\Delta\varphi_T = 0^\circ$  the transmitted signals have the same polarization state. The difference between these polarimetric configurations is the  $45^\circ$  rotation of the receiving basis as performed in Eq. (4.11). Note that Eq. (4.11) allows for the representation of the coherency matrix measured in the SLDR mode in the horizontal-vertical basis and, thus, can be used to retrieve polarimetric variables such as  $Z_{DR}$  and  $\rho_{hv}$ .

For the subsequent data analysis spectral components  $\omega_p$ , where the backscattered signal is detected in the elements  $B_{cc}(\omega_k)$  and  $B_{xx}(\omega_k)$ , are defined. The threshold applied for the detection is calculated as follows:

$$B_{Tc,Tx} = N_{c,x} \left( 1 + \frac{Q}{\sqrt{N_s}} \right). \quad (4.16)$$

In Eq. (4.16)  $N_{c,x}$  is the mean power of noise of  $B_{cc}(\omega_k)$  and  $B_{xx}(\omega_k)$ , respectively. The value of  $Q = 5$ , which is applied for the thresholding in the operational MIRA-35 radars [Görsdorf et al., 2015], is used.

Further, the mean noise levels are removed from the elements  $B_{cc}(\omega_p)$  and  $B_{xx}(\omega_p)$ :

$$B'_{cc}(\omega_p) = B_{cc}(\omega_p) - N_c, \quad (4.17)$$

$$B'_{xx}(\omega_p) = B_{xx}(\omega_p) - N_x. \quad (4.18)$$

The correlation between noise in the orthogonal components is negligible and, thus, does not influence the element  $\dot{B}_{xc}(\omega_p)$  significantly. The resulting coherency matrix is represented as follows:

$$\mathbf{B}'_S(\omega_p) = \begin{pmatrix} B'_{xx}(\omega_p) & \dot{B}_{xc}(\omega_p) \\ \dot{B}_{xc}^*(\omega_p) & B'_{cc}(\omega_p) \end{pmatrix}. \quad (4.19)$$

## 4.5 Correction of the coherency matrix for the antenna coupling

In analogy to Eqs. (3.31)–(3.36) the coherency matrix  $\mathbf{B}'_S(\omega_p)$  is decomposed into non-polarized and fully-polarized parts:

$$\mathbf{B}'_S(\omega_p) = A_S(\omega_p)\mathbf{I} + \begin{pmatrix} B_S(\omega_p) & \dot{D}_S(\omega_p) \\ \dot{D}_S^*(\omega_p) & C_S(\omega_p) \end{pmatrix}, \quad (4.20)$$

with the condition:

$$B_S(\omega_p)C_S(\omega_p) - |\dot{D}_S(\omega_p)|^2 = 0. \quad (4.21)$$

$A_S(\omega_p)$ ,  $B_S(\omega_p)$ ,  $C_S(\omega_p)$ , and  $\dot{D}_S(\omega_p)$  can be calculated with the following equations [Kanareykin *et al.*, 1966; Born and Wolf, 1975]:

$$A_S(\omega_p) = \frac{1}{2} \left( \text{Sp} [\mathbf{B}'_S(\omega_p)] - \{ \text{Sp}^2 [\mathbf{B}'_S(\omega_p)] - 4 \det [\mathbf{B}'_S(\omega_p)] \}^{1/2} \right), \quad (4.22)$$

$$B_S(\omega_p) = \frac{1}{2} \left( B'_{xx}(\omega_p) - B'_{cc}(\omega_p) + \{ \text{Sp}^2 [\mathbf{B}'_S(\omega_p)] - 4 \det [\mathbf{B}'_S(\omega_p)] \}^{1/2} \right), \quad (4.23)$$

$$C_S(\omega_p) = \frac{1}{2} \left( B'_{cc}(\omega_p) - B'_{xx}(\omega_p) + \{ \text{Sp}^2 [\mathbf{B}'_S(\omega_p)] - 4 \det [\mathbf{B}'_S(\omega_p)] \}^{1/2} \right), \quad (4.24)$$

$$\dot{D}_S(\omega_p) = \dot{B}_{xc}(\omega_p). \quad (4.25)$$

Applying the method described in Chapter 3, the influence of antenna coupling on the elements  $A_S(\omega_p)$ ,  $B_S(\omega_p)$ , and  $C_S(\omega_p)$  is removed. Note that in this chapter the fully-polarized part of the co-polarized component is described by  $C_S(\omega_p)$ . The calculated variables are denoted as  $A'_S(\omega_p)$ ,  $B'_S(\omega_p)$ , and  $C'_S(\omega_p)$ , respectively. The corrected value  $\dot{D}'_S(\omega_p)$  can be found using  $B'_S(\omega_p)$  and  $C'_S(\omega_p)$  in Eq. (4.21). Reverse rotation of the slanted basis allows for the calculation of the elements  $A(\omega_p)$ ,  $B(\omega_p)$ , and  $C(\omega_p)$  in the description basis:

$$A(\omega_p) = A'_S(\omega_p), \quad (4.26)$$

$$B(\omega_p) = 0.5 \left( B'_S(\omega_p) + C'_S(\omega_p) + 2 \text{Re} \left\{ \sqrt{B'_S(\omega_p)C'_S(\omega_p)} e^{i \arg [\dot{D}'_S(\omega_p)]} \right\} \right), \quad (4.27)$$

$$C(\omega_p) = 0.5 \left( B'_S(\omega_p) + C'_S(\omega_p) - 2 \text{Re} \left\{ \sqrt{B'_S(\omega_p)C'_S(\omega_p)} e^{i \arg [\dot{D}'_S(\omega_p)]} \right\} \right). \quad (4.28)$$

## 4.6 Spectral polarimetric variables

From  $A(\omega_p)$ ,  $B(\omega_p)$ , and  $C(\omega_p)$  spectral polarimetric variables can be obtained. In the following, the word “spectral” is omitted for brevity. Differential reflectivity  $Z_{DR}(\omega_p)$ , correlation coefficient  $\rho_{hv}(\omega_p)$ , differential phase shift  $\Phi_{DP}(\omega_p)$ , SLDR( $\omega_p$ ), and cross-correlation coefficient  $\rho_s(\omega_p)$  in the slanted basis are defined as follows:

$$Z_{DR}(\omega_p) = \frac{A(\omega_p) + B(\omega_p)}{A(\omega_p) + C(\omega_p)}, \quad (4.29)$$

$$\rho_{hv}(\omega_p) = \left\{ \frac{B(\omega_p)C(\omega_p)}{[A(\omega_p) + B(\omega_p)][A(\omega_p) + C(\omega_p)]} \right\}^{1/2}, \quad (4.30)$$

$$\Phi_{DP}(\omega_p) = \arg \left[ \dot{B}'_{hv}(\omega_p) \right], \quad (4.31)$$

$$\text{SLDR}(\omega_p) = \frac{A'_S(\omega_p) + B'_S(\omega_p)}{A'_S(\omega_p) + C'_S(\omega_p)}, \quad (4.32)$$

$$\rho_s(\omega_p) = \left\{ \frac{B'_S(\omega_p)C'_S(\omega_p)}{[A'_S(\omega_p) + B'_S(\omega_p)][A'_S(\omega_p) + C'_S(\omega_p)]} \right\}^{1/2}. \quad (4.33)$$

In order to check the quality of the polarimetric measurements of MIRA-35 in hybrid mode, vertical-stare measurements of a cloud system, which passed over the METEK site on 1 May 2014, were performed. Figure 4.5 shows SNR (a) and the polarimetric variables (b–f) derived with Eqs. (4.29)–(4.33), respectively. The presented parameters were obtained for the spectral line at which the maximum signal was observed. From 17:45 to 18:00 UTC a melting layer is visible at 1.7 km height, indicated by enhanced values of SNR and SLDR. Below the melting layer light rain occurred, whereas ice crystals were present above. The comparison of Fig. 4.5 (b–f) with (a) shows that the polarimetric parameters could not be obtained for all data points because the quality criterion of Eq. (4.16) is not fulfilled when SNR is too low. At lower SNR, the influence of noise becomes significant resulting in high biases and variability in all polarimetric variables.

It can be seen in Fig. 4.5b and 4.5d that on average values of  $Z_{DR}$  and  $\Phi_{DP}$  in clouds and precipitation are close to 0 dB and  $0^\circ$ , respectively, which is the case when particles can be considered as spheres or randomly oriented in the polarization plane. Areas with slightly increased values of  $Z_{DR}$  and  $\Phi_{DP}$  are caused by noise, as these areas are in correlation with decreasing SNR especially along cloud edges. Insects are characterized by values of  $Z_{DR}$  and  $\Phi_{DP}$  that lie outside of the colorbars.

In rain, the correlation coefficient  $\rho_{hv}$  is 1, which is consistent with high values of this parameter observed by polarimetric weather radars [Mudukutore et al., 1995; Wang et al., 2006]. Slightly lower values of about 0.995 were observed in areas with ice particles producing weak depolarization. In the highly depolarizing melting layer  $\rho_{hv}$  is below 0.95.

Values of SLDR measured vertically in rain, in the melting layer, in ice areas, and in regions dominated by scattering from insects are consistent with direct measurements of



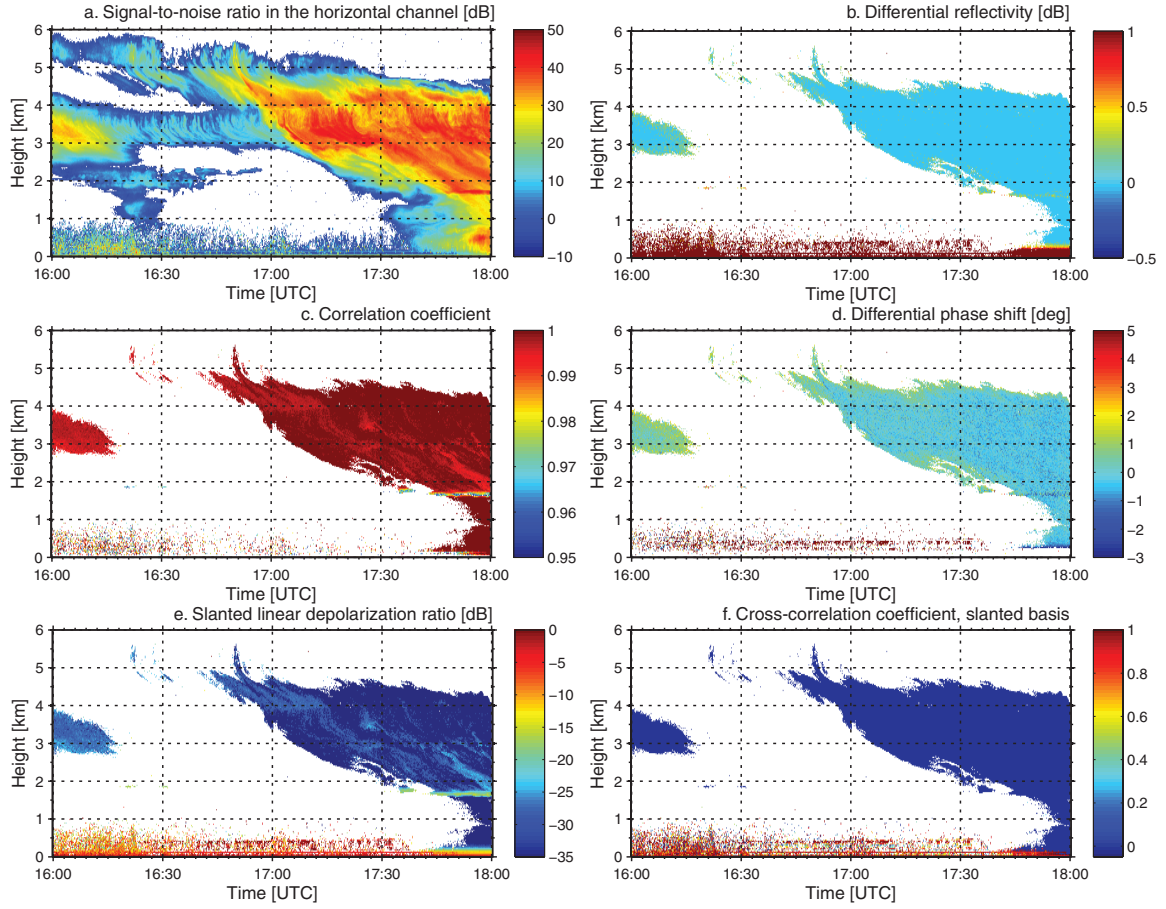


**Figure 4.5:** Time-height cross section of the signal-to-noise ratio in the horizontal channel (a), differential reflectivity  $Z_{DR}$  (b), correlation coefficient  $\rho_{hv}$  (c), differential phase shift  $\Phi_{DP}$  (d), slanted linear depolarization ratio SLDR (e), and cross-correlation coefficient  $\rho_s$  in the slanted basis for the measurements taken at Elmshorn, Germany, on 1 May 2014.

LDR [Lohmeier et al., 1997; Di Girolamo et al., 2012; Görsdorf et al., 2015]. Values of  $\rho_s$  for meteorological scatterers are 0, as it follows from theoretical considerations given in Sec. 3.2. Insects can be considered as point depolarizing targets and therefore produce high  $\rho_s$  (see Sec. 3.3).

Polarimetric variables obtained for the time period from 17:55 to 18:00 UTC and the height range from 500 m to 1700 m, where light rain was observed, are close to those that would be measured in rain by a hypothetical ideal radar, i.e.,  $Z_{DR} = 1$  (0 dB),  $\Phi_{DP} = 0^\circ$ ,  $\rho_{hv} = 1$ , SLDR = 0 ( $-\infty$  dB), and  $\rho_s = 0$  (in the limit approximation given in Sec. 3.2). For comparison and estimation of the antenna quality, values of polarimetric parameters without the correction for antenna coupling are shown in Table 4.1. These variables were calculated by inserting the elements  $A_S(\omega_p)$ ,  $B_S(\omega_p)$ , and  $C_S(\omega_p)$  instead of  $A'_S(\omega_p)$ ,  $B'_S(\omega_p)$ , and  $C'_S(\omega_p)$  in Eqs. (4.26)–(4.33).

**Table 4.1:** Polarimetric variables calculated without the correction for the antenna coupling and those that would be observed by an hypothetical ideal radar. Values are based on measurements with the vertically pointed cloud radar in light rain on 1 May 2014 that is shown in Fig. 4.5. The statistics are based on the height range from 500 to 1700 m and the time period from 17:55 to 18:00 UTC.

Variable	Mean value	Standard deviation	Theoretical value
$Z_{DR}$	1.011 (0.048 dB)	0.017	1 (0 dB)
$\rho_{hv}$	0.9976	$4.8 \times 10^{-4}$	1
$\Phi_{DP}$	$-0.16^\circ$	$0.35^\circ$	$0^\circ$
SLDR	$1.2 \times 10^{-3}$ ( $-29.3$ dB)	$2.2 \times 10^{-4}$	0 ( $-\infty$ dB)
$\rho_s$	0.089	0.046	0

## 4.7 Sensitivity issue

Splitting the transmitting power into two channels in the hybrid mode worsens the radar sensitivity by 3 dB. In the case when only power spectra  $B_{hh}(\omega_k)$  and  $B_{vv}(\omega_k)$  are available, non-coherent averaging can recover up to 1.5 dB [Skolnik, 1980]. The availability of the full coherency matrix permits the application of coherent averaging based on Eq. (4.15), which can potentially improve the radar sensitivity by up to 3 dB. Thus, the sensitivity loss due to splitting can be balanced out by the sensitivity gain due to coherent averaging. Applicability of the coherent averaging to weather radars was previously shown by Melnikov *et al.* [2011].

Coherent averaging can be applied when the received signals in the horizontal and vertical channels are in-phase. In the case of elliptical or circular polarization of the transmitted signal an additional phase shift can be introduced during processing to fulfill this requirement. As shown in Sec. 4.1, in our case the transmission phase difference is  $\Delta\varphi_T = -0.9^\circ$ , which is considered to be sufficiently low to neglect effects of the phase difference on SNR.

In Fig. 4.3b it can be seen that the mean noise levels in the receiving channels are different. This can hamper the procedure of increasing the sensitivity. Therefore, the mean noise levels were adjusted using the coefficient  $K_n$ :

$$K_n = \frac{N_h}{N_v}. \quad (4.34)$$

For the rain case on 1 May 2014  $K_n$  was found to be  $1.32 \pm 0.14$ . Long-term fluctuations of  $K_n$  are of the same order of magnitude as for  $K_a$ . Using  $K_n$  instead of the coefficient  $K_a$  in Eqs. (4.9) and (4.10), the elements  $B_{vv}(\omega_k)$  and  $\dot{B}_{hv}(\omega_k)$  were corrected for different noise levels, which were then inserted into Eq. (4.15) to perform the coherent averaging.

Another factor that can affect the utilization of Eq. (4.15) is the differential phase shift introduced by the propagation and backscattering properties of the scatterers. As mentioned in Sec. 4.1, the orientation of particles can be assumed to be distributed uniformly in the

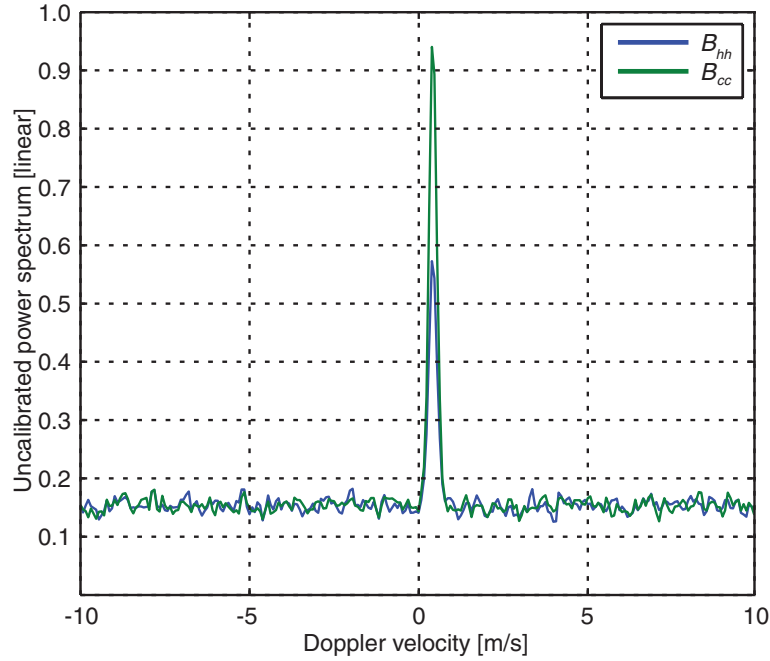


**Figure 4.6:** Power spectrum in the horizontal channel (blue line) and power spectrum after coherent averaging (green line). The same data as in Fig. 4.3 are used.

polarization plane when the radar is pointed vertically. In this case, both backscattering and propagation differential phase shift are 0. Nevertheless, differential phase effects should be accounted for in the case of utilization of the 35-GHz cloud radar at low elevations for precipitation observations. For instance, *Matrosov et al.* [1999] showed that at 35 GHz the propagation and backscattering differential phase shifts in rain stronger than 5 mm/hr can exceed  $1^\circ/\text{km}$  and  $5^\circ$ , respectively. In this thesis a correction for the differential phase shift introduced by scatterers is not considered.

The results of Eq. (4.15) are shown in Fig. 4.6 for an arbitrary example case. It can be seen that  $B_{cc}(\omega_k)$  has about two times higher signal power than  $B_{hh}(\omega_k)$ , while the standard deviations of noise are 0.01 and 0.011 (arbitrary units), respectively. The noise levels of  $B_{cc}(\omega_k)$  and  $B_{hh}(\omega_k)$  are the same. The power spectra  $B_{cc}(\omega_k)$  can be used for the standard processing, i.e., for the detection and the estimation of spectral moments. In this case, the total power transmitted by the radar instead of the power transmitted in the horizontal channel should be used for the calculation of reflectivity.

In Fig. 4.7 the height-time cross sections of SNR calculated from  $B_{hh}(\omega_k)$  and  $B_{cc}(\omega_k)$  are shown. For the thresholding and the SNR calculation the standard processing implemented in MIRA-35 cloud radar [*Görsdorf et al.*, 2015] was used. It can be seen that the coherent averaging results in more data points, which is especially of benefit for the detection efficiency of high-level clouds.

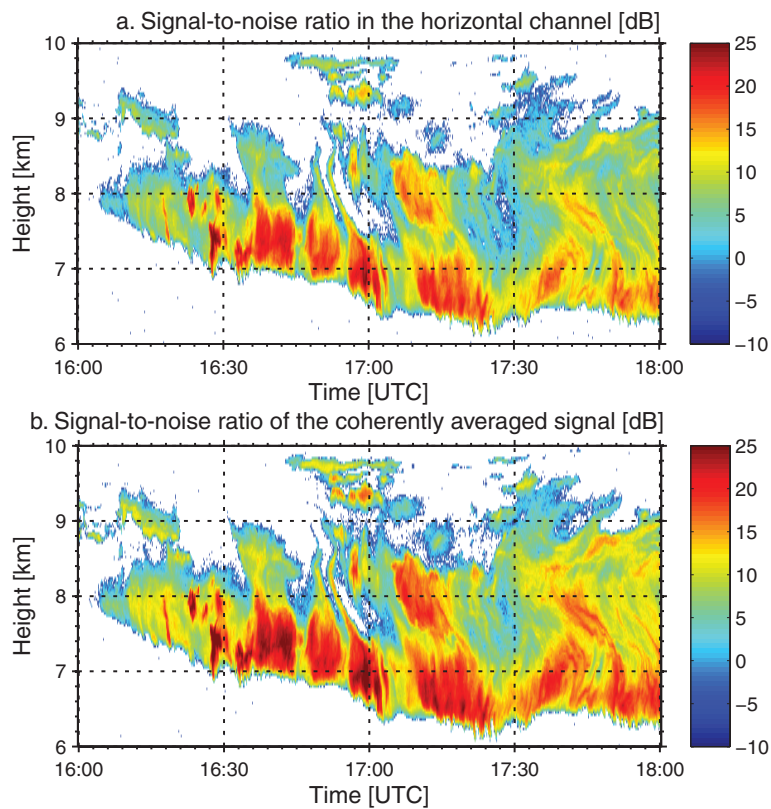


**Figure 4.7:** Time-height cross sections of signal-to-noise ratios calculated from  $B_{hh}$  (a) and  $B_{cc}$  (b) measured at Elmshorn, Germany, on 1 May 2014. The amount of data points (especially in high-level clouds) in panel (b) is higher in comparison with (a) because of higher sensitivity.

---

## Chapter 5

# Shape and orientation retrieval

In the previous chapter the implementation of the hybrid-mode cloud radar was described, which enables a registration of a set of polarimetric variables. Based on these polarimetric variables the current chapter presents an experimental quantitative characterization of the shape and orientation distribution of ice particles in clouds. The characterization utilizes measured and modeled elevation dependencies of the polarimetric parameters differential reflectivity and correlation coefficient. The approach presented in the following is based on a combination of established spheroidal models [Matrosov, 1991a; Ryzhkov, 2001; Bringi and Chandrasekar, 2001] that were developed to describe the polarimetric variables. The modeled parameters are polarizability ratio and degree of orientation, which can be assigned to certain particle orientations and shapes. The developed algorithm is applied to a measurement of the hybrid-mode cloud radar taken in the framework of the ACCEPT campaign at Cabauw, the Netherlands, on 20 October 2014. The material in this chapter is based on Myagkov *et al.* [2016a]. The modeling of polarimetric variables is explained in Sec. 5.1. The approach for the retrieval of the shape and orientation distribution is presented in Sec. 5.2. A case study showing the application of the method is discussed in Sec. 5.3.

### 5.1 Backscattering model

It is known that particles with sizes much smaller than the wavelength of a radar can be approximated by a spheroid. Matrosov [2015] shows that this approximation is valid in the case of ice-particle observations with cloud radars. Scattering properties of a spheroid are often described using the Jones representation in a linear polarization basis by a  $2 \times 2$  backscattering matrix:

$$\mathbf{S} = \begin{pmatrix} \dot{S}_{hh} & \dot{S}_{hv} \\ \dot{S}_{vh} & \dot{S}_{vv} \end{pmatrix}. \quad (5.1)$$


---

The elements of the backscattering matrix  $\mathbf{S}$  are calculated as follows [Bringi and Chandrasekar, 2001, Ch. 2]:

$$\dot{S}_{hh} = \frac{k_0^2}{4\pi\epsilon_0} [p_1 + (p_2 - p_1) \sin^2 \theta_p \sin^2 \varphi_p], \quad (5.2)$$

$$\dot{S}_{hv} = \dot{S}_{vh} = \frac{k_0^2}{4\pi\epsilon_0} \left[ \frac{(p_2 - p_1)}{2} (\cos \psi \sin^2 \theta_p \sin 2\varphi_p + \sin \psi \sin 2\theta_p \sin \varphi_p) \right], \quad (5.3)$$

$$\dot{S}_{vv} = \frac{k_0^2}{4\pi\epsilon_0} \left[ p_1 + (p_2 - p_1) \left( \cos^2 \psi \sin^2 \theta_p \cos^2 \varphi_p + \sin^2 \psi \cos^2 \theta_p + \frac{\sin 2\psi \sin 2\theta_p \cos \varphi_p}{2} \right) \right], \quad (5.4)$$

where  $k_0$  is the wavenumber,  $\epsilon_0$  is the vacuum permittivity, and  $\psi$  is the angle between the unit vector  $\mathbf{e}_z$  (see Fig. 3.1) and the zenith direction. The angle  $\psi$  is further denoted as the elevation angle.  $\theta_p$  and  $\varphi_p$  are angles defining the orientation of the spheroid, which is illustrated in Fig. 5.2.  $p_{1,2}$  are polarizability elements:

$$p_{1,2} = V\epsilon_0(\epsilon_r - 1)\Lambda_{1,2}. \quad (5.5)$$

In Eq. (5.5)  $V$  is the volume of the spheroid,  $\epsilon_r$  is the relative permittivity, and  $\Lambda_{1,2}$  can be found as follows:

$$\Lambda_{1,2} = \frac{1}{(\epsilon_r - 1)d_{1,2} + 1}, \quad (5.6)$$

where  $d_{1,2}$  are depolarizing factors. The depolarizing factors for prolate and oblate spheroids are described as follows:

$$d_2(\text{prolate}) = \frac{1 - b^2}{b^2} \left( -1 + \frac{1}{2b} \ln \frac{1+b}{1-b} \right); \quad b^2 = 1 - \left( \frac{1}{\xi_g} \right)^2, \quad \xi_g \geq 1, \quad (5.7)$$

$$d_2(\text{oblate}) = \frac{1 + f^2}{f^2} \left( 1 - \frac{1}{f} \tan^{-1} f \right); \quad f^2 = \left( \frac{1}{\xi_g} \right)^2 - 1, \quad 0 < \xi_g \leq 1, \quad (5.8)$$

$$d_1 = \frac{1 - d_2}{2}. \quad (5.9)$$

In Eqs. (5.7) and (5.8)  $\xi_g$  is the axis ratio of the spheroid, which is defined as shown in Fig. 5.1.

In the following, only ice particles are considered. In the microwave region the real part of  $\epsilon_r$  for pure ice is approximately 3.168. The imaginary part is several orders of magnitude lower than the real part [Ray, 1972] and, therefore, it is neglected. In this case, the elements of the backscattering matrix  $\mathbf{S}$  are real numbers.

Further, the polarizability ratio is defined as:

$$\xi_e = \frac{p_2}{p_1}. \quad (5.10)$$

$\xi_e$  is a function of permittivity and axis ratio  $\xi_g$  and is independent of particle volume  $V$ . As it was shown in the review of Oguchi [1983], the permittivity and apparent density of

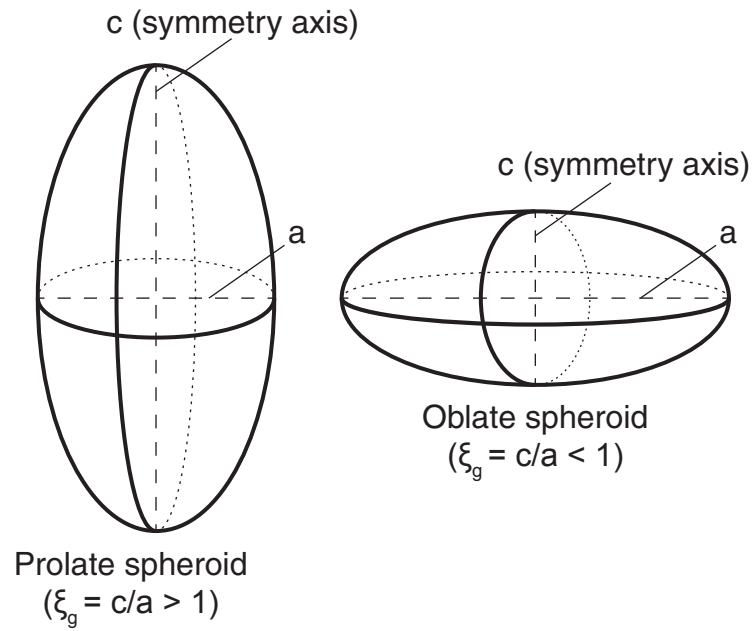


**Figure 5.1:** Geometry of prolate and oblate spheroids.

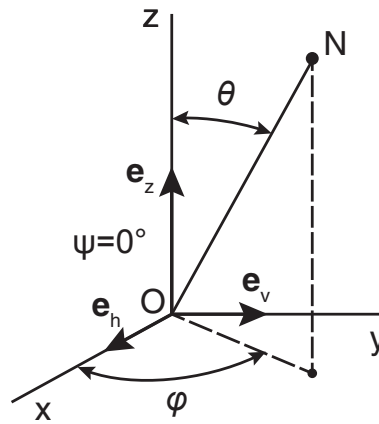


**Figure 5.2:** Geometry of spheroid orientation, adopted from *Matrosov* [1991a]. The description polarization basis is shown for the case of  $\psi = 0^\circ$ .  $ON$  is the symmetry axis of the spheroid.

ice crystals are related almost linearly. Apparent ice density  $\rho_a$  characterizes the ratio of ice and air within the approximating spheroidal particle (see Fig. 5.3). Numerical values of  $\xi_g$  and  $\rho_a$  for ice crystals are considered in more details in Chapter 6. The relationship between  $\xi_e$ ,  $\xi_g$ , and  $\rho_a$  is shown in Fig. 5.4.

The backscattering matrix of  $N$  particles dispersed in a certain volume can be written

as follows:

$$\mathbf{S}_\Sigma = \sum_{j=1}^N \mathbf{S}_j e^{2ik_0 r_j}, \quad (5.11)$$

where  $\mathbf{S}_j$  and  $r_j$  are the backscattering matrix and the distance of the  $j$ -th particle from the radar, respectively. Assuming complex amplitudes of the horizontal and vertical components of the transmitted signal  $\dot{E}_{th} = \dot{E}_{tv} = 1$ , the polarization state corresponds to the one of a wave emitted by an ideal hybrid-mode radar with a transmission phase difference  $\Delta\varphi_T = 0^\circ$ . The complex amplitudes of the horizontal  $\dot{E}_h$  and vertical  $\dot{E}_v$  components of the received

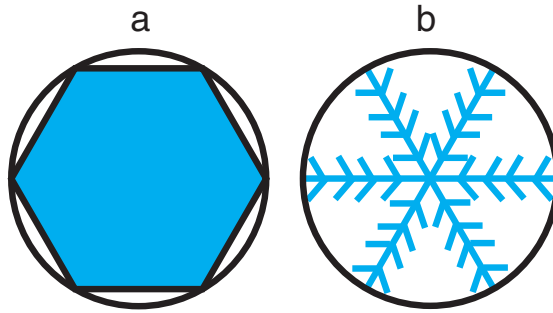


**Figure 5.3:** Schematic images of a hexagonal plate (a) and a dendrite (b) circumscribed by spheroids. The hexagonal plate covers the major part of the spheroid's volume and is characterized by high apparent ice density. The dendrite is characterized by low apparent ice density because the approximating spheroid is mainly filled with air.

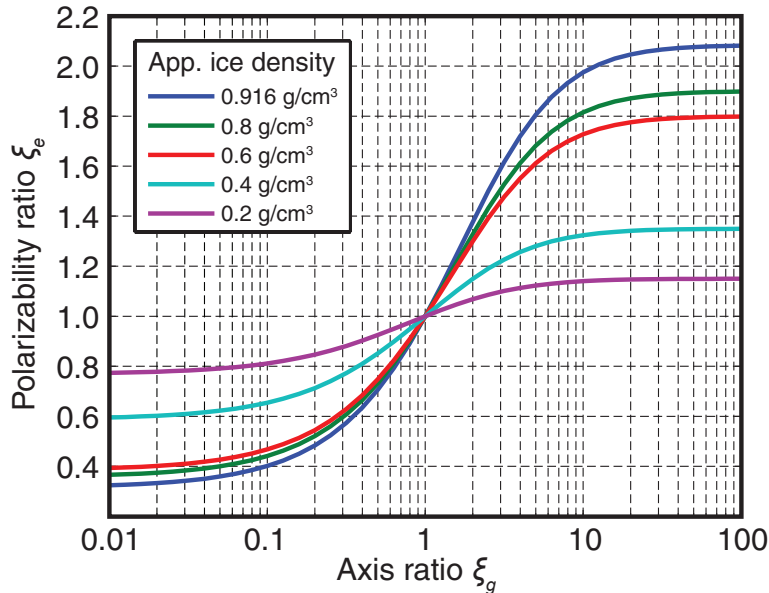


**Figure 5.4:** Dependency of polarizability ratio  $\xi_e$  on axis ratio  $\xi_g$  of a spheroid for different apparent ice densities  $\rho_a$ .



signal can be derived as follows:

$$\dot{E}_h = \left( \dot{S}_{hh} \right)_\Sigma \dot{E}_{th} + \left( \dot{S}_{hv} \right)_\Sigma \dot{E}_{tv}, \quad (5.12)$$

$$\dot{E}_v = \left( \dot{S}_{hv} \right)_\Sigma \dot{E}_{th} + \left( \dot{S}_{vv} \right)_\Sigma \dot{E}_{tv}, \quad (5.13)$$

where  $\left( \dot{S}_{hh} \right)_\Sigma$ ,  $\left( \dot{S}_{hv} \right)_\Sigma$ ,  $\left( \dot{S}_{vh} \right)_\Sigma$ , and  $\left( \dot{S}_{vv} \right)_\Sigma$  are the elements of the backscattering matrix  $\mathbf{S}_\Sigma$ .

The implementation of the subsequent modeling approach is based on the following assumptions:

1.  $V$ ,  $\theta_p$ ,  $\varphi_p$ ,  $\xi_g$  are not correlated with each other.
2. All particles have the same axis ratio  $\xi_g$ .
3.  $\varphi_p$  is uniformly distributed in the range from  $-\pi$  to  $\pi$ .
4. The scattering is non-coherent.
5. Multiple scattering is neglected.
6. Propagation effects such as differential attenuation and specific differential phase shift are neglected.

It is assumed that particles falling with the same terminal velocity have comparable size, shape, and apparent ice density. In this case, the first two assumptions are reasonable when polarimetric variables for a certain spectral line are modeled.

Under all above-mentioned assumptions the elements of the coherency matrix can then be found as follows:

$$\hat{B}_{hh} = \langle \dot{E}_h \dot{E}_h^* \rangle = F_1 (1 + P_1 T_1 + F_2 P_2 T_1 + F_3 P_2 T_2), \quad (5.14)$$

$$\hat{B}_{vv} = \langle \dot{E}_v \dot{E}_v^* \rangle = F_1 (1 + F_4 P_1 + F_5 P_1 T_1 + F_6 P_2 + F_7 P_2 T_1 + F_8 P_2 T_2), \quad (5.15)$$

$$\hat{B}_{hv} = \langle \dot{E}_h \dot{E}_v^* \rangle = F_1 (1 + F_9 P_1 T_1 + F_{10} P_1 + F_{10} P_2 T_1 + F_{11} P_2 T_2). \quad (5.16)$$

In Eqs. (5.14)–(5.16) the following parameters are used:

$$F_1 = N \langle p_1 \rangle \left( \frac{k_0^2}{4\pi\epsilon_0} \right)^2, \quad (5.17)$$

$$F_2 = \frac{1}{2} \sin^2 \psi, \quad (5.18)$$

$$F_3 = \frac{(4 - 5 \sin^2 \psi)}{8}, \quad (5.19)$$

$$F_4 = 4F_2, \quad (5.20)$$

$$F_5 = \cos^2 \psi - 2 \sin^2 \psi, \quad (5.21)$$

$$F_6 = \sin^4 \psi, \quad (5.22)$$

$$F_7 = \frac{7}{2} \sin^2 \psi - 5 \sin^4 \psi, \quad (5.23)$$

$$F_8 = \frac{1}{2} - \frac{35}{8} \sin^2 \psi + \frac{35}{8} \sin^4 \psi, \quad (5.24)$$

$$F_9 = \frac{1}{2} + \frac{1}{2} F_5, \quad (5.25)$$

$$F_{10} = 2F_2, \quad (5.26)$$

$$F_{11} = \frac{1}{4} \cos^2 \psi - \sin^2 \psi, \quad (5.27)$$

$$P_1 = \xi_e - 1, \quad (5.28)$$

$$P_2 = (\xi_e - 1)^2, \quad (5.29)$$

$$T_1 = \langle \sin^2 \theta_p \rangle, \quad (5.30)$$

$$T_2 = \langle \sin^4 \theta_p \rangle. \quad (5.31)$$

Averaging in Eqs. (5.17), (5.30), and (5.31) is performed over  $N$  particles.

The probability density function of orientation angle  $\theta_p$  is modeled by using the function adopted from *Kanareykin et al.* [1966]:

$$W(\Theta) = \frac{1 - R^2}{2\pi} \left[ \frac{1}{1 - R^2 \cos^2 2\Theta} + R \cos 2\Theta \frac{\frac{\pi}{2} + \arcsin(R \cos 2\Theta)}{(1 - R^2 \cos^2 2\Theta)^{3/2}} \right], \quad -\frac{\pi}{2} \leq \Theta \leq \frac{\pi}{2}, \quad (5.32)$$

where  $R$  is a factor defining the width of the distribution and  $\Theta = \theta_p - \theta_0$ , with  $\theta_0$  being the preferable orientation of particles. The preferable orientation is considered to be horizontal, i.e.,  $\theta_0 = 0$  for oblate spheroids and  $\theta_0 = \pi/2$  for prolate spheroids, which is consistent with *Mitchell* [1996]. The advantage of using Eq. (5.32) is that it permits us to model a variety of cases, including a Delta-distribution ( $R = 1$ ) as well as uniform ( $R = 0$ ) and fully chaotic distributions. In Fig. 5.5  $W(\Theta)$  for different values of  $R$  is shown.

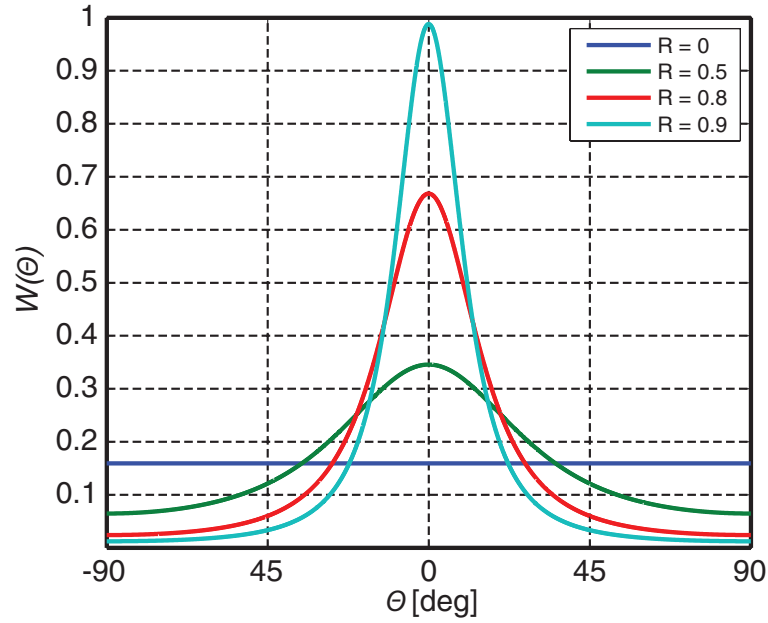


**Figure 5.5:** Probability density function of  $\Theta$  for different values of  $R$ . Adopted from *Kanareykin et al.* [1966].

Using Eqs. (5.30)–(5.32) the parameters  $T_1$  and  $T_2$  can be calculated as follows:

$$T_1 = \int_{-\pi/2}^{\pi/2} \sin^2(\Theta + \theta_0) W(\Theta) d\Theta, \quad (5.33)$$

$$T_2 = \int_{-\pi/2}^{\pi/2} \sin^4(\Theta + \theta_0) W(\Theta) d\Theta. \quad (5.34)$$

The calculated values of  $T_1$  and  $T_2$  are shown in Fig. 5.6. For further analysis it is convenient to use the degree of orientation  $\kappa$ , introduced in *Hendry et al.* [1976]. The degree of orientation  $\kappa$  is related to the parameter  $T_1$  as follows:

$$\kappa = 1 - 2T_1. \quad (5.35)$$

*Hendry et al.* [1976] considered  $\kappa$  only for  $\theta_0 = 0$ , for which  $\kappa$  lies in the range from 0 to 1. In the case  $\theta_0 = \pi/2$  values of  $\kappa$  are in the range from  $-1$  to 0. Thus, the absolute value of  $\kappa$  represents the degree of orientation, while the sign indicates the preferable orientation of the symmetry axis (either vertical or horizontal, see Figs. 5.1 and 5.2).

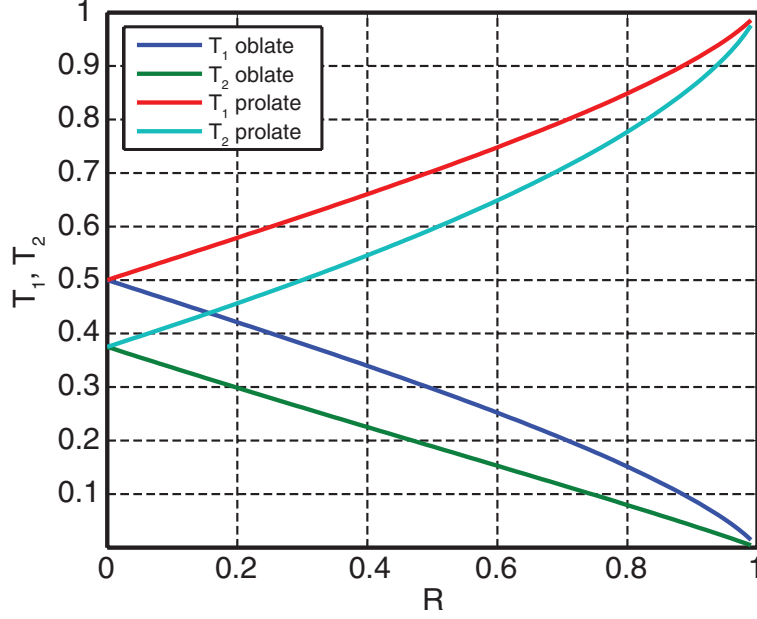


**Figure 5.6:** Dependency of  $T_1$  and  $T_2$  on  $R$  for oblate and prolate spheroids.

Finally, the polarimetric variables can be calculated from Eqs. (5.14)–(5.16):

$$\hat{Z}_{DR} = \frac{\hat{B}_{hh}}{\hat{B}_{vv}}, \quad (5.36)$$

$$\hat{\rho}_{hv} = \frac{|\hat{B}_{hv}|}{\sqrt{\hat{B}_{hh}\hat{B}_{vv}}}, \quad (5.37)$$

$$\widehat{\text{SLDR}} = \frac{\hat{B}_{hh} + \hat{B}_{vv} - 2\text{Re}(\hat{B}_{hv})}{\hat{B}_{hh} + \hat{B}_{vv} + 2\text{Re}(\hat{B}_{hv})}, \quad (5.38)$$

$$\hat{\rho}_s = \frac{|\hat{B}_{hh} - \hat{B}_{vv} + 2i\text{Im}(\hat{B}_{hv})|}{\sqrt{[\hat{B}_{hh} + \hat{B}_{vv} - 2\text{Re}(\hat{B}_{hv})][\hat{B}_{hh} + \hat{B}_{vv} + 2\text{Re}(\hat{B}_{hv})]}}. \quad (5.39)$$

Here, the  $\wedge$ -sign indicates that the parameters are modeled.

## 5.2 Retrieval technique

Melnikov and Straka [2013] proposed a shape and orientation retrieval algorithm based on  $Z_{DR}$  and  $\rho_{hv}$  observed by a weather radar. The authors showed that the algorithm is applicable for cloud areas with  $Z_{DR} > 4$  dB, where the backscatter signal is dominated by oblate particles. When  $Z_{DR} < 4$  dB the algorithm cannot distinguish between oblate and prolate particles.

*Matrosov* [1991a] and *Matrosov et al.* [2012] showed that an appropriate classification of ice particles in clouds requires scanning over the elevation angle. Therefore, the shape and orientation retrieval described below requires measurement of differential reflectivity and correlation coefficient in dependence on elevation angle. During the ACCEPT campaign, elevation scans from  $-60^\circ$  to  $60^\circ$  were performed ( $0^\circ$  corresponds to the zenith pointing). Natural obstacles at the measurement site limited scanning at lower elevation angles. Thus, from every scan cycle two half-scans are available for the shape classification.

By using Eqs. (5.36) – (5.39) look-up tables of  $\hat{Z}_{DR}(\kappa, \psi, \xi_e)$ ,  $\hat{\rho}_{hv}(\kappa, \psi, \xi_e)$ ,  $\widehat{\text{SLDR}}(\kappa, \psi, \xi_e)$ , and  $\hat{\rho}_s(\kappa, \psi, \xi_e)$  can be calculated. Values from  $-1$  to  $1$  for  $\kappa$ , from  $-60^\circ$  to  $60^\circ$  for  $\psi$ , and from  $0.3$  to  $2.3$  for  $\xi_e$  are used. The chosen range of  $\xi_e$  covers the possible values for ice shown in Fig. 5.4. The cross-sections of modeled polarimetric variables are presented in Fig. 5.7. Left and right columns in Fig. 5.7 represent elevation angles  $\psi$  of  $60^\circ$  and  $0^\circ$ , respectively. Values of  $\kappa = -1$  (upper part of diagrams) characterize particles with horizontally oriented symmetry axis;  $\kappa = 0$  is typical for uniformly distributed orientation angles  $\theta_p$ ;  $\kappa = 1$  (lower part of diagrams) describes a vertically oriented symmetry axis of particles. It should be noticed that  $\kappa \sim -0.4$  specifies the so-called fully chaotic orientation of particles [*Ryzhkov*, 2001], which can be considered as a special case of reflection symmetry [*Nghiem et al.*, 1992]. In this case, the polarimetric variables do not depend on  $\psi$ , and  $Z_{DR}$  and  $\rho_s$  are 0 dB and 0, respectively. Values of  $\xi_e < 1$  designate oblate particles;  $\xi_e = 1$  represents spherical particles or particles with low density;  $\xi_e > 1$  correspond to prolate particles (see Fig. 5.4).

In Fig. 5.7a  $Z_{DR}$  is larger than 0 dB in the lower left and in the upper right corners of the diagram. These corners correspond to horizontally aligned oblate and prolate particles, respectively. In contrast, in the upper left and in the lower right corners particles are oriented vertically and thus produce  $Z_{DR}$  lower than 0 dB. Additionally, oblate particles can produce larger  $Z_{DR}$  than prolate ones, in agreement with *Hogan et al.* [2002] and *Melnikov and Straka* [2013]. For zenith pointing (Fig. 5.7b)  $Z_{DR}$  values are 0 dB because of the reflection symmetry [*Nghiem et al.*, 1992]. Figs. 5.7c and d show that  $\hat{\rho}_{hv}$  is equal to 1 for spherical and horizontally aligned oblate particles. At  $\psi = 60^\circ$  values of  $\hat{\rho}_{hv}$  decrease with decreasing  $|\kappa|$ . This behavior is especially noticeable for particles with  $\xi_e < 0.5$  and  $\xi_e > 1.8$ . The relation between  $\hat{\rho}_{hv}$  and  $|\kappa|$  is consistent with the findings of *Matrosov* [1991b]. Fig. 5.7e shows that values of  $\widehat{\text{SLDR}}$  are dominated by  $\xi_e$  and only slightly depend on  $\kappa$ . This feature was previously described in *Reinking et al.* [2002] and *Matrosov et al.* [2012]. *Galletti and Zrnica* [2012] showed that in hybrid mode at zenith pointing  $\hat{\rho}_{hv}$  is equal to the degree of polarization. In this case,  $\widehat{\text{SLDR}}$  and  $\hat{\rho}_{hv}$  can be related as follows:

$$\hat{\rho}_{hv} \sim 1 - 2\widehat{\text{SLDR}}. \quad (5.40)$$

The relation given by Eq. (5.40) can be clearly seen in Figs. 5.7d and f. Fig. 5.7g shows that  $\hat{\rho}_s$  is mostly defined by  $\kappa$ , i.e. by the orientation of particles. This was previously found

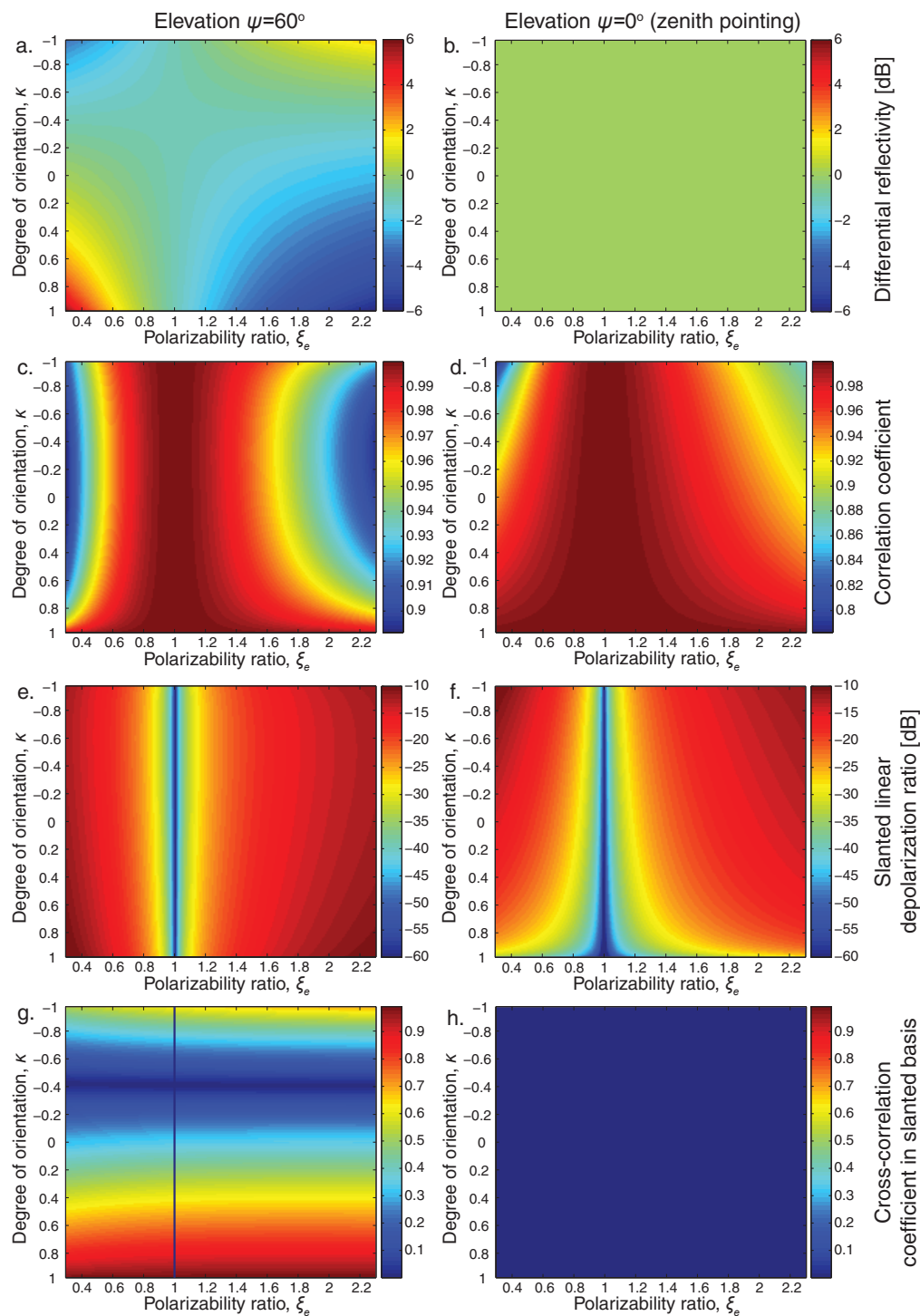


**Figure 5.7:** Modeled differential reflectivity  $\hat{Z}_{DR}$  (a,b), correlation coefficient  $\hat{\rho}_{hv}$  (c,d), slanted linear depolarization ratio  $\widehat{\text{SLDR}}$  (e,f), and cross-correlation coefficient in the slanted basis  $\hat{\rho}_s$  (g,h).

by *Ryzhkov et al.* [2002]. For spherical particles ( $\xi_e = 1$ ) the limit approximation  $\hat{\rho}_s = 0$  [*Myagkov et al.*, 2015] is used. As mentioned above  $\hat{\rho}_s$  is equal to 0 in the case of reflection symmetry, i.e., when  $\psi = 0^\circ$  (Fig. 5.7h).

In Chapter 4 it was shown that pairs of polarimetric variables  $Z_{DR}$  and  $\rho_{hv}$ , and SLDR and  $\rho_s$  characterize the same received wave in the Cartesian and slanted polarization basis, respectively. Thus,  $Z_{DR}$  and  $\rho_{hv}$  can be calculated from SLDR and  $\rho_s$  and vice versa. Therefore, the full set of four polarimetric variables is not necessary. In this thesis  $Z_{DR}$  and  $\rho_{hv}$  were chosen for the retrieval. Nevertheless, the same approach can be applied to SLDR and  $\rho_s$ , which can be measured directly by cloud radars operating in SLDR mode.

The Doppler velocity measured by a cloud radar is defined not only by the terminal velocity of particles but also by air motion. Thus, Doppler spectra measured at different elevation angles usually have different shapes and mean values. In the following, it is however assumed that the spectrum maximums (spectrum peaks), measured at a certain altitude and at different elevation angles, correspond to particles of similar microphysical properties.

Due to the spatial inhomogeneity of a cloud or in the case of low SNR, some data points in a half-scan can be missing. Also some altitudes cannot be reached by the radar at certain elevation angles. Therefore, the algorithm is only applied to altitudes where more than 50 % of the data points of polarimetric variables in a half-scan are present.

For simplicity, the retrieval is described for one altitude only. Denotations  $Z_{DR}(\psi)$  and  $\rho_{hv}(\psi)$  correspond to differential reflectivity and correlation coefficient calculated for the maximum spectral line at elevation angle  $\psi$ , respectively. Using the measured polarimetric variables and the look-up tables of modeled values, the following error functions are calculated:

$$E_{ZDR}(\kappa, \xi_e) = \int_{\Psi} \left| Z_{DR}(\psi) - \hat{Z}_{DR}(\kappa, \psi, \xi_e) \right|^2 d\psi, \quad (5.41)$$

$$E_{RHV}(\kappa, \xi_e) = \int_{\Psi} \left| \rho_{hv}(\psi) - \hat{\rho}_{hv}(\kappa, \psi, \xi_e) \right|^2 d\psi, \quad (5.42)$$

where  $\Psi$  represents elevation angles  $\psi$  for a certain half-scan. Eqs. (5.8) and (5.7) show that prolate and oblate particles have different scattering properties and therefore a quantitative characterization implies knowledge of the predominant shape. In order to classify particles as either prolate or oblate the minimum of  $E_{ZDR}(\kappa, \xi_e)$  is searched. Values of  $\kappa$  and  $\xi_e$  with corresponding  $E_{ZDR}(\kappa, \xi_e)$  that do not exceed the minimum  $E_{ZDR}$  by a factor of 1.1 are defined. For these values of  $\kappa$  and  $\xi_e$  the lowest value of  $E_{RHV}(\kappa, \xi_e)$  is determined. In the case when the minimum of  $E_{RHV}$  corresponds to  $\xi_e \leq 1$ , particles are classified as oblate spheroids. Otherwise, the particles are prolate spheroids. It should be noted that without the correction for the antenna coupling (see Sec. 4.5) the algorithm cannot reliably discriminate spheroids with polarizability ratios in the range from 0.8 to 1.2.

After the classification  $\xi_e$  and  $\kappa$  for every elevation angle within ranges from  $30^\circ$  to  $60^\circ$  and from  $-60^\circ$  to  $-30^\circ$  are determined. These ranges have been chosen considering the fact that polarimetric variables do not allow for a reliable discrimination between different properties of particles at elevation angles close to the zenith. Further, the following error function is calculated:

$$E_s(\kappa, \psi, \xi_e) = \left| Z_{DR}(\psi) - \hat{Z}_{DR}(\kappa, \psi, \xi_e) \right|^2 + [10 |\rho_{hv}(\psi) - \hat{\rho}_{hv}(\kappa, \psi, \xi_e)|]^2. \quad (5.43)$$

The weighting factor in Eq. (5.43) has not been optimized. It was set to 10 considering that errors in  $Z_{DR}$  are about one order of magnitude higher than errors in  $\rho_{hv}$ . For every elevation angle  $\psi$  values of  $\xi_e$  and  $\kappa$ , corresponding to the minimum of the function  $E_s(\kappa, \psi, \xi_e)$ , are found. It is emphasized that the retrieval allows for the estimation of the polarizability ratio  $\xi_e$ . The estimation of the exact axis ratio  $\xi_g$  from  $\xi_e$  requires knowledge of the apparent density (see Fig. 5.4) of ice crystals, which has to be assumed or measured.

### 5.3 Case study

In this section a case study is presented to demonstrate the applicability of MIRA-35 with hybrid mode for the particle classification technique described above. The dataset was acquired during the ACCEPT campaign, which was conducted at Cabauw, the Netherlands, in October and November 2014. The campaign is described in more detail in Chapter 6.

Throughout the ACCEPT campaign the radar was operated with the number of averaged spectra  $N_s = 20$ , which corresponds to an averaging time of 1 s. A scan cycle that was performed by the hybrid-mode MIRA is shown in Fig. 5.8. Within the 15-min period the radar performed two elevation scans from  $-60^\circ$  to  $60^\circ$  at an angular speed of  $0.5^\circ \text{s}^{-1}$ . The two scans were conducted perpendicular to each other in azimuth direction. Other details of the scan cycle are not related to this thesis and are not considered.

In Fig. 5.9 range-altitude cross sections of SNR, differential reflectivity, and correlation coefficient calculated for the maximum spectral lines are shown. These observations were taken in one azimuth plane from 18:16 to 18:20 UTC on 20 October 2014. Two cloud layers at 2.7–3.5 km and 4.0–5.2 km height are visible. These layers are denoted as 1 and 2, respectively. Between the layers a clear gap is present, thus seeding of ice crystals from the upper layer into the lower layer [Rutledge and Hobbs, 1984] can be assumed to be absent.

In Figs. 5.10 and 5.11 a detailed analysis of the case introduced in Fig. 5.9 is presented for altitudes of 3.0 and 4.7 km (layer 1 and 2), respectively. Well-pronounced elevation dependencies of the differential reflectivity can be seen for both layers. At elevation angles of  $|\psi| = 60^\circ$  the differential reflectivity reaches values of  $\sim 3$  dB and  $\sim 5$  dB for the layers 1 and 2, respectively. In vertical pointing direction ( $|\psi| = 0^\circ$ ) the differential reflectivity is



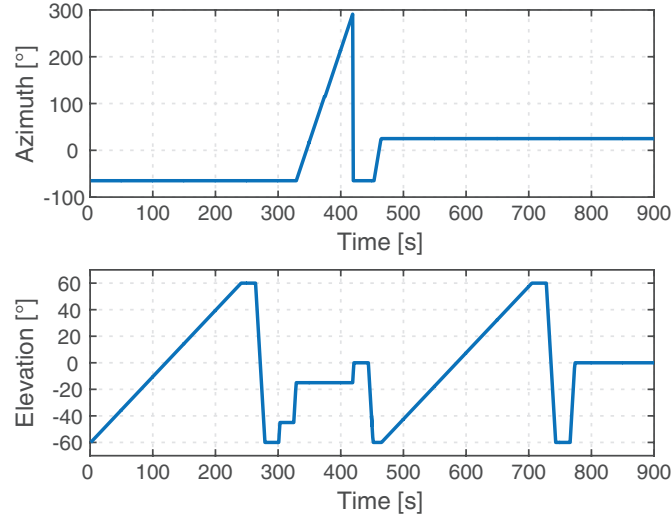


**Figure 5.8:** One period of the scan cycle of the hybrid-mode MIRA used during the ACCEPT campaign. Azimuth angles are given with respect to the north direction. Elevation angle of  $0^\circ$  corresponds to the zenith.

close to 0.5 dB and 0 dB, respectively. Thus, for both layers the differential reflectivity has its minimal value at  $0^\circ$  elevation and increases at higher  $|\psi|$ .

In contrast to the differential reflectivity, the elevation dependencies of the correlation coefficient have different behavior for layers 1 and 2 (Figs. 5.10b and 5.11b). In layer 1  $\rho_{hv}$  has its minimum at  $|\psi| = 0^\circ$ , whereas it shows increased values at higher  $|\psi|$ . In layer 2  $\rho_{hv}$  has a maximum at  $|\psi| = 0^\circ$ , while at higher  $|\psi|$  the values of  $\rho_{hv}$  are slightly lower.

Figs. 5.10c and d and 5.11c and d show the error functions  $E_{ZDR}(\kappa, \xi_e)$  and  $E_{RHV}(\kappa, \xi_e)$ , respectively. The algorithm described in Sec. 5.2 is used to distinguish between oblate and prolate particles at a certain altitude. The polarizability ratio determined using Figs. 5.10c and d is  $\sim 1.6$ , while the one from Figs. 5.11c and d is  $\sim 0.4$ . Thus, the spheroid types of the ice particles observed in layer 1 (3.0 km) and 2 (4.7 km) are classified as prolate and oblate, respectively.

After the classification of the spheroid type the polarizability ratio  $\xi_e$  and the degree of orientation  $\kappa$  are retrieved for every elevation angle in the range from  $30^\circ \leq |\psi| \leq 60^\circ$ . Using the obtained values mean and standard deviation of  $\xi_e$  and  $\kappa$  are calculated for every altitude. Standard deviations of  $\xi_e$  and  $\kappa$  characterize differences of the corresponding parameters for particle populations observed at different elevation angles. In order to estimate the influence of uncertainties in  $Z_{DR}$  and  $\rho_{hv}$  on the retrieval of  $\xi_e$ , we applied the algorithm to measurements in light rain on 7 November 2015, from 20:30 to 21:00 UTC. The precipitation intensity during the chosen time period was about  $1 \text{ mm hr}^{-1}$ , as it was observed by a

disdrometer on-site. We assume that raindrops have a spherical shape which is characterized by the polarizability ratio of 1. Values of retrieved  $\xi_e$  were mainly  $1.00 \pm 0.02$ .

The algorithm was applied to 6-hour time series of scanning polarimetric observations from 13:30 to 19:30 UTC on 20 October 2014. The results are presented in Fig. 5.12. Fig. 5.12a shows the time-height cross section of the equivalent radar reflectivity factor

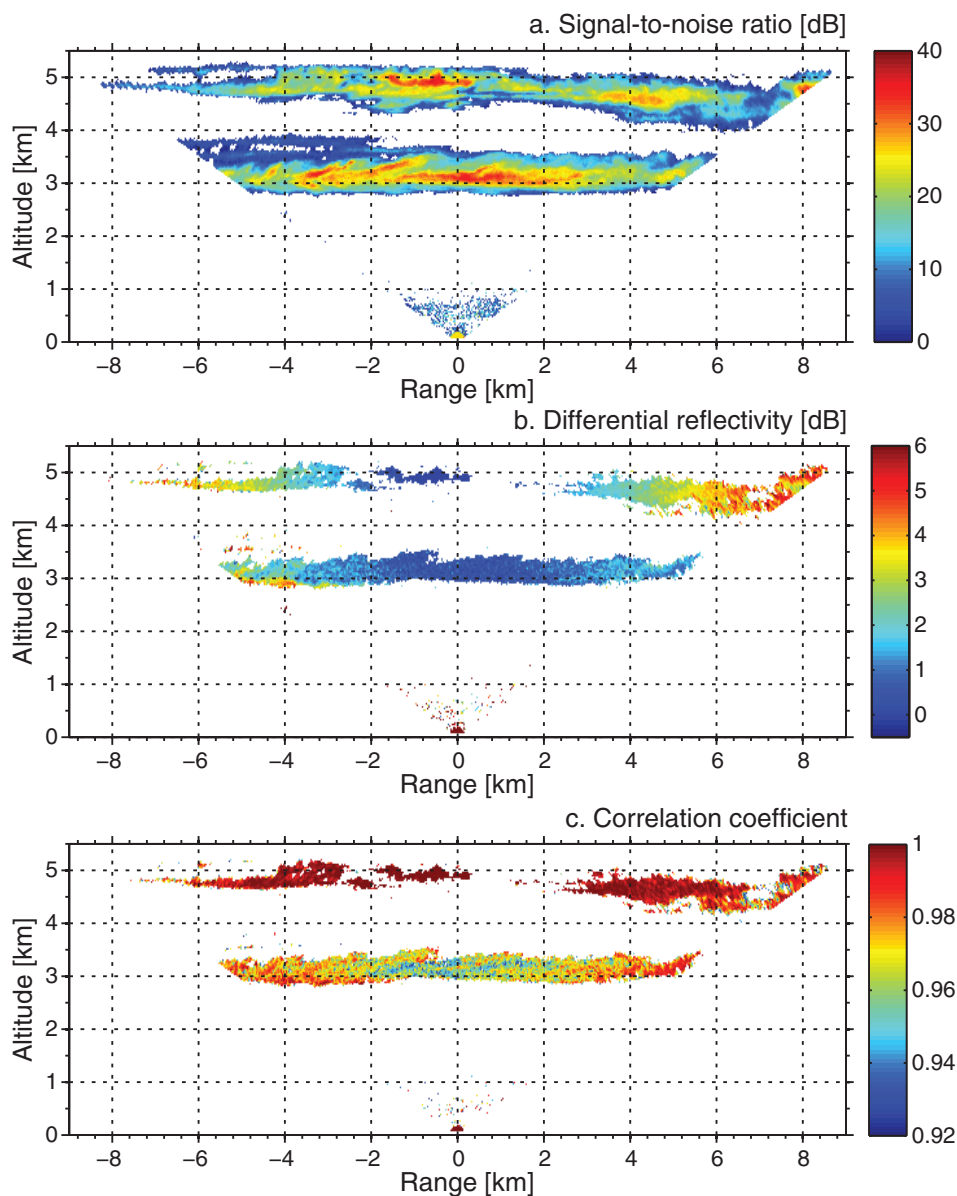


**Figure 5.9:** Range-altitude cross sections of (a) signal-to-noise ratio, (b) differential reflectivity  $Z_{DR}$ , and (c) correlation coefficient  $\rho_{hv}$  taken at Cabauw, the Netherlands, from 18:16 to 18:20 UTC on 20 October 2014. Shown parameters are calculated for the maximum spectral lines (spectral peaks).

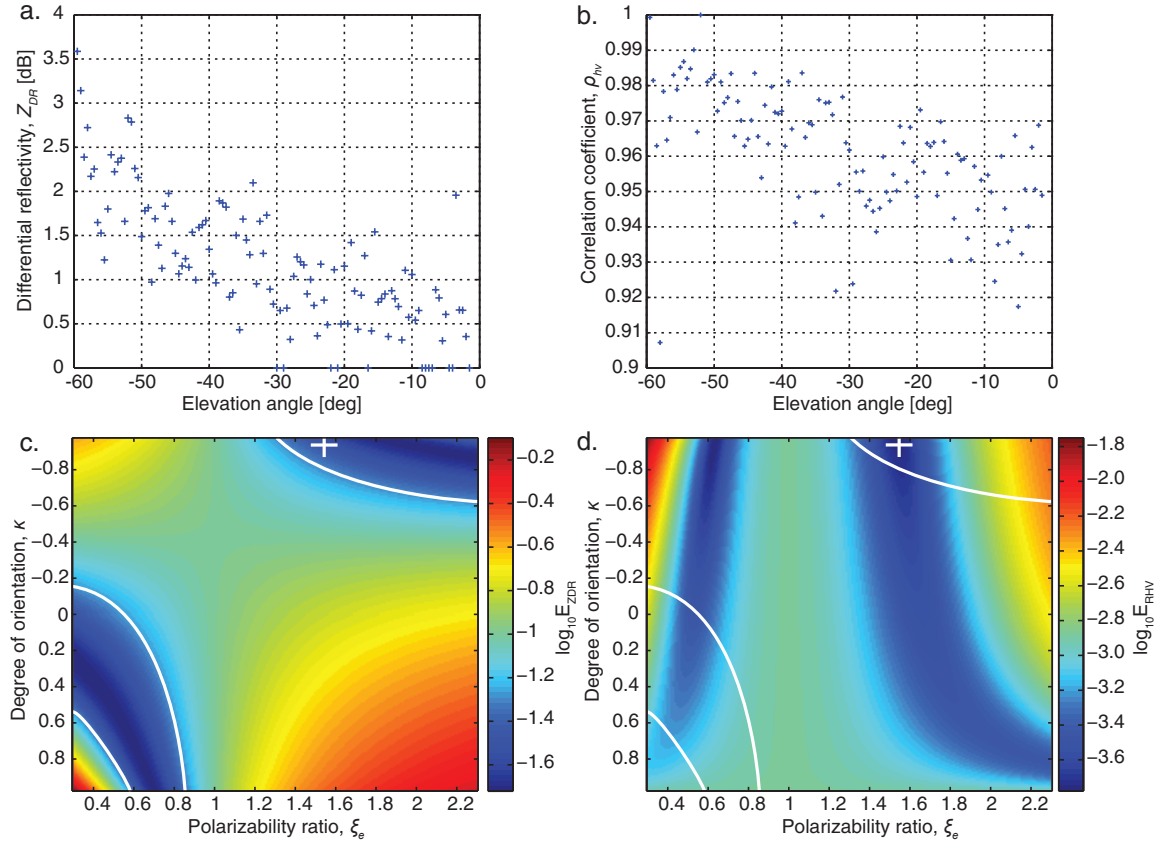


**Figure 5.10:** Measured elevation dependencies of differential reflectivity (a) and correlation coefficient (b) and logarithms of  $E_{ZDR}$  (c) and  $E_{RHV}$  (d). Measured data correspond to 3 km height of the left half-scan of Fig. 5.9. White contours indicate areas with  $E_{ZDR}(\kappa, \xi_e)$  not exceeding the minimum  $E_{ZDR}$  by a factor of 1.1. White crosses mark the results of the optimization algorithm. According to the classification scheme described in the text, this case corresponds to a polarizability ratio of 1.6 (prolate spheroids).

from a collocated vertically pointed cloud radar MIRA-35 with LDR mode. The time period corresponding to the elevation scan that is shown in Fig. 5.9 is indicated by the red rectangle in Fig. 5.12a. Several cloud layers at different heights were observed during the measurement. High-level clouds with a cloud top at around 8 km height were observed from 13:30 to 14:30 UTC and from 15:00 to 17:00 UTC. Reflectivity values for these cloud layers mostly exceeded  $-10$  dBZ, which is high enough to calculate polarimetric variables. From 15:00 to 19:30 UTC a thick mid-level cloud with a top at 5 km height was observed. At 16:40 UTC strong ice formation, indicated by high values of the radar reflectivity, was registered. Melting of ice particles resulted in a short precipitation event reaching the ground. Later, the cloud experienced seeding from the high-level cloud above. From 18:15 UTC the cloud split into two thin cloud layers with cloud tops at 5 and 3 km height. Different ambient conditions

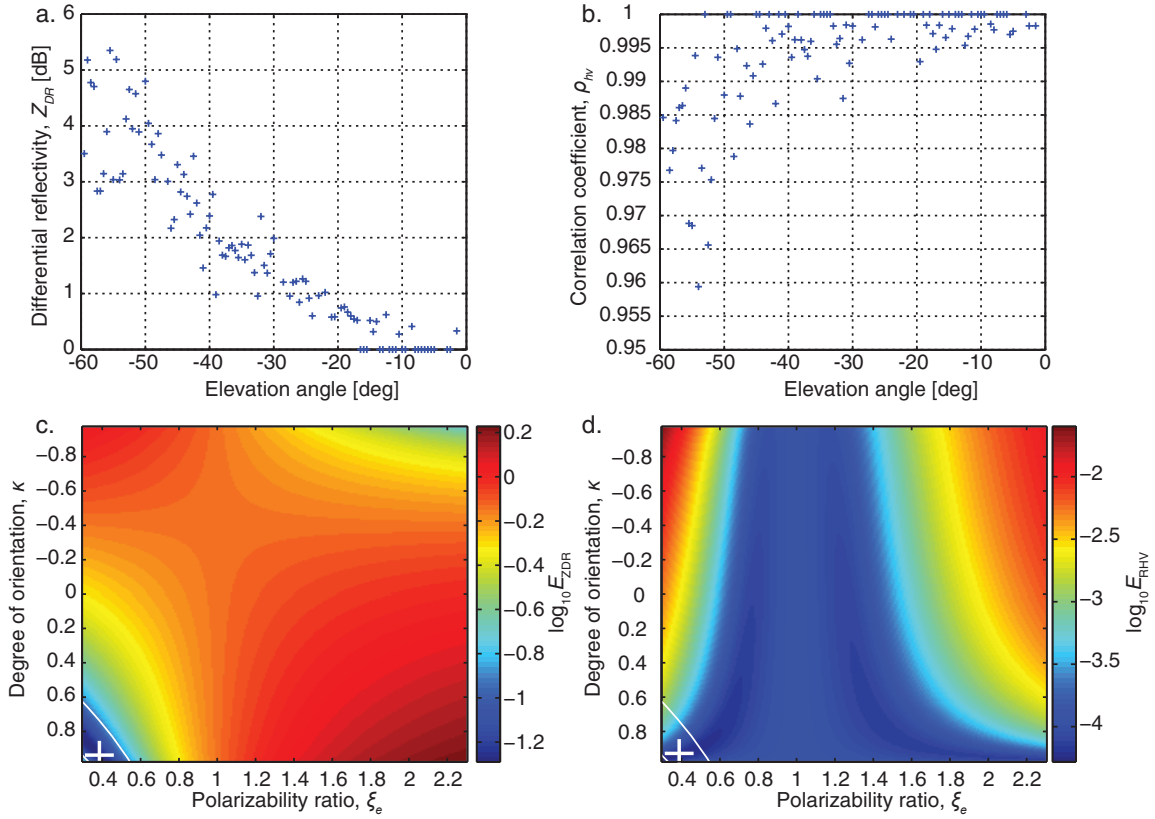


**Figure 5.11:** Measured elevation dependencies of differential reflectivity (a) and correlation coefficient (b) and logarithms of  $E_{ZDR}$  (c) and  $E_{RHV}$  (d). Measured data correspond to 4.7 km height of the left half-scan of Fig. 5.9. White contours indicate areas with  $E_{ZDR}(\kappa, \xi_e)$  not exceeding the minimum  $E_{ZDR}$  by a factor of 1.1. White crosses mark the results of the optimization algorithm. According to the classification scheme described in the text, this case corresponds to a polarizability ratio of 0.4 (oblate spheroids).

within these layers caused different types of ice crystals. At about 2 km height thin low-level cloud layers appeared from 13:00 to 17:00 UTC. These cloud layers had not enough SNR and/or were spatially inhomogeneous and, therefore, were filtered out by the retrieval algorithm.

In Figs. 5.12b and c mean and standard deviation of the polarizability ratio are presented, respectively. Every vertical profile was calculated from a half elevation scan. Thus, during a scan cycle (see Fig. 5.8) four consecutive profiles which correspond to different azimuth directions were derived. It can be seen that the high-level clouds (above 5 km height) are characterized by a polarizability ratio of  $0.85 \pm 0.07$ . According to Fig. 5.4 this can be caused either by ice particles of quasi-spherical shape or of low density or both. Low density ( $< 0.1 \text{ g cm}^{-3}$ ) of ice particles in cirrus clouds was reported, e.g., by *Heymsfield et al.* [2002]. Ice particles in the mid-level cloud with the top below 5 km height showed

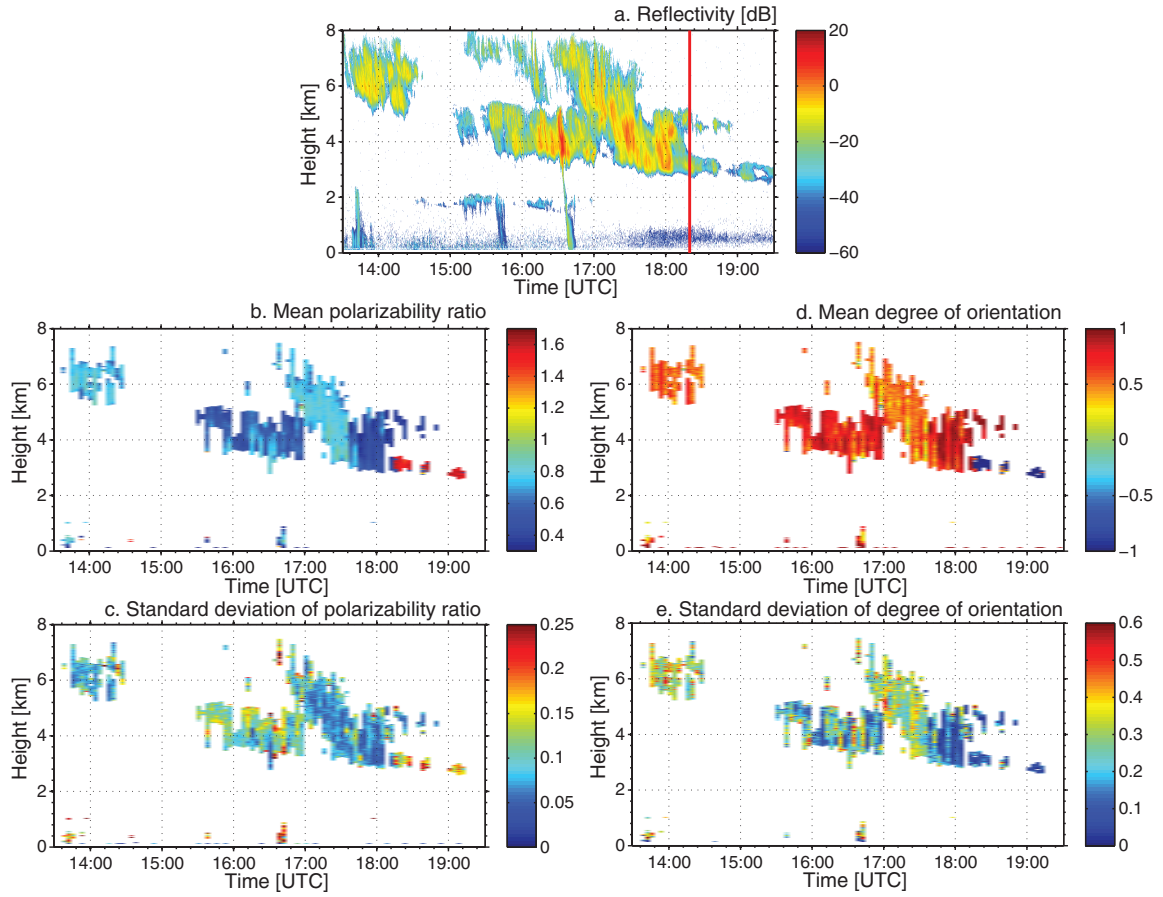


**Figure 5.12:** Height-time cross sections of (a) equivalent radar reflectivity factor  $Z_h$ , mean (b) and standard deviation (c) of polarizability ratio  $\xi_e$ , mean (d) and standard deviation (e) of degree of orientation  $\kappa$  taken at Cabauw, the Netherlands, on 20 October 2014. The equivalent radar reflectivity factor  $Z_h$  was measured with a collocated vertically pointed 35-GHz cloud radar MIRA-35 operated in LDR mode and with 1 s averaging. The vertical red line marks the time period which corresponds to Fig. 5.9.

values of  $\xi_e \approx 0.43 \pm 0.17$ , which indicates a strongly oblate shape and a high density of ice particles (Fig. 5.4). From 15:50 to 16:30 UTC the polarizability ratio increased to values of  $\xi_e \approx 0.83 \pm 0.1$  towards the bottom of the cloud. These signatures were accompanied by an enhancement of the effective radar reflectivity factor (Fig. 5.12a). Thus, the larger particles were more spherical and/or less dense which, is a clear indication of particle growth due to aggregation and/or riming processes. The capability to identify such processes can be especially useful for the investigation of precipitation formation. It can be seen from the virga shown in Fig. 5.12a, which partly reaches the ground, that the areas in which aggregation or riming occur can produce precipitation. From 18:15 to 19:15 UTC a thin cloud layer

with prolate ice particles was observed at 3 km height. These particles are characterized by  $\xi_e \approx 1.5 \pm 0.2$  (see also Fig. 5.10).

In Figs. 5.12d and e the mean and standard deviation of the degree of orientation are shown, respectively. Areas, where the spheroid shape of the ice particles was classified as strongly oblate or prolate, are characterized by  $\kappa$  values of  $\sim 0.7$  and  $\sim -0.95$ , respectively, i.e., particles are oriented nearly horizontally, which is consistent with theoretical studies [Sassen, 1980; Mitchell, 1996; Noel and Sassen, 2005]. The low standard deviation of  $\kappa$  in these areas indicates similar orientation distributions for ice particles observed at  $30^\circ \leq |\psi| \leq 60^\circ$ . Observed high-level clouds and cloud areas with seeding had considerably lower values of the degree of orientation with  $\kappa \sim 0.4 - 0.6$ . These values are indicative of a more random orientation of ice particles (around the horizontal alignment). The high standard deviation of  $\kappa$  in these clouds shows that ice particles observed at  $30^\circ \leq |\psi| \leq 60^\circ$  have significantly different orientation distributions.

---

## Chapter 6

# Shape-temperature relationship of pristine ice crystals

In the previous chapter the algorithm for a quantitative characterization of shapes and orientations of ice particles based on polarimetric observations with a newly developed 35-GHz cloud radar with hybrid polarimetric configuration was presented. The algorithm was applied to a complex cloud system observed during the ACCEPT field campaign in Cabauw, the Netherlands. During the ACCEPT campaign the performance of the hybrid-mode cloud radar was evaluated and a long-term dataset of six weeks was acquired. Such a dataset provides great potential for the statistical characterization of ice crystal habits under ambient conditions. This chapter aims at the characterization of the shape of preferably pristine ice crystals formed in mixed-phase clouds. Due to the lack of in situ observations, the retrieval could not be evaluated against direct observations of particle shapes. Nevertheless, an approach is presented that allows for an indirect validation of the polarimetric observations using microphysical properties of ice crystals grown in a wind tunnel under laboratory conditions. This chapter is based on *Myagkov et al.* [2016b] and is organized as follows. Section 6.1 describes the instruments used for this study and the data set. Five case studies are discussed in details in Sec. 6.2. The results of the analysis of 22 measurement cases and their comparison with laboratory studies are presented in Sec. 6.3. In Sec. 6.4 the retrieved degrees of orientation are shown.

### 6.1 Instrumentation and data set

The ACCEPT measurement campaign was initiated by the Leibniz Institute for Tropospheric Research (TROPOS), Leipzig, Germany, the Technical University of Delft, the Netherlands, and METEK GmbH, Elmshorn, Germany within the ITaRS (Initial Training for atmospheric Remote Sensing) project. The major goal of the campaign was to evaluate the capabilities

---



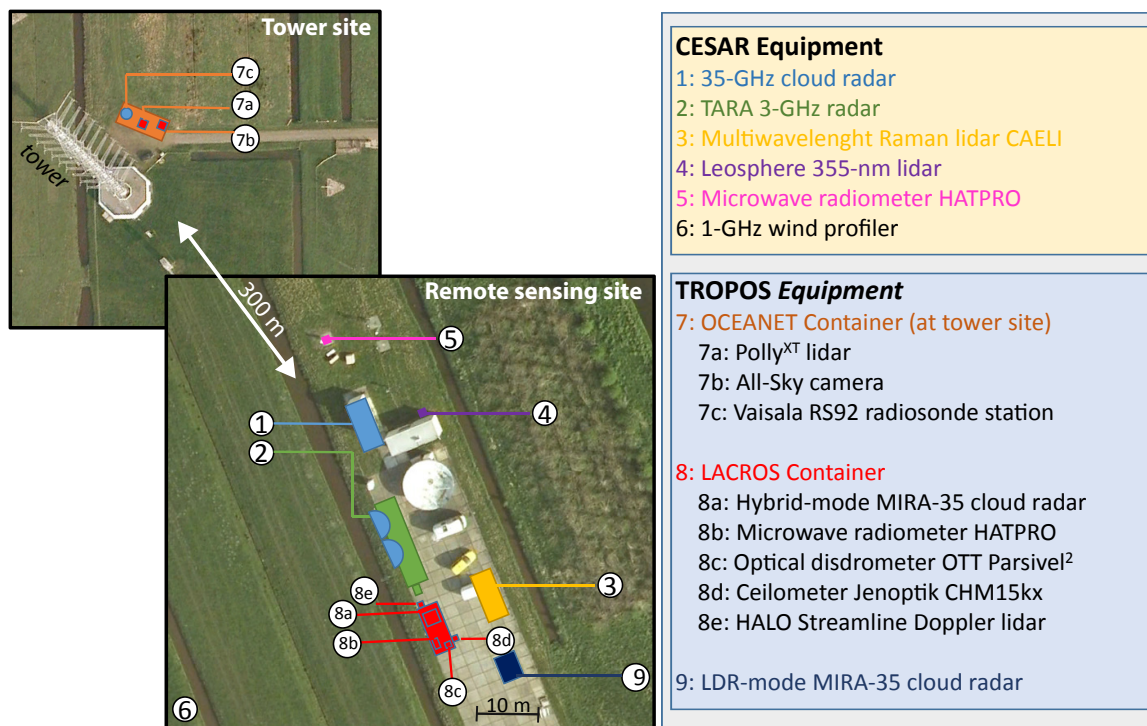


**Figure 6.1:** Instruments at the CESAR observatory during the ACCEPT campaign. The figure was provided by Dr. Patric Seifert.

of the newly developed hybrid-mode polarimetric cloud radar of type MIRA-35 described in Chapter 4 and to estimate the potential of its implementation into existing observational stations. In the following, this radar is denoted as the hybrid-mode MIRA-35.

The campaign took place at CESAR, located in the Netherlands ( $51.971^\circ$  N,  $4.927^\circ$  E), from 7 October to 17 November 2014. The CESAR observatory operated by the Royal Netherlands Meteorological Institute (KNMI) is well equipped with a variety of atmospheric remote-sensing instruments. In addition to the instruments available at CESAR and the hybrid-mode MIRA-35, which was rented from METEK GmbH, the main instruments of LACROS were brought to Cabauw. The instruments operated during the ACCEPT campaign are shown in Fig. 6.1. In Table 6.1 the equipment that was used for this particular study is listed.

As mentioned in Chapter 5, the shape retrieval requires information about elevation dependencies of the differential reflectivity  $Z_{DR}$  and correlation coefficient  $\rho_{hv}$ . Therefore, the hybrid-mode MIRA-35 was installed into the scanning unit of the LACROS container. An implemented scan cycle is shown in Fig. 5.8. During every scan cycle the radar was pointed vertically for several minutes. In this way, occasional rain events could be used for the calibration of polarimetric variables as explained in Chapter 4.

During the campaign a second cloud radar MIRA-35 was operated as well. The radar



**Table 6.1:** Instruments used in the ACCEPT campaign

Instrument	Main specifications	Measurements	Reference
Cloud radar MIRA-35	Frequency: 35.5 GHz, configuration: LDR, pointing: zenith, temporal resolution: 1 s, range resolution: 30 m	Equivalent radar reflectivity factor, LDR, mean Doppler velocity, Doppler width, complete spectra	<i>Görsdorf et al. [2015]</i>
Cloud radar MIRA-35	Frequency: 35.17 GHz, configuration: hybrid, pointing: scanning, temporal resolution: 1 s, range resolution: 30 m	Equivalent radar reflectivity factor, mean Doppler velocity, Doppler width, complete spectra, differential reflectivity, correlation coefficient, differential phase shift	<i>Myagkov et al. [2016a]</i>
Multiwavelength Raman lidar Polly <sup>XT</sup>	Wavelengths: 355 nm, 532 nm, 1064 nm, pointing: 5° off-zenith, temporal resolution: 30 s, range resolution: 7.5 m	Backscatter coefficient at three wavelengths, volume depolarization ratio at 532 nm	<i>Althausen et al. [2009]</i>
Microwave radiometer HATPRO	Bands: 22–31 GHz, 51–58 GHz, temporal resolution: 1 s	Brightness temperatures, temperature profile, liquid water path	<i>Rose et al. [2005]</i>
Radiosonde Vaisala RS92	Variable resolution	Temperature, pressure, relative humidity, wind	<i>Suortti et al. [2008]</i>

is owned by TROPOS and has the conventional linear depolarization configuration. In the following, this radar is denoted as LDR-mode MIRA-35. The radar was unmounted from the scanning unit of the LACROS container and installed into a trailer without scanning unit and, thus, was pointed vertically. In order to avoid interference between the two cloud radars, their operation frequencies were set to differ by approximately 330 MHz (35.17 GHz vs 35.5 GHz for hybrid-mode and LDR-mode MIRA-35, respectively). Additionally, the trailer was placed about 30 m away from the LACROS container to avoid any near-field interference. In this study, data from LDR-mode MIRA-35 are used to estimate the temporal and spatial dimensions of the observed cloud systems.

When both liquid water droplets and ice crystals are present in a volume, cloud radar alone can hardly detect the liquid-water signatures. It is, however, well known that polarimetric lidars are powerful tools for the detection of supercooled liquid particles within mixed-phase clouds [*Schotland et al., 1971; Seifert et al., 2010*]. The multiwavelength Raman lidar Polly<sup>XT</sup> was employed for this purpose. The lidar was set up near the Cabauw meteorological tower, which is located about 300 m north of the measurement site where most of

the other instruments were operated. In order to avoid specular reflection from horizontally aligned planar surfaces of ice crystals the laser beam of Polly<sup>XT</sup> was pointed to 5° off-zenith. The container with the lidar was oriented in such a way that the beam was above the radar site at about 4 km height.

Temperature is the main parameter controlling the efficiency of heterogeneous nucleation of ice crystals [DeMott *et al.*, 2015] and it is lowest at cloud top. Therefore, in this study cloud-top temperature is used as the reference parameter when crystal properties are investigated. In order to retrieve the temperature at the cloud tops, the used techniques are, in order of priority, either locally launched radiosondes, the microwave radiometer HATPRO, or assimilated meteorological datasets. Radiosondes of type Vaisala RS-92 were occasionally launched on-site. If no local radiosonde information was available, radiosonde data from the 00 UTC launch at De Bilt (WMO code: 06260; 20 km northeast of CESAR site) was used in case the cloud was observed around 00 UTC. If no recent radiosonde ascent was available, temperature data of HATPRO was used in non-precipitating conditions. Finally, for precipitating cases, when the operation of the microwave radiometer is hampered, temperature profiles from the GDAS1 dataset (available at: <http://ready.arl.noaa.gov/gdas1.php>) provided by the Global Data Assimilation System (GDAS, Kanamitsu [1989]) operated by the U.S. National Center for Environmental Prediction (NCEP) were used.

For the analysis 22 cases of mid-level mixed-phase clouds with the following criteria were manually chosen:

1. The hybrid-mode MIRA-35 was operating and the measured signal-to-noise ratio was high enough to retrieve calibrated polarimetric variables according to Chapter 4.
  2. The investigated cloud layer did not experience seeding from upper clouds. Seeding would hamper the relation of crystal properties to a definite cloud-top temperature.
  3. The calibrated polarimetric variables were available for more than 50 % of the data points in elevation dimension within a half-scan of the hybrid-mode MIRA-35. This is a basic criterion for the horizontal homogeneity of the analyzed cloud layer. However, the cloud spatial homogeneity is not a major assumption of the retrieval algorithm. Instead, it is assumed that ice particles present at the same altitude (same ambient conditions) have the same shape, even if the cloud is not spatially homogeneous [Myagkov *et al.*, 2016a].
  4. Cloud-top temperatures were in the range from about  $-20^{\circ}\text{C}$  to  $-0^{\circ}\text{C}$ . Ice crystals formed at such temperatures under water saturation conditions have a clear primary shape [Bailey and Hallett, 2009]. At lower temperatures ice particles can have a variety of shapes at a certain temperature caused by differences in the ice supersaturation [Bailey and Hallett, 2004], which can significantly influence the shape retrieval.
-

5. For non-precipitating cases lidar data should be available for the identification of liquid layers.
6. At temperatures above  $-5^{\circ}\text{C}$  the presence of ice crystals should be confirmed. For cases without liquid precipitation, ice virgae produce strong volume depolarization ( $> 0.2$ ) of the lidar signal. For precipitating cases, a melting layer is an indicator of ice presence. If none of the two checks was positive, the layer was excluded from further analysis.

In the ideal case, analyzed cloud layers should not produce liquid precipitation to permit the usage of lidar and radiometer data. Nevertheless, most of the clouds with cloud-top temperatures warmer than  $-5^{\circ}\text{C}$  that fulfilled the requirements 1–4 produced precipitation.

## 6.2 Examples of the shape retrieval

In this section five examples of the shape estimation retrieval based on elevation scans of differential reflectivity and correlation coefficient are shown. Mixed-phase clouds with different cloud-top temperatures observed during the ACCEPT campaign were chosen. Several types of ice crystals were clearly identified by the hybrid-mode MIRA-35. The fifth case study indicates that slight variations of cloud-top altitude can lead to changes from oblate to prolate shape.

### 6.2.1 Case 1: 12 October 2014, 15:00–16:00 UTC

Figures 6.2a and b show height-time cross sections of the equivalent radar reflectivity  $Z_h$  and LDR measured by LDR-mode MIRA-35. These parameters were calculated using the total powers of the received signals in the co- and cross-polarized channels. A cloud system observed on 12 October 2014, 15:00–16:00 UTC, is depicted. The radar observed a cloud layer with the top at around 5.2 km height. After 15:32 UTC the cloud layer was influenced by a higher-level cloud with a top height at 6 km height. Thus, for the analysis the time period 15:16–15:20 UTC, when the high-level cloud did not cause any seeding effects to the lower layer, was chosen. Within the chosen period the SNR was high enough to apply the shape retrieval algorithm. On the other hand, ice development in this period was not as intensive as the one starting at 15:20 UTC, which is confirmed by about 10 dB lower values of  $Z_h$  (see Fig. 6.2a). Figure 6.2b shows that in the cloud layer ice particles did not produce depolarization. Observed values of LDR are very close to the minimum observable LDR of  $-31$  dB. In Fig. 6.2c and d the attenuated backscatter coefficient and the volume linear depolarization ratio measured by Polly<sup>XT</sup> are presented, respectively. A single liquid layer indicated by increased values of the backscatter coefficient can be clearly seen at the top of the cloud layer. Low values of volume depolarization ratio within the liquid layer are caused

---

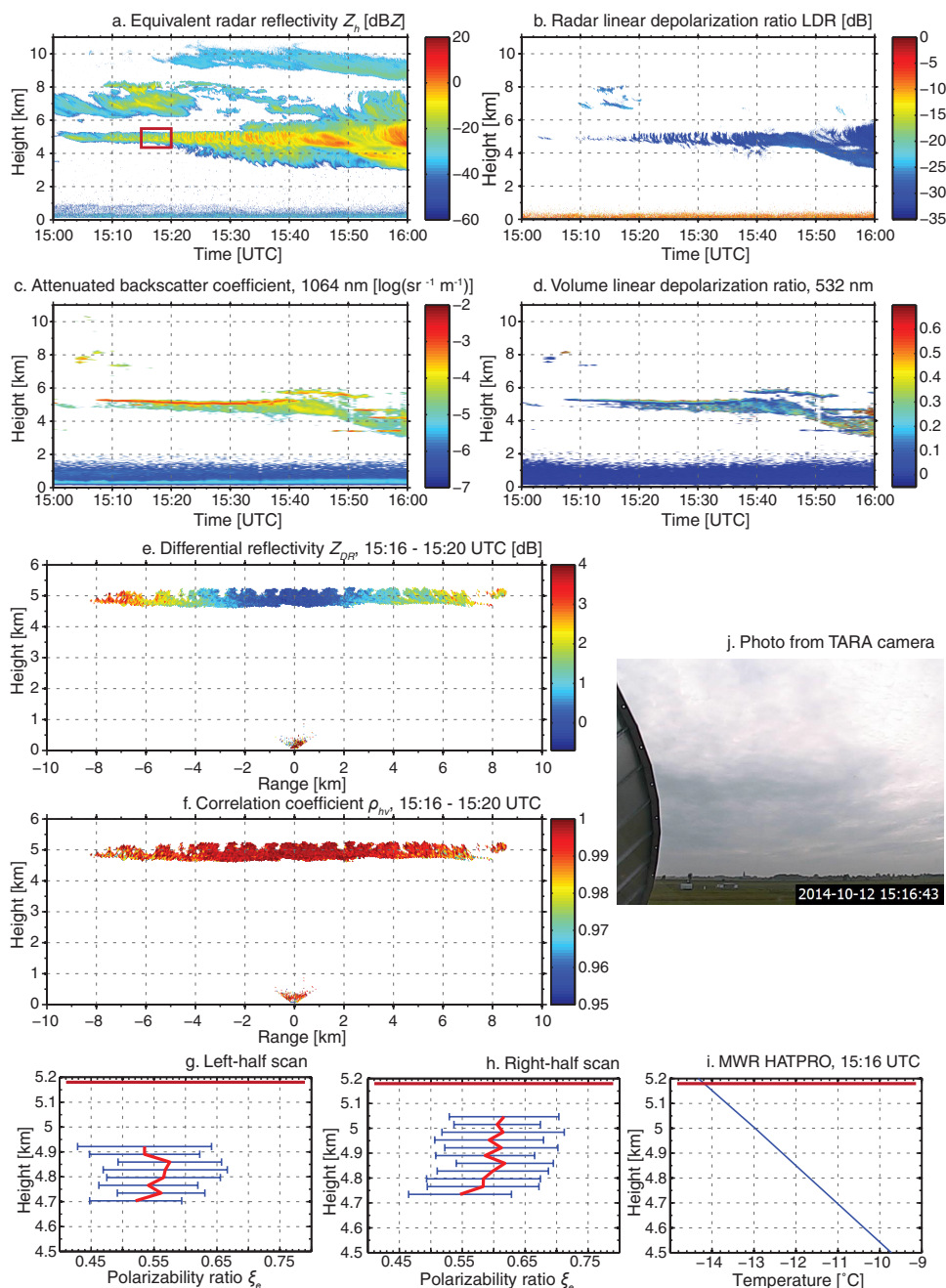


**Figure 6.2:** Case study of 12 October 2014, 15:00–16:00 UTC. (a) Radar reflectivity  $Z_h$  and (b) radar linear depolarization ratio from LDR-mode MIRA-35, (c) attenuated backscatter coefficient and (d) volume linear depolarization ratio at 532 nm from Polly<sup>XT</sup>, (e) differential reflectivity  $Z_{DR}$  and (f) correlation coefficient  $\rho_{hv}$  measured by hybrid-mode MIRA-35. Vertical profiles of polarizability ratio for the left- (g) and right-half scans (h), respectively. (i) Vertical temperature profile from the microwave radiometer HATPRO. (j) Photo taken by a web camera. The red rectangle shows the analyzed cloud layer and the time period corresponding to a full elevation scan of hybrid MIRA-35. Red horizontal lines in (h,i,j) represent the cloud top.

by the spherical shape of supercooled water drops. It is noticeable that values of volume depolarization ratio were also low in the ice virga. The reason for this behavior is unclear, considering that Polly<sup>XT</sup> is pointed 5° off-zenith to prevent the influence of specular reflection at planar planes of horizontally aligned crystals. It may thus be a distinct microphysical feature of the ice crystals formed at the given temperature.

A photograph of the analyzed cloud layer is shown in Fig. 6.2g. It can be seen that the cloud is relatively homogeneous. Figures 6.2e and f depict the differential reflectivity  $Z_{DR}$  and the correlation coefficient  $\rho_{hv}$  measured by the hybrid-mode MIRA-35, which were calculated for the spectrum peaks. The elevation scans of  $Z_{DR}$  and  $\rho_{hv}$  are uncorrected for the polarization coupling to make the figures more illustrative. After the correction the amount of data points is much lower. Nevertheless, for the shape retrieval shown below the corrected values were used. Strong elevation dependencies can be seen in  $Z_{DR}$  and  $\rho_{hv}$ . At 0° elevation, the differential reflectivity is almost zero, whereas it reaches values of 3 dB at 60° elevation. The correlation coefficient has values close to 1 in zenith direction, while its values at 60° reach 0.98.

Using the corrected values of  $Z_{DR}$  and  $\rho_{hv}$  polarizability ratios were retrieved separately for the left- and right-half scans. For the antenna coupling correction vertical measurements in rain on 12 October 2014, 19:00–20:00 UTC were used. Results of the retrievals are given in Figs. 6.2h and i. Vertical profiles indicated by red line correspond to mean values of the polarizability ratio. Horizontal blue bars denote 2 standard deviations of the polarizability ratio. The value of the polarizability ratio close to the cloud top is of special interest, because there ice particles should be least influenced by processes such as aggregation and riming, which would lead to a deviation of the crystal shape from its pristine state. Unfortunately, often the SNR at the cloud top is too low to apply the retrieval. The retrieved value of the polarizability ratio closest to the cloud top is  $0.62 \pm 0.09$ , which corresponds to oblate spheroids. The distance from the cloud top is about 150 m. Figure 6.2j represents a temperature profile retrieved from the microwave radiometer HATPRO. It can be seen that at the cloud top, where ice crystals are formed, the temperature was  $-14.2^\circ\text{C}$ .

### 6.2.2 Case 2: 18 October 2014, 01:00–02:00 UTC

An analysis of a mid-level mixed-phase cloud observed on 18 October 2014, 01:00–02:00 UTC, is given in Fig. 6.3. The time period chosen for the retrieval is 01:23–01:27 UTC. The cloud top estimated from equivalent radar reflectivity measured by LDR-mode MIRA-35 (Fig. 6.3a) was at about 5 km height. The thickness of the cloud layer exceeded 1.2 km. The radar reflectivity reached values as high as 10 dBZ, which indicate the presence of large ice particles. LDR values registered by LDR-mode MIRA-35 for the analyzed period were mostly low, even though areas with increased LDR (up to  $-17$  dB) can be seen occasionally at 4.0–4.5 km height. At the top of the cloud a liquid layer characterized by high attenuated backscatter

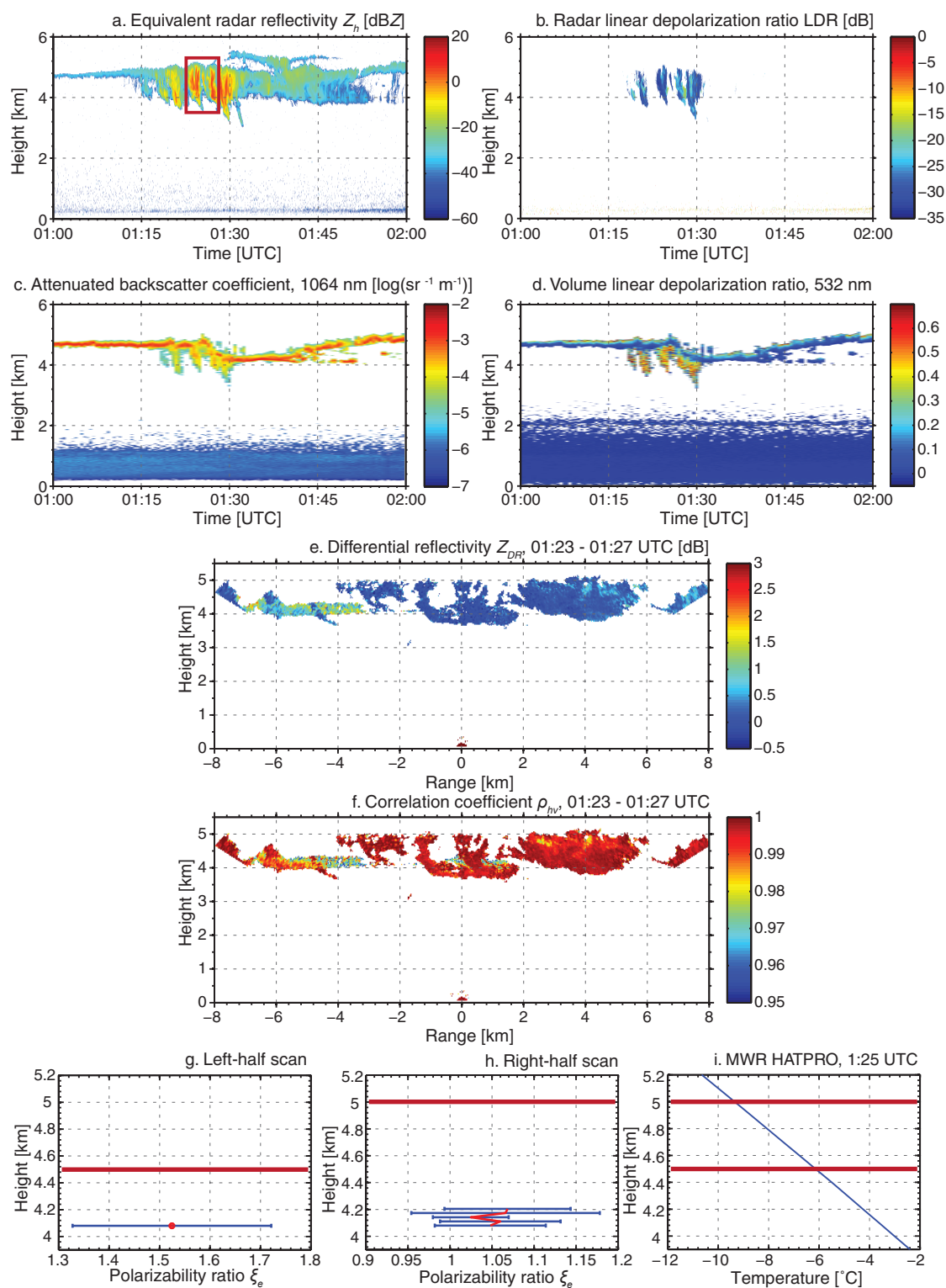


**Figure 6.3:** Same as Fig. 6.2, but for 18 October 2014, 01:00–02:00 UTC, and without a photograph.

coefficients and low volume depolarization ratios (Figs. 6.3c and d, respectively) is visible. It should be noted that in the second half of the analyzed period (01:27 UTC) the lidar also detected an internal liquid layer at 4.5 km height. In contrast to case 1, where low volume depolarization ratios were observed with Polly<sup>XT</sup>, the ice virgae observed in the case 2 produced volume depolarization ratios exceeding 0.5.

Elevation scans of the differential reflectivity and the correlation coefficient depicted in Figs. 6.3e and f, respectively, show that the cloud was spatially inhomogeneous. Within the right-half scan only slight angular changes in  $Z_{DR}$  and  $\rho_{hv}$  are visible. In the left-half scan high  $Z_{DR}$  and low  $\rho_{hv}$  values were observed at lower elevations at 4.0–4.5 km height, where the lidar detected the internal liquid layer. For the correction of the polarization coupling vertical measurements in a short precipitation event on 18 October 2014, 2:30–2:50 UTC, were used. The results of the shape retrieval are shown in Figs. 6.3g and h. It can be seen that due to the spatial inhomogeneity the calculated polarizability ratios are available only for a limited number of range bins. Nevertheless, the results show that in the left-half scan prolate particles characterized by the polarizability ratio of  $1.5 \pm 0.2$  were detected. In the right-half scan the polarizability ratios closest to the cloud top were  $1.1 \pm 0.1$ . Such values correspond to particles with quasi-spherical shapes and/or low apparent ice density (see Fig. 5.4). Below, such particles are denoted as quasi-isotropic as they do not change the polarization of the scattered wave significantly. The distances from the liquid layers, where prolate and quasi-isotropic particles formed, were about 0.4 and 0.8 km, respectively. Figure 6.3i shows that temperatures at liquid-layer heights were about  $-6$  °C and  $-9$  °C, respectively. We point out that the coexistence of different types of particles can lead to a misclassification of prolate and oblate particles. The spectrum peaks at different elevations can be dominated by different particles. One of the ways to avoid this influence is a combined Doppler–polarimetric analysis similar to the one given by *Oue et al.* [2015]. After the separation of spectral modes the retrieval algorithm can be applied to each mode separately. In this thesis such analysis is not provided.

### 6.2.3 Case 3: 20 October 2014, 18:00–19:00 UTC

In Fig. 6.4 a residual part of a mixed-phase cloud system observed on 20 October 2014, 18:00–19:00 UTC, is shown. A cloud layer with the cloud top at around 3.6 km height in the time period of 18:16–18:20 UTC (Fig. 6.4a) is considered. In the chosen area the cloud layer was about 1 km thick and the radar reflectivity reached  $-10$  dBZ. The cloud layer did not experience seeding from the higher cloud layer. High values of LDR (Fig. 6.4b) that reached up to  $-15$  dB indicated the presence of strongly non-spherical scatterers. In Figs. 6.4c and d enhanced values of the attenuated backscatter coefficient and low volume depolarization ratios at the top of the cloud layer indicated the presence of a single supercooled liquid layer. The average volume depolarization ratio in the ice virga was  $\sim 0.3$ .

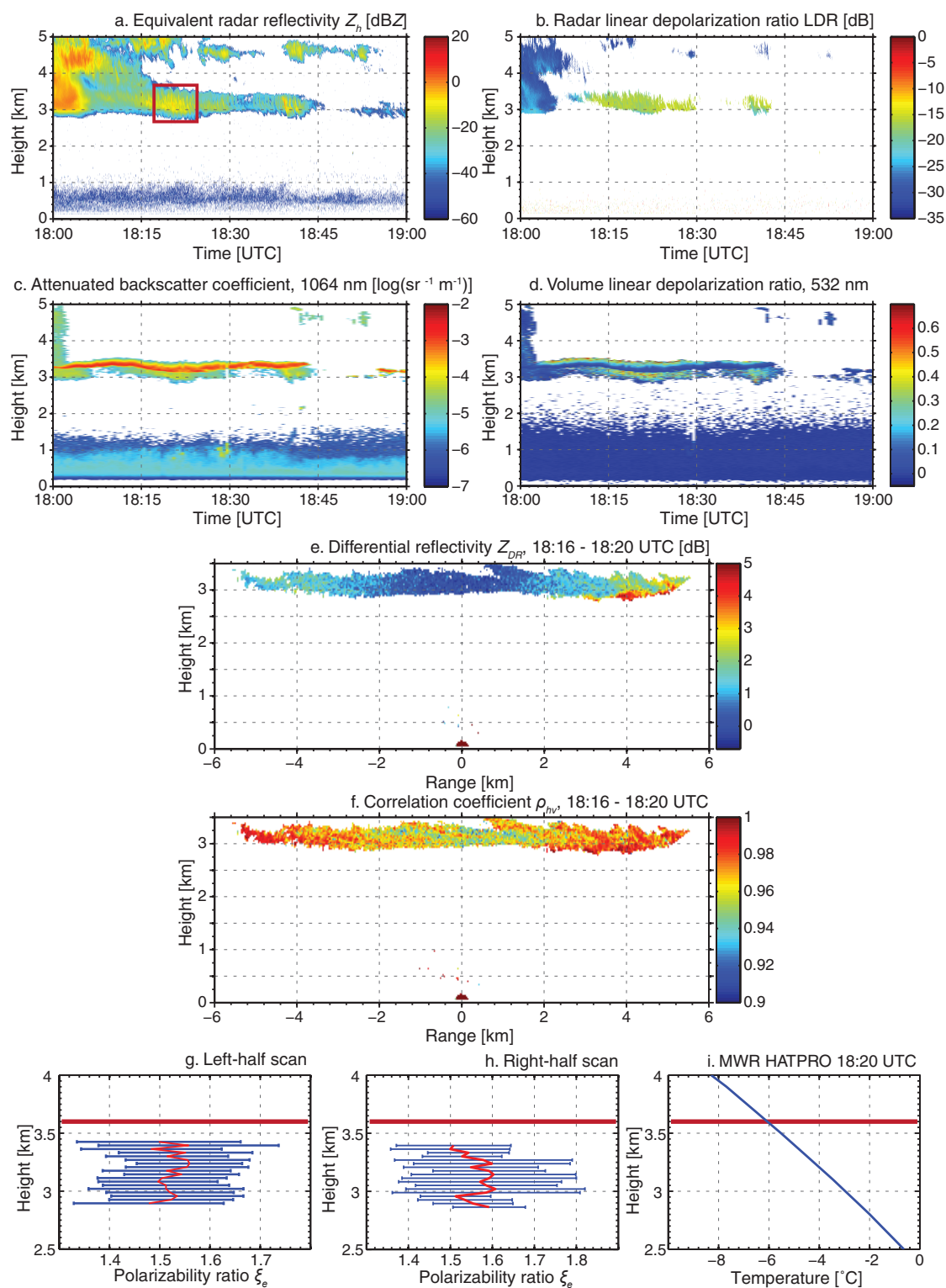


**Figure 6.4:** Same as Fig. 6.2, but for 20 October 2014, 18:00–19:00 UTC, and without a photograph.



Figures 6.4e and f show that the cloud layer was spatially homogeneous. Strong angular dependencies in  $Z_{DR}$  and  $\rho_{hv}$  can be clearly seen. Changes in differential reflectivity were up to 2 dB and 4 dB within the left- and right-half scan, respectively. The correlation coefficient  $\rho_{hv}$  had its minimum in zenith-pointing direction and approached higher values at lower elevations. It was shown in Chapter 5 that such signatures are specific for prolate particles. For the correction of the polarization coupling vertical observations in light rain on 21 October 2014, 8:00 – 9:00 UTC, were used. The results of the shape retrieval are depicted in Figs. 6.4g and h. Retrieved polarizability ratios are slightly higher in the right-half scan, which is caused by the observed increased values of  $Z_{DR}$ . The polarizability ratios closest to the cloud top are  $1.5 \pm 0.2$ . The distance from the cloud top is about 240 m. A temperature profile retrieved from the microwave radiometer HATPRO indicated that the temperature at the cloud top was about  $-6^\circ\text{C}$  (see Fig. 6.4i).

#### 6.2.4 Case 4: 10 November 2014, 02:00–03:00 UTC

A complex mixed-phase cloud system observed on 10 November 2014, 02:00–03:00 UTC, is presented in Fig. 6.5. A cloud layer with the cloud top at around 5 km height in the time period 02:53–02:57 UTC is considered for the analysis. The cloud layer was more than 2 km thick. The equivalent radar reflectivity at the cloud top did not exceed  $-10$  dBZ, while it reached values up to 10 dBZ towards the cloud bottom (Fig. 6.5a). LDR values measured by LDR-mode MIRA-35 were about  $-30$  dB (Fig. 6.5b). In Fig. 6.5c it can be seen that the laser beam often could not penetrate through the whole cloud layer because of strong attenuation. Nevertheless, some indications of liquid water at the cloud top are present. For example, two areas at 5.4 km height characterized by low volume depolarization ratio can be identified. There is also a thick internal liquid layer at about 4 km height specified by the increased attenuated backscatter coefficient and the low volume depolarization ratio.

Figures 6.5e and f show almost no angular dependencies of  $Z_{DR}$  and  $\rho_{hv}$ . Some slight changes are visible at 4 km height where the lidar detected the internal liquid layer. For the correction of the antenna coupling a short precipitation event on 1 November 2014, 17:00–18:00 UTC, was used because the correction parameters were found to be almost constant in November 2014. The retrieved polarizability ratios were close to 1 characterizing quasi-isotropic particles. The profiles indicate rapid changes of the polarizability ratio from 0.92 to 1.05, e.g., from 4.5 to 4.8 km height in the left-half scan. Such changes result from misclassification of prolate and oblate particles which is caused by the variability in  $Z_{DR}$  and  $\rho_{hv}$  due to measurement noise and/or differences in scattering properties of ice populations. Biases in polarimetric variables caused by the polarization coupling also lead to inaccurate classification. Without the polarization coupling correction given by [Myagkov *et al.*, 2016a] the misclassification for the used radar would result in a range of polarizability ratios from 0.8 to 1.2. For the following analysis, the polarizability ratio of  $0.92 \pm 0.08$  observed 450 m below

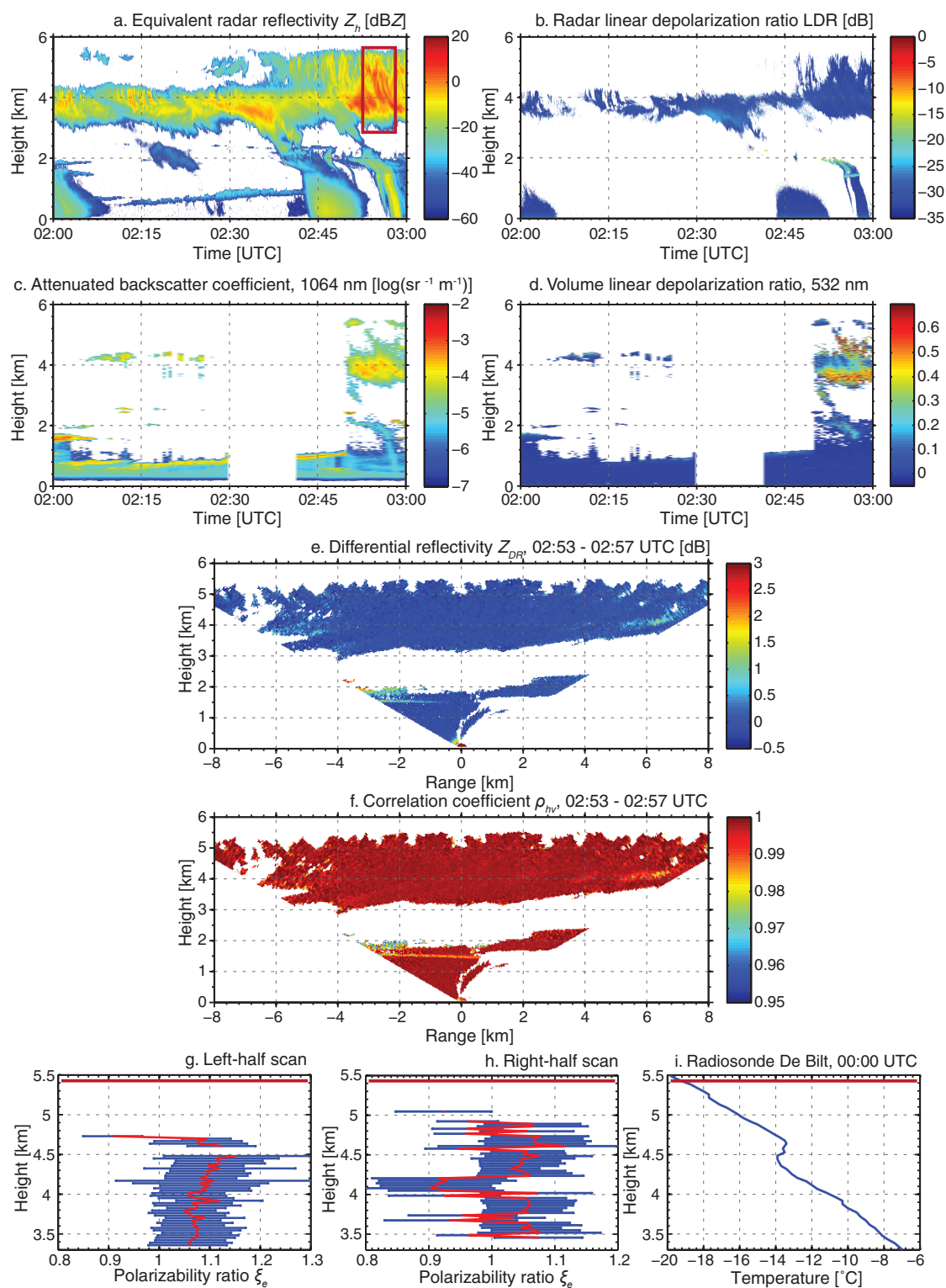


**Figure 6.5:** Same as Fig. 6.2, but for 10 November 2014, 02:00–03:00 UTC, and without a photograph.

the cloud top was chosen. The temperature measured at 5.5 km height by the radiosonde launched at midnight from De Bilt was about  $-20^{\circ}\text{C}$  (see Fig. 6.5i).

### 6.2.5 Case 5: 7 November 2014, 20:00–21:00 UTC

Figure 6.6 depicts a precipitating cloud system with the cloud top located at around 2.3 km height, which was observed on 7 November 2014, 20:00–21:00 UTC. The SNR in this case was not high enough to retrieve polarizability ratios, although elevation dependencies of the measured polarimetric variables allow us to classify the general shape of the observed ice particles. Two full scans performed by the hybrid-mode MIRA-35, which correspond to time periods shown in Fig. 6.6a enframed by black rectangles, were analyzed. The time gap between these periods is 11 min. It can be seen that values of  $Z_h$  in the first period do not exceed  $-15$  dBZ. Ice formation was not intensive enough to produce precipitation reaching the ground. Corresponding ice particles caused low depolarization, which is indicated by low LDR values of around  $-30$  dB shown in Fig. 6.6b. In contrast, ice formation during the second time period was much more intensive.  $Z_h$  values close to the top of the cloud were around  $-20$  dBZ, while those observed 1 km below the cloud top exceeded 10 dBZ. Ice particles were large enough to produce liquid precipitation at the ground with 10 dBZ equivalent radar reflectivity. Ice particles in the second period were characterized by LDR values of up to  $-15$  dB. The melting layer with LDR of  $-12$  dB is clearly seen at about 1.4 km height.

In Figs. 6.6c and d range-height cross sections of SNR for the first and second time period are given, respectively. In both cases, SNR is of the same order of magnitude. Elevation scans of differential reflectivity shown in Figs. 6.6e and f yield  $Z_{DR}$  values close to 0 dB in the zenith-pointing direction, while at lower elevations  $Z_{DR}$  reached 4 dB and 2 dB, respectively. For both cases,  $Z_{DR}$  had less pronounced angular dependence at 1.5 km height. This effect can be caused by aggregation as particles become more spherical and/or less dense. Angular dependencies of  $\rho_{hv}$  at the cloud tops show a different behavior. In Fig. 6.6g  $\rho_{hv}$  has the highest value in the zenith-pointing direction and slightly decreases at lower elevations. For the second time period  $\rho_{hv}$  has its minimum value of about 0.93 at vertical pointing direction and increases up to 0.98 at lower elevations. Observed elevation dependencies at the cloud tops indicate the presence of oblate and prolate particles for the first and the second time period, respectively. Unfortunately, continuous temperature profiles from the microwave radiometer were not available for this case because of precipitation. Temporal resolution of the GDAS1 model is three hours and can therefore not be used to capture temperature variations within 15 min. The temperature profile given in Fig. 6.6i shows a cloud-top temperature of  $-4^{\circ}\text{C}$  at 2.3 km height at 21:00 UTC. In Fig. 6.6a it can be seen that cloud-top altitudes for the analyzed time periods differ by about 200 m. Also vertical variations of LDR (Fig. 6.6b) indicate changes of the  $0^{\circ}\text{C}$  isotherm. Thus, temperatures at the top could

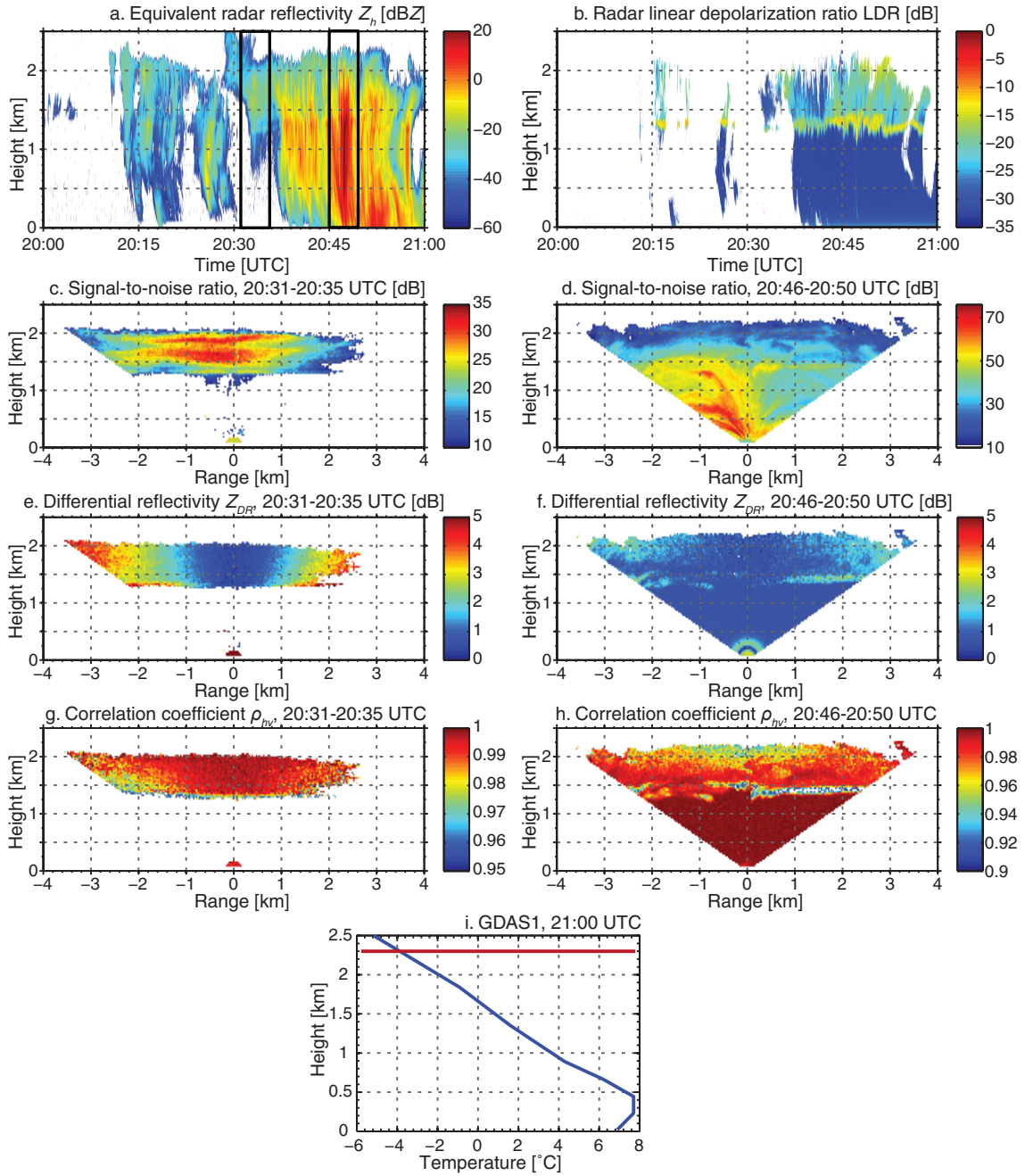


**Figure 6.6:** Case study of strong short-term variability of ice particle shapes observed at Cabauw, the Netherlands, on 7 November 2014, 20:00–21:00 UTC. (a) Radar reflectivity  $Z_h$  and (b) radar linear depolarization ratio from LDR-mode MIRA-35, (c) signal-to-noise ratio, (e) differential reflectivity  $Z_{DR}$  and (g) correlation coefficient  $\rho_{hv}$  measured by hybrid-mode MIRA-35 from 20:31 to 20:35 UTC, (d) signal-to-noise ratio, (f) differential reflectivity  $Z_{DR}$  and (h) correlation coefficient  $\rho_{hv}$  measured by hybrid-mode MIRA-35 from 20:46 to 20:50 UTC, (i) vertical temperature profile from the GDAS1 model. Two black rectangles in (a) show the analyzed cloud layer and the time periods corresponding to full elevation scans of hybrid-mode MIRA-35. The red horizontal line in (i) represents the cloud top at 20:45 UTC.

be different by few degrees, which can cause crucial differences in the ice particle shape. Such strong indications of the presence of oblate particles at such warm temperatures were observed twice during the whole field campaign. In both cases, the existence of these particles was registered for not longer than about 5 min.

### 6.3 Comparison of shape with laboratory studies

The analysis shown in Sec. 6.2 was applied to 22 cases. The number of cases corresponding to cloud-top-temperature ranges from  $-7$  to  $-3^\circ\text{C}$ ,  $-13$  to  $-7^\circ\text{C}$ ,  $-17$  to  $-13^\circ\text{C}$ , and  $-25$  to  $-17^\circ\text{C}$  are 9, 2, 9, and 2, respectively. Most of the analyzed clouds had a liquid layer at the top, which was identified using the polarimetric measurements from the lidar. In the case of precipitating clouds the conclusion of *Westbrook and Illingworth* [2011] that 95 % of ice crystals at temperatures warmer than  $-20^\circ\text{C}$  are formed in presence of liquid water is taken into account. For every case the polarizability ratio closest to the cloud top detected by the LDR-mode MIRA-35 was chosen. The distance from the cloud top mostly did not exceed 500 m.

For the comparison, measurements from fall chamber studies of *Takahashi et al.* [1991] were utilized. In order to facilitate the comparison, first the polarizability ratio needs to be derived from the laboratory measurements. Thus, the information about axis lengths and mass of ice particles grown at water saturation conditions in the temperature range from  $-23$  to  $-3^\circ\text{C}$  was used. The apparent ice density of an ice particle was defined as follows:

$$\rho_a = \frac{8m}{3\sqrt{3}a^2c}, \quad (6.1)$$

where  $m$  is the mass of the ice particle. According to *Takahashi and Fukuta* [1988] the apparent ice density in Eq. (6.1) is calculated considering the ice particle as a hexagonal prism.

The dependencies of the geometrical axis ratio and the apparent ice density on the temperature at which ice particles were formed are shown in Fig. 6.7. At temperatures as low as  $-5$  and  $-15^\circ\text{C}$  long columns (strongly prolate) and dendrites (strongly oblate particles) were formed in the laboratory, respectively. Quasi-spherical (also known as isometric) particles were observed near  $-3$ ,  $-10$ , and  $-23^\circ\text{C}$ . These shape-temperature dependencies have been known from laboratory measurements since the 1950s [*Kampe et al.*, 1951], even though it is not clear yet to which extent these studies are valid at ambient conditions. Considering the apparent ice density, it can be seen that the columns and the dendrites had values of  $\rho_a$  down to  $0.3\text{ g cm}^{-3}$ . At temperatures around  $-12$  and  $-16^\circ\text{C}$  particles had the highest values of  $\rho_a$  exceeding  $0.8\text{ g cm}^{-3}$ . Ice formation in this temperature range was studied more precisely by *Takahashi* [2014]. Quasi-spherical particles tended to have  $\rho_a$  in the range of  $0.6\text{--}0.8\text{ g cm}^{-3}$ .

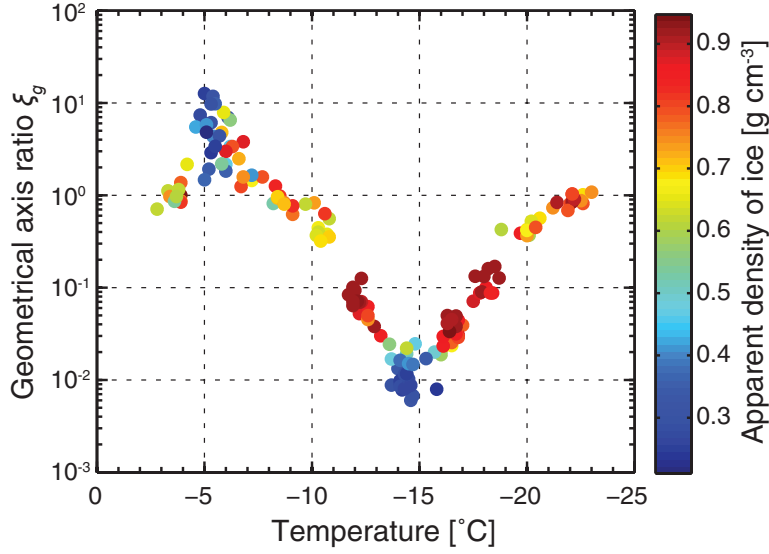


**Figure 6.7:** Temperature dependence of geometrical axis ratio for particles grown in a free-fall cloud chamber [Takahashi *et al.*, 1991]. Apparent density is color-coded. Note that  $\xi_g > 1$  corresponds to prolate particles,  $\xi_g < 1$  corresponds to oblate particles. Numerical data were provided by Prof. Takahashi, Hokkaido University of Education, Sapporo, Japan.

It is known that the dielectric constant of ice is almost linearly dependent on apparent ice density [Oguchi, 1983]. In this study the following dependence is assumed:

$$\epsilon_r = 2.36\rho_a + 1, \quad (6.2)$$

where  $\rho_a$  is in  $\text{g cm}^{-3}$ .

Based on the spheroidal scattering model and information about geometrical axis ratios and dielectric constants of ice crystals grown in a fall chamber, polarizability ratios  $\xi_e$  (see Eqs. (5.5)–(5.10)) were calculated. For the polarimetric scattering model it was assumed that spheroids have the same volume and the geometrical axis ratio as the hexagonal prisms used for the calculation of the apparent ice density in Eq. (6.1). In Fig. 6.8 values of  $\xi_e$  retrieved from the laboratory studies are shown as blue filled circles. The highest  $\xi_e$  values of about 1.6–1.7 were observed in the temperature range from  $-7$  to  $-6^\circ\text{C}$ . Even though prolate particles with the highest geometrical axis ratio were formed at  $-5^\circ\text{C}$ , they had low apparent ice density and therefore their  $\xi_e$  did not exceed 1.4. Polarizability ratios of 0.4 correspond to ice crystals that formed at temperatures of  $-12$  and  $-16^\circ\text{C}$ , where ice crystals were found to cause apparent ice densities exceeding  $0.8 \text{ g cm}^{-3}$ . Dendrites, which form at  $-15^\circ\text{C}$ , had low  $\rho_a$  that led to values of  $\xi_e$  of 0.6.

In Fig. 6.8 polarizability ratios retrieved from the polarimetric observations of the hybrid-mode MIRA-35 during the ACCEPT campaign are also shown (red filled dots with error bars). A good agreement between findings from the free-fall chamber and remote observations

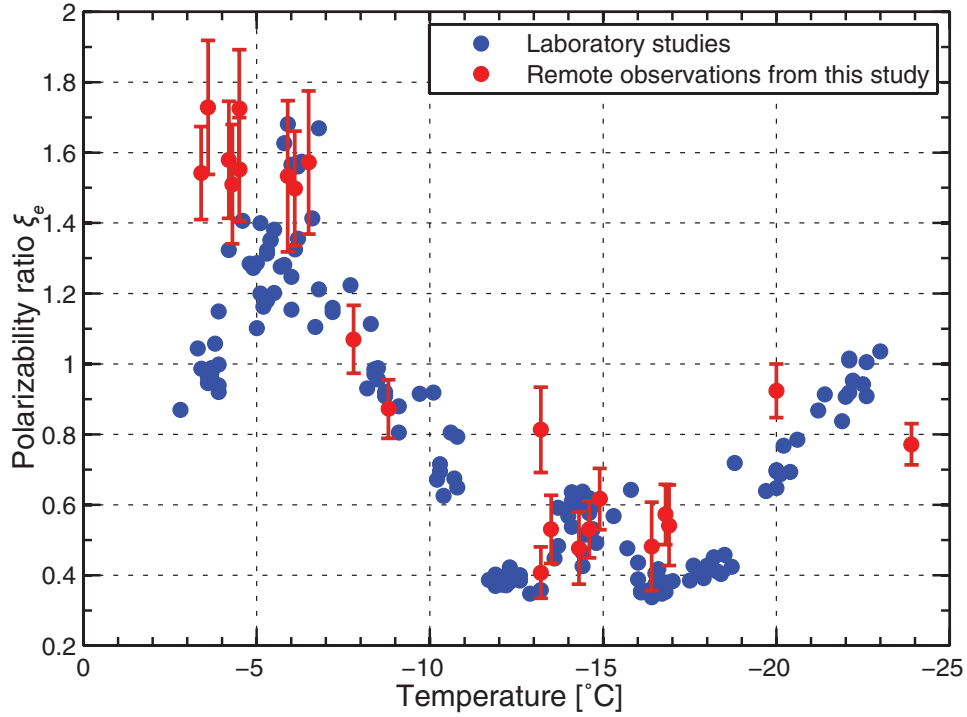


**Figure 6.8:** Temperature dependence of polarizability ratios for ice crystals grown in the free-fall chamber (blue filled circles) and for the ones located close to tops of mixed-phase clouds, retrieved from hybrid-mode MIRA-35 (red filled circles). Note that  $\xi_e > 1$  corresponds to prolate particles,  $\xi_e < 1$  corresponds to oblate particles. Vertical red bars represent  $\pm 1$  standard deviations of observed polarizability ratios. Data from the free-fall chamber [Takahashi *et al.*, 1991] were provided by Prof. Takahashi, Hokkaido University of Education, Sapporo, Japan.

can be seen. In the temperature range from  $-6$  to  $-4^\circ\text{C}$  values of  $\xi_e$  retrieved close to cloud tops varied from 1.4–1.8. At temperatures from  $-9$  to  $-7^\circ\text{C}$  isometric particles were detected with  $\xi_e$  of 0.8–1.2. In the temperature range from  $-17$  to  $-13^\circ\text{C}$  observed oblate particles mostly had  $\xi_e$  of 0.4–0.6. At temperatures from  $-25$  to  $-20^\circ\text{C}$  ice crystals had  $\xi_e$  of 0.8–1. At the same time, differences in measured and calculated polarizability ratios can be seen in Fig. 6.8 at temperatures from  $-4$  to  $-3^\circ\text{C}$ . As it was mentioned in Sec. 6.1, such cases often had liquid precipitation, which hampered utilization of MWR temperatures and, therefore, temperature from GDAS1 was used. Thus, the differences between polarizability ratios calculated from the laboratory studies and the ones retrieved from remote observations can be caused by uncertainties in temperature values from the GDAS1 data set. Even though the number of cases available from six weeks of measurements is quite low, it is shown that ice particles formed close to the top of mid-level mixed-phase clouds at temperatures warmer than  $\sim -25^\circ\text{C}$  in general have a similar dependence of shape and apparent ice density on ambient temperature as the ones grown in the free-fall chamber.

## 6.4 Orientation of pristine ice crystals

As it was mentioned in Sec. 5.1, the width of the canting angle distribution is described by the degree of orientation  $\kappa$ . The retrieved temperature dependence of  $|\kappa|$  is shown in Fig. 6.9. For the retrieval the 22 cases considered above were used. In the temperature ranges from  $-7$  to  $-3$  °C and from  $-17$  to  $-13$  °C mean values of  $\kappa$  were mainly above 0.7. Thus, observed strongly prolate and oblate particles were mostly characterized by a standard deviation of  $\theta_p$  below  $20^\circ$ . The retrieved values for strongly non-spherical particles are in agreement with results of *Kajikawa [1976]*, *Matrosov et al. [2005]*, and *Melnikov and Straka [2013]*. At temperatures from  $-9$  to  $-7$  °C and below  $-20$  °C mean values of  $\kappa$  were in the range from 0.3 to 0.62 corresponding to a standard deviation of  $\theta_p$  from  $30^\circ$  to  $40^\circ$ . Thus, observed quasi-isotropic ice particles tended to be more randomly oriented in comparison with strongly non-spherical ice crystals. In spite of rare studies devoted to ground-based in situ observations of ice-particle orientations (e.g., *Garrett et al. [2015]*), direct observations of particle orientations at cloud tops are not available for further in-depth evaluations of the dataset retrieved within this work.

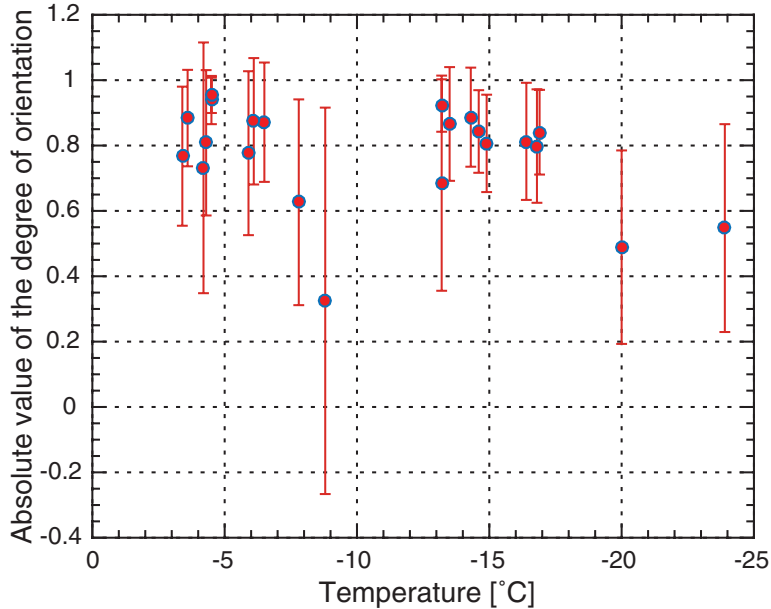


**Figure 6.9:** Temperature dependence of absolute values of the degree of orientation for ice crystals located close to tops of mixed-phase clouds, retrieved from hybrid-mode MIRA-35. Vertical red bars represent  $\pm 1$  standard deviations of observed degree of orientation.



## Chapter 7

# Summary and outlook

Polarimetric cloud radar is one of the remote-sensing instruments that can provide valuable information on ice particle properties. Flexible scanning capabilities of modern cloud radars allow for the implementation of novel algorithms for classification and quantitative description of ice crystals. In this thesis, it was shown that existing backscattering models, assuming the spheroidal approximation of cloud scatterers, permit us to establish a link between a set of measured polarimetric variables and the shape and orientation of cloud particles.

In order to measure a variety of polarimetric variables the new 35-GHz cloud radar MIRA-35 with hybrid polarimetric configuration was implemented in collaboration between TROPOS and METEK GmbH within the ITaRS project. The radar emits the horizontal and vertical components of the transmitted wave simultaneously with the differential phase shift set close to  $0^\circ$ . It was shown in Chapter 4 that the radar permits the measurement of the spectral polarimetric parameters differential reflectivity  $Z_{DR}$ , slanted linear depolarization ratio SLDR, correlation coefficient  $\rho_{hv}$ , cross-correlation coefficient  $\rho_s$  in the slanted basis, and differential phase  $\Phi_{DP}$ . The slanted linear depolarization ratio and the cross-correlation coefficient are derived using the rotation of the measured coherency matrix. Retrieved values of these parameters are consistent with observations of cloud radars with LDR or SLDR mode.

Radar hardware (e.g., antennas) affects the quality of polarimetric variables. Polarization leakage between receiving channels results in biases in the observed  $Z_{DR}$ ,  $\rho_{hv}$ , LDR, and  $\rho_{cx}$  values and, therefore, can cause uncertainties in the retrieved parameters. The biases depend on the quality of the antenna system and thus are specific for a particular radar. In order to estimate the influence of antenna quality on polarimetric observations, high-resolution measurements of complex antenna patterns were conducted. In Chapter 3 measurements of the antenna patterns were discussed, which were performed for the antenna systems of two METEK Ka-band cloud radars, one with a good polarimetric isolation and the other one with a pure polarization isolation. It was shown that up to 80 % of polarization leakage is

---

produced by the struts holding the antenna sub-reflector. Based on the antenna patterns, the biases in polarimetric variables measured in LDR mode were calculated. The obtained values of ICPR (approximately  $-25$  dB and  $-32$  dB for the bad and the good antenna, respectively) were in good agreement with independent ICPR estimates found from measurements with a vertically pointing system in light rain. The  $\rho_{cx}$  biases were found to be about 0.4 and 0.1 for the two antennas, respectively. Estimates of the differences between ICPR values calculated using complex antenna patterns and the upper ICPR bounds computed from the amplitude patterns only were found not to exceed 2.5 dB. Further, a coherency matrix formalism was used to develop an algorithm to correct the observed LDR and  $\rho_{cx}$  for the polarization coupling effects. The correction algorithm was evaluated using measurements of precipitating cloud systems. The intercomparison results from two collocated MIRA-35 cloud radars indicated that the correction uncertainty for LDR was about 3 dB for intrinsic LDR values in a typical range from  $-30$  to  $-10$  dB. The results of applying the correction algorithm to the correlation coefficient show that for volumes filled with isotropic scatterers values of the correlation coefficient were 0 as expected from theoretical considerations. The developed algorithm requires the  $I/Q$  data or coherency matrix measurements in light rain or drizzle. In Chapter 4 a similar approach was applied to the measurements from the developed hybrid-mode cloud radar in order to correct  $Z_{DR}$  and  $\rho_{hv}$ . It was shown that after the correction polarimetric variables are very close to those that would be observed with an “ideal” cloud radar.

In Chapter 5 the developed algorithm for deriving the polarizability ratio  $\xi_e$  and degree of orientation  $\kappa$  of particles based on differential reflectivity  $Z_{DR}$  and correlation coefficient  $\rho_{hv}$  measured by a cloud radar with hybrid polarimetric configuration was presented. The same approach can be applied to slanted linear depolarization ratio SLDR and cross-correlation coefficient  $\rho_s$  measured by a cloud radar with SLDR mode. Registered elevation dependencies of differential reflectivity  $Z_{DR}$  and correlation coefficient  $\rho_{hv}$  were related to polarizability ratios  $\xi_e$  and degree of orientation  $\kappa$  of ice crystals. The polarizability ratio  $\xi_e$  depends on the geometrical axis ratio  $\xi_g$  and apparent ice density  $\rho_a$ , while the degree of orientation  $\kappa$  characterizes the width of the canting angle distribution. In Chapter 5 the algorithm was applied to a complex cloud system. Vertical profiles of the polarizability ratio and the degree of orientation were retrieved. The results showed clouds with oblate ( $\xi_e \approx 0.43 \pm 0.17$ ), prolate ( $\xi_e \approx 1.5 \pm 0.2$ ), and quasi-spherical or low-density particles ( $\xi_e \approx 0.85 \pm 0.07$ ). All these clouds had different cloud-top heights (5 km, 3 km, and 8 km, respectively), indicating different ambient conditions of ice formation. Areas, in which aggregation and/or riming led to ice particle growth, could be detected. High absolute values of the degree of orientation observed in areas dominated by oblate and prolate ice particles indicated their nearly horizontal orientation. The orientation of slightly oblate or low-density ice particles,

---

detected in high-level clouds and in areas with seeding, was found to be more random though the primary orientation was horizontal.

In order to validate the retrieval algorithm, the cloud radar MIRA-35 with the hybrid polarimetric configuration was deployed during the ACCEPT measurement campaign in Cabauw, the Netherlands, in October and November of 2014. The radar was collocated with a vast number of active and passive remote sensors providing continuous information about cloud geometry, ambient conditions, and presence of supercooled liquid layers.

Addressing Question 1 from Chapter 2 (*Is there a way to compare microphysical properties such as shape and apparent density of ice crystals grown in the atmosphere and under laboratory conditions?*), combined analysis of available data allowed for deriving temperature-dependent polarizability ratios of ice crystals at the tops of mixed-phase clouds. As it was mentioned in Chapter 2, ice crystals in mixed-phase clouds at temperatures higher than  $-20$  °C are mostly formed at water saturation conditions. During the ACCEPT campaign thin supercooled liquid tops were observed with the polarimetric lidar Polly<sup>XT</sup>. For the comparison data about ice crystals grown in a free-fall cloud chamber were used. The measurements available from laboratory studies include accurate information about axis lengths and mass of ice crystals grown at water saturation conditions. Even though the remote observations do not provide the exact axis ratios and apparent ice densities, polarizability ratios retrieved from polarimetric measurements can be compared with those calculated using the laboratory data.

Answering Question 2 (*Are temperature dependencies of the shape and apparent ice density of ice crystals grown at water saturation in the atmosphere similar to those found under laboratory conditions?*), a comparison of polarizability ratios of ice crystals investigated in the cloud chamber and those observed close to the cloud tops showed a good agreement. At temperatures in the range from  $-6$  to  $-4$  °C columnar-shaped particles with  $\xi_e$  of 1.2–1.7 and 1.4–1.8 were found in laboratory studies and remote observations, respectively. Isometric particles with  $0.8 < \xi_e < 1.2$  occurred at temperatures near  $-8$  and  $-20$  °C. Oblate particles investigated in the temperature range from  $-17$  to  $-13$  °C had  $\xi_e$  of 0.4–0.6 both in the chamber studies and remote observations. Thus, addressing Question 3 (*Can ice crystals at the top of mixed-phase clouds be considered as pristine?*), from the good correspondence between polarizability ratios of ice particles at the top of mixed-phase clouds and ice crystals grown in laboratories, it was concluded that ice particles located close to the tops of mixed-phase clouds are not significantly influenced by aggregation and/or riming and can be considered as pristine in scattering models in the microwave region.

During the ACCEPT campaign only 22 simple cases available for the analysis were found. Thus, many more polarimetric observations are required to collect a data set that can be used for the further analysis. Special attention should be paid to the analysis of spectral polarimetric variables. As it was mentioned in Sec. 6.2, spectral polarimetry provides a

---

potential for the separation of different populations of ice crystals within a cloud. The separation of ice populations can reduce classification errors and give a potential to study newly produced small ice crystals, which are often masked by the presence of large aggregates in integrated polarimetric variables.

In Sec. 5.3 it was shown that vertical profiles of the polarizability ratio can be used for the characterization of ice-phase evolution. Such characterization is helpful for the investigation of large ice particles such as aggregates and graupel, which often form precipitation at the ground. In order to take into account wind-shear effects, which are frequently present in precipitating cloud systems, polarimetric methods should be accompanied by known fall-streak tracking algorithms (e.g., *Kalesse et al.* [2015]). In addition, as it was mentioned in the introduction section, the quantitative description of the ice particle shape enables the estimation of particle number size distribution and ice mass flux [*Bühl et al.*, 2016] using radar Doppler spectra.

As it was shown in Sec. 4.6, the developed hybrid-mode Ka-band cloud radar provides a large set of spectrally resolved polarimetric variables, which still have to be interpreted for the case of large particles when Mie-scattering effects occur. For instance, *Matrosov et al.* [1999] showed an “oscillation” dependence of polarimetric variables at Ka-band for drops larger than 0.3 mm. Hence, spectral polarimetric variables can be used for improving quantitative precipitation estimation. Such effects are expected to be even more pronounced at W-band. Therefore, there is a great potential of a combination of polarimetric, Doppler, and multi-frequency analysis in cloud radars.

---

---

## Bibliography

- Adler, R. F., G. J. Huffman, A. Chang, R. Ferraro, P.-P. Xie, J. Janowiak, B. Rudolf, U. Schneider, S. Curtis, D. Bolvin, A. Gruber, J. Susskind, P. Arkin, and E. Nelkin (2003), The version-2 global precipitation climatology project (GPCP) monthly precipitation analysis (1979–Present), *Journal of Hydrometeorology*, *4*, 1147–1167, doi:10.1175/1525-7541(2003)004<1147:TVGPCP>2.0.CO;2.
- Althausen, D., R. Engelmann, H. Baars, B. Heese, A. Ansmann, D. Müller, and M. Kompula (2009), Portable Raman lidar Polly<sup>XT</sup> for automated profiling of aerosol backscatter, extinction, and depolarization, *Journal of Atmospheric and Oceanic Technology*, *26*, 2366–2378, doi:10.1175/2009JTECHA1304.1.
- Andreae, M. O. (2009), Correlation between cloud condensation nuclei concentration and aerosol optical thickness in remote and polluted regions, *Atmospheric Chemistry and Physics*, *9*, 543–556, doi:10.5194/acp-9-543-2009.
- Andrić, J., M. R. Kumjian, D. S. Zrnić, J. M. Straka, and V. M. Melnikov (2013), Polarimetric signatures above the melting layer in winter storms: an observational and modeling study, *Journal of Applied Meteorology and Climatology*, *52*, 682–700, doi:10.1175/JAMC-D-12-028.1.
- Ansmann, A., M. Tesche, P. Seifert, D. Althausen, R. Engelmann, J. Fruntke, U. Wandinger, I. Mattis, and D. Müller (2009), Evolution of the ice phase in tropical altocumulus: SAMUM lidar observations over Cape Verde, *Journal of Geophysical Research (Atmospheres)*, *114*, D17208, doi:10.1029/2008JD011659.
- Aydin, K., and J. Singh (2004), Cloud ice crystal classification using a 95-GHz polarimetric radar, *Journal of Atmospheric and Oceanic Technology*, *21*, 1679–1688, doi:10.1175/JTECH1671.1.
- Bailey, M., and J. Hallett (2004), Growth rates and habits of ice crystals between  $-20^{\circ}$  to  $-70^{\circ}$  C, *Journal of Atmospheric Sciences*, *61*, 514–544, doi:10.1175/1520-0469(2004)061<0514:GRAHOI>2.0.CO;2.
-

- Bailey, M. P., and J. Hallett (2009), A comprehensive habit diagram for atmospheric ice crystals: Confirmation from the laboratory, AIRS II, and other field studies, *Journal of Atmospheric Sciences*, *66*, 2888–2899, doi:10.1175/2009JAS2883.1.
- Battaglia, A., M. O. Ajewole, and C. Simmer (2007), Evaluation of radar multiple scattering effects in Cloudsat configuration, *Atmospheric Chemistry and Physics*, *7*, 1719–1730, doi:10.5194/acp-7-1719-2007.
- Battaglia, A., S. Tanelli, S. Kobayashi, D. Zrnica, R. J. Hogan, and C. Simmer (2010), Multiple-scattering in radar systems: A review, *Journal of Quantitative Spectroscopy and Radiative Transfer*, *111*, 917–947, doi:10.1016/j.jqsrt.2009.11.024.
- Baustian, K. J., D. J. Cziczo, M. E. Wise, K. A. Pratt, G. Kulkarni, A. G. Hallar, and M. A. Tolbert (2012), Importance of aerosol composition, mixing state, and morphology for heterogeneous ice nucleation: A combined field and laboratory approach, *Journal of Geophysical Research (Atmospheres)*, *117*, D06217, doi:10.1029/2011JD016784.
- Born, M., and E. Wolf (1975), *Principles of Optics*, 836 pp., Pergamon Press, Oxford.
- Bringi, V. N., and V. Chandrasekar (2001), *Polarimetric Doppler Weather Radar*, 664 pp., Cambridge University Press.
- Bühl, J., A. Ansmann, P. Seifert, H. Baars, and R. Engelmann (2013), Toward a quantitative characterization of heterogeneous ice formation with lidar/radar: Comparison of CALIPSO/CloudSat with ground-based observations, *Geophysical Research Letters*, *40*, 4404–4408, doi:10.1002/grl.50792.
- Bühl, J., P. Seifert, A. Myagkov, and A. Ansmann (2016), Relation between ice and liquid water mass in mixed-phase cloud layers measured with Cloudnet, *Atmospheric Chemistry and Physics Discussions*, *2016*, 1–19, doi:10.5194/acp-2016-25.
- Castellano, N. E., E. E. Avila, R. E. Burgesser, and C. P. R. Saunders (2014), The growth of ice particles in a mixed phase environment based on laboratory observations, *Atmospheric Research*, *150*, 12–20, doi:10.1016/j.atmosres.2014.07.010.
- Chahine, M. T. (1992), The hydrological cycle and its influence on climate, *Nature*, *359*, 373–380, doi:10.1038/359373a0.
- Chandrasekar, V., and R. J. Keeler (1993), Antenna pattern analysis and measurements for multiparameter radars, *Journal of Atmospheric and Oceanic Technology*, *10*, 674–683, doi:10.1175/1520-0426(1993)010<0674:APAAMF>2.0.CO;2.
-

- Chen, M., P. Xie, J. E. Janowiak, and P. A. Arkin (2002), Global land precipitation: A 50-yr monthly analysis based on gauge observations, *Journal of Hydrometeorology*, *3*, 249–266, doi:10.1175/1525-7541(2002)003<0249:GLPAYM>2.0.CO;2.
- Cober, S. G., G. A. Isaac, A. V. Korolev, and J. W. Strapp (2001a), Assessing cloud-phase conditions, *Journal of Applied Meteorology*, *40*, 1967–1983, doi:10.1175/1520-0450(2001)040<1967:ACPC>2.0.CO;2.
- Cober, S. G., G. A. Isaac, and J. W. Strapp (2001b), Characterizations of aircraft icing environments that include supercooled large drops, *Journal of Applied Meteorology*, *40*, 1984–2002, doi:10.1175/1520-0450(2001)040<1984:COAIET>2.0.CO;2.
- Curry, J. A., J. Maslanik, G. Holland, and J. Pinto (2004), Applications of aerosondes in the Arctic, *Bulletin of the American Meteorological Society*, *85*, 1855–1861, doi:10.1175/BAMS-85-12-1855.
- De Boer, G., E. W. Eloranta, and M. D. Shupe (2009), Arctic mixed-phase stratiform cloud properties from multiple years of surface-based measurements at two high-latitude locations, *Journal of Atmospheric Sciences*, *66*, 2874–2887, doi:10.1175/2009JAS3029.1.
- De Boer, G., H. Morrison, M. D. Shupe, and R. Hildner (2011), Evidence of liquid dependent ice nucleation in high-latitude stratiform clouds from surface remote sensors, *Geophysical Research Letters*, *38*, L01803, doi:10.1029/2010GL046016.
- Delanoë, J., and R. J. Hogan (2010), Combined CloudSat-CALIPSO-MODIS retrievals of the properties of ice clouds, *Journal of Geophysical Research (Atmospheres)*, *115*, D00H29, doi:10.1029/2009JD012346.
- Delanoë, J. M. E., A. J. Heymsfield, A. Protat, A. Bansemer, and R. J. Hogan (2014), Normalized particle size distribution for remote sensing application, *Journal of Geophysical Research: Atmospheres*, *119*, 4204–4227, doi:10.1002/2013JD020700.
- DeMott, P. J., D. J. Cziczo, A. J. Prenni, D. M. Murphy, S. M. Kreidenweis, D. S. Thomson, R. Borys, and D. C. Rogers (2003a), Measurements of the concentration and composition of nuclei for cirrus formation, *Proceedings of the National Academy of Science*, *100*, 14655–14660, doi:10.1073/pnas.2532677100.
- DeMott, P. J., K. Sassen, M. R. Poellot, D. Baumgardner, D. C. Rogers, S. D. Brooks, A. J. Prenni, and S. M. Kreidenweis (2003b), African dust aerosols as atmospheric ice nuclei, *Geophysical Research Letters*, *30*, 1732, doi:10.1029/2003GL017410.
- DeMott, P. J., A. J. Prenni, X. Liu, S. M. Kreidenweis, M. D. Petters, C. H. Twohy, M. S. Richardson, T. Eidhammer, and D. C. Rogers (2010), Predicting global atmospheric ice
-

- nuclei distributions and their impacts on climate, *Proceedings of the National Academy of Sciences*, *107*, 11217–11222, doi:10.1073/pnas.0910818107.
- DeMott, P. J., A. J. Prenni, G. R. McMeeking, R. C. Sullivan, M. D. Petters, Y. Tobo, M. Niemand, O. Möhler, J. R. Snider, Z. Wang, and S. M. Kreidenweis (2015), Integrating laboratory and field data to quantify the immersion freezing ice nucleation activity of mineral dust particles, *Atmospheric Chemistry and Physics*, *15*, 393–409, doi:10.5194/acp-15-393-2015.
- Di Girolamo, P., D. Summa, M. Cacciani, E. G. Norton, G. Peters, and Y. Dufournet (2012), Lidar and radar measurements of the melting layer: Observations of dark and bright band phenomena, *Atmospheric Chemistry and Physics*, *12*, 4143–4157, doi:10.5194/acp-12-4143-2012.
- Doviak, R. J., D. S. Zrnic, and D. S. Sirmans (1979), Doppler weather radar, *Proceedings of the IEEE*, *67*, 1522–1553, doi:10.1109/PROC.1979.11511.
- Field, P. R., R. J. Hogan, P. R. A. Brown, A. J. Illingworth, T. W. Chouarton, P. H. Kaye, E. Hirst, and R. Greenaway (2004), Simultaneous radar and aircraft observations of mixed-phase cloud at the 100 m scale, *Quarterly Journal of the Royal Meteorological Society*, *130*, 1877–1904, doi:10.1256/qj.03.102.
- Findeisen, W., E. Volken, A. M. Giesche, and S. Brönnimann (2015), Colloidal meteorological processes in the formation of precipitation, *Meteorologische Zeitschrift*, *24*, 443–454, doi:10.1127/metz/2015/0675.
- Flato, G., J. Marotzke, B. Abiodun, P. Braconnot, S. Chou, W. Collins, P. Cox, F. Driouech, S. Emori, V. Eyring, C. Forest, P. Gleckler, E. Guilyardi, C. Jakob, V. Kattsov, C. Reason, and M. Rummukainen (2013), *Evaluation of Climate Models*, book section 9, pp. 741–866, Cambridge University Press, Cambridge, United Kingdom and New York, NY, USA, doi:10.1017/CBO9781107415324.020.
- Fleishauer, R. P., V. E. Larson, and T. H. Vonder Haar (2002), Observed microphysical structure of midlevel, mixed-phase clouds, *Journal of Atmospheric Sciences*, *59*, 1779–1804, doi:10.1175/1520-0469(2002)059<1779:OMSOMM>2.0.CO;2.
- Frech, M., B. Lange, T. Mammen, J. Seltmann, C. Morehead, and J. Rowan (2013), Influence of a radome on antenna performance, *Journal of Atmospheric and Oceanic Technology*, *30*, 313–324, doi:10.1175/JTECH-D-12-00033.1.
- Fukuta, N. (1969), Experimental studies on the growth of small ice crystals, *Journal of Atmospheric Sciences*, *26*, 522–531, doi:10.1175/1520-0469(1969)026<0522:ESOTGO>2.0.CO;2.
-



- Fukuta, N., and T. Takahashi (1999), The growth of atmospheric ice crystals: A summary of findings in vertical supercooled cloud tunnel studies, *Journal of Atmospheric Sciences*, *56*, 1963–1979, doi:10.1175/1520-0469(1999)056<1963:TGOAIC>2.0.CO;2.
- Galletti, M. (2013), Atmospheric radar, International patent WO 2013/192308.
- Galletti, M., and D. S. Zrnic (2012), Degree of polarization at simultaneous transmit: Theoretical aspects, *IEEE Geoscience and Remote Sensing Letters*, *9*, 383–387, doi:10.1109/LGRS.2011.2170150.
- Galletti, M., D. S. Zrnic, V. M. Melnikov, and R. J. Doviak (2012), Degree of polarization at horizontal transmit: Theory and applications for weather radar, *IEEE Transactions on Geoscience and Remote Sensing*, *50*, 1291–1301, doi:10.1109/TGRS.2011.2167516.
- Galletti, M., D. Huang, and P. Kollias (2014a), Zenith/nadir pointing mm-wave radars: Linear or circular polarization?, *IEEE Transactions on Geoscience and Remote Sensing*, *52*, 628–639, doi:10.1109/TGRS.2013.2243155.
- Galletti, M., D. S. Zrnic, F. Gekat, and P. Goelz (2014b), Eigenvalue signal processing for weather radar polarimetry: Removing the bias induced by antenna coherent cross-channel coupling, *IEEE Transactions on Geoscience and Remote Sensing*, *52*, 7695–7707, doi:10.1109/TGRS.2014.2316821.
- Galloway, J., A. Pazmany, J. Mead, R. E. McIntosh, D. Leon, J. French, R. Kelly, and G. Vali (1997), Detection of ice hydrometeor alignment using an airborne W-band polarimetric radar, *Journal of Atmospheric and Oceanic Technology*, *14*, 3–12, doi:10.1175/1520-0426(1997)014<0003:DOIHAU>2.0.CO;2.
- Garrett, T. J., S. E. Yuter, C. Fallgatter, K. Shkurko, S. R. Rhodes, and J. L. Endries (2015), Orientations and aspect ratios of falling snow, *Geophysical Research Letters*, *42*, 4617–4622, doi:10.1002/2015GL064040.
- Gibbs, J. W. (1878), On the equilibrium of heterogeneous substances, *American Journal of Science*, *16*, 441–458, doi:10.2475/ajs.s3-16.96.441.
- Görsdorf, U., V. Lehmann, M. Bauer-Pfundstein, G. Peters, D. Vavriv, V. Vinogradov, and V. Volkov (2015), A 35-GHz polarimetric Doppler radar for long term observations of cloud parameters - Description of system and data processing, *Journal of Atmospheric and Oceanic Technology*, *32*, 675–690, doi:10.1175/JTECH-D-14-00066.1.
- Hallett, J. (1974), Production of secondary ice particles during the riming process, *Nature*, *249*, 26–28, doi:10.1038/249026a0.
-

- Hendry, A., G. C. McCormick, and B. L. Barge (1976), The degree of common orientation of hydrometeors observed by polarization diversity radars., *Journal of Applied Meteorology*, 15, 633–640, doi:10.1175/1520-0450(1976)015<0633:TDOCOO>2.0.CO;2.
- Heymsfield, A. J., A. Bansemer, P. R. Field, S. L. Durden, J. L. Stith, J. E. Dye, W. Hall, and C. A. Grainger (2002), Observations and parameterizations of particle size distributions in deep tropical cirrus and stratiform precipitating clouds: Results from in situ observations in TRMM field campaigns, *Journal of Atmospheric Sciences*, 59, 3457–3491, doi:10.1175/1520-0469(2002)059<3457:OAPOPS>2.0.CO;2.
- Hildebrand, P. H., and R. S. Sekhon (1974), Objective determination of the noise level in Doppler spectra, *Journal of Applied Meteorology*, 13, 808–811, doi:10.1175/1520-0450(1974)013<0808:ODOTNL>2.0.CO;2.
- Hogan, R. J., P. R. Field, A. J. Illingworth, R. J. Cotton, and T. W. Choullarton (2002), Properties of embedded convection in warm-frontal mixed-phase cloud from aircraft and polarimetric radar, *Quarterly Journal of the Royal Meteorological Society*, 128, 451–476, doi:10.1256/003590002321042054.
- Hogan, R. J., P. N. Francis, H. Flentje, A. J. Illingworth, M. Quante, and J. Pelon (2003), Characteristics of mixed-phase clouds. I: Lidar, radar and aircraft observations from CLARE'98, *Quarterly Journal of the Royal Meteorological Society*, 129, 2089–2116, doi:10.1256/rj.01.208.
- Holt, A. R. (1984), Some factors affecting the remote sensing of rain by polarization diversity radar in the 3- to 35-GHz frequency range, *Radio Science*, 19, 1399–1412, doi:10.1029/RS019i005p01399.
- Hoose, C., and O. Möhler (2012), Heterogeneous ice nucleation on atmospheric aerosols: a review of results from laboratory experiments, *Atmospheric Chemistry and Physics*, 12, 9817–9854, doi:10.5194/acp-12-9817-2012.
- Huuskonen, A., E. Saltikoff, and I. Holleman (2013), The operational weather radar network in Europe, *Bulletin of the American Meteorological Society*, 95, 897–907, doi:10.1175/BAMS-D-12-00216.1.
- Illingworth, A. J., R. J. Hogan, E. J. O'Connor, D. Bouniol, J. Delano, J. Pelon, A. Protat, M. E. Brooks, N. Gaussiat, D. R. Wilson, D. P. Donovan, H. K. Baltink, G.-J. van Zadelhoff, J. D. Eastment, J. W. F. Goddard, C. L. Wrench, M. Haeffelin, O. A. Krasnov, H. W. J. Russchenberg, J.-M. Piriou, F. Vinit, A. Seifert, A. M. Tompkins, and U. Willn (2007), Cloudnet, *Bulletin of the American Meteorological Society*, 88, 883–898, doi:10.1175/BAMS-88-6-883.
-

- Kajikawa, M. (1976), Observation of falling motion of columnar snow crystals, *Journal of the Meteorological Society of Japan. Ser. II*, 54, 276–284.
- Kalesse, H., W. Szyrmer, S. Kneifel, P. Kollias, and E. Luke (2015), Fingerprints of a riming event on cloud radar Doppler spectra: observations and modeling, *Atmospheric Chemistry & Physics Discussions*, 15, 28619–28658, doi:10.5194/acpd-15-28619-2015.
- Kampe, H. J., H. K. Weickmann, and J. J. Kelly (1951), The influence of temperature on the shape of ice crystals growing at water saturation, *Journal of Atmospheric Sciences*, 8, 168–174, doi:10.1175/1520-0469(1951)008<0168:TIIOTOT>2.0.CO;2.
- Kamphus, M., M. Ettner-Mahl, T. Klimach, F. Drewnick, L. Keller, D. J. Cziczo, S. Mertes, S. Borrmann, and J. Curtius (2010), Chemical composition of ambient aerosol, ice residues and cloud droplet residues in mixed-phase clouds: Single particle analysis during the cloud and aerosol characterization experiment (CLACE 6), *Atmospheric Chemistry and Physics*, 10, 8077–8095, doi:10.5194/acp-10-8077-2010.
- Kanamitsu, M. (1989), Description of the NMC global data assimilation and forecast system, *Weather and Forecasting*, 4, 335–342, doi:10.1175/1520-0434(1989)004<0335:DOTNGD>2.0.CO;2.
- Kanareykin, D. B., N. F. Pavlov, and V. A. Potechin (1966), *Polarization of Radar Signals*, 440 pp., Sov. Radio, [In Russian].
- Kanareykin, D. B., V. A. Potechin, and I. F. Shishkin (1968), *Marine Radio Polarimetry*, 328 pp., Sudostroenie, [In Russian].
- Kanitz, T., P. Seifert, A. Ansmann, R. Engelmann, D. Althausen, C. Casaccia, and E. G. Rohwer (2011), Contrasting the impact of aerosols at northern and southern midlatitudes on heterogeneous ice formation, *Geophysical Research Letters*, 38, L17802, doi:10.1029/2011GL048532.
- Kankiewicz, J. A., C. J. Seaman, S. Q. Kidder, T. H. Vonder Haar, and L. D. Carey (2005), An overview of the next cloud layer experiment (clex-10), in *Battlespace Atmosphere and Cloud Impacts on Military Operations (BACIMO) Conference*, Monterey, CA, 11-15 October 2005.
- Keller, V., and J. Hallett (1982), Influence of air velocity on the habit of ice crystal growth from the vapor, *Journal of Crystal Growth*, 60, 91–106, doi:10.1016/0022-0248(82)90176-2.
- Kneifel, S., M. S. Kulie, and R. Bennartz (2011), A triple-frequency approach to retrieve microphysical snowfall parameters, *Journal of Geophysical Research (Atmospheres)*, 116, D11203, doi:10.1029/2010JD015430.
-

- Kneifel, S., A. von Lerber, J. Tiira, D. Moisseev, P. Kollias, and J. Leinonen (2015), Observed relations between snowfall microphysics and triple-frequency radar measurements, *Journal of Geophysical Research (Atmospheres)*, pp. 6034–6055, doi:10.1002/2015JD023156, 2015JD023156.
- Kollias, P., E. E. Clothiaux, M. A. Miller, B. A. Albrecht, G. L. Stephens, and T. P. Ackerman (2007), Millimeter-wavelength radars: New frontier in atmospheric cloud and precipitation research, *Bulletin of the American Meteorological Society*, 88, 1608–1624, doi:10.1175/BAMS-88-10-1608.
- Korolev, A. V., and I. P. Mazin (2003), Supersaturation of water vapor in clouds, *Journal of Atmospheric Sciences*, 60, 2957–2974, doi:10.1175/1520-0469(2003)060<2957:SOWVIC>2.0.CO;2.
- Korolev, A. V., G. A. Isaac, S. G. Cober, J. W. Strapp, and J. Hallett (2003), Microphysical characterization of mixed-phase clouds, *Quarterly Journal of the Royal Meteorological Society*, 129, 39–65, doi:10.1256/qj.01.204.
- Korolev, A. V., G. A. Isaac, J. W. Strapp, S. G. Cober, and H. W. Barker (2007), In situ measurements of liquid water content profiles in midlatitude stratiform clouds, *Quarterly Journal of the Royal Meteorological Society*, 133, 1693–1699, doi:10.1002/qj.147.
- Kumjian, M. R. (2012), The impact of precipitation physical processes on the polarimetric radar variables, Ph.D. thesis, University of Oklahoma.
- Kumjian, M. R., and A. V. Ryzhkov (2010), The impact of evaporation on polarimetric characteristics of rain: Theoretical model and practical implications, *Journal of Applied Meteorology and Climatology*, 49, 1247–1267, doi:10.1175/2010JAMC2243.1.
- Kumjian, M. R., and A. V. Ryzhkov (2012), The impact of size sorting on the polarimetric radar variables, *Journal of Atmospheric Sciences*, 69, 2042–2060, doi:10.1175/JAS-D-11-0125.1.
- Kumjian, M. R., S. M. Ganson, and A. V. Ryzhkov (2012), Freezing of raindrops in deep convective updrafts: A microphysical and polarimetric model, *Journal of Atmospheric Sciences*, 69, 3471–3490, doi:10.1175/JAS-D-12-067.1.
- Kuroda, T. (1983), Recent developments in theory and experiment of growth kinetics of ice crystals from the vapour phase and their growth forms, *Journal of Crystal Growth*, 65, 27–35, doi:10.1016/0022-0248(83)90032-5.
- Kuroda, T., and R. Lacmann (1982), Growth kinetics of ice from the vapour phase and its growth forms, *Journal of Crystal Growth*, 56, 189–205, doi:10.1016/0022-0248(82)90028-8.
-

- Ladino Moreno, L. A., O. Stetzer, and U. Lohmann (2013), Contact freezing: a review of experimental studies, *Atmospheric Chemistry and Physics*, *13*, 9745–9769, doi:10.5194/acp-13-9745-2013.
- Lamb, D., and P. V. Hobbs (1971), Growth rates and habits of ice crystals grown from the vapor phase, *Journal of Atmospheric Sciences*, *28*, 1507–1508, doi:10.1175/1520-0469(1971)028<1507:GRAHOI>2.0.CO;2.
- Libbrecht, K. G. (2005), The physics of snow crystals, *Reports on Progress in Physics*, *68*, 855–895, doi:10.1088/0034-4885/68/4/R03.
- Liu, Y., W. Wu, M. P. Jensen, and T. Toto (2011), Relationship between cloud radiative forcing, cloud fraction and cloud albedo, and new surface-based approach for determining cloud albedo, *Atmospheric Chemistry and Physics*, *11*, 7155–7170, doi:10.5194/acp-11-7155-2011.
- Loeb, N. G., B. A. Wielicki, D. R. Doelling, G. L. Smith, D. F. Keyes, S. Kato, N. Manalo-Smith, and T. Wong (2009), Toward optimal closure of the Earth’s top-of-atmosphere radiation budget, *Journal of Climate*, *22*, 748–766, doi:10.1175/2008JCLI2637.1.
- Lohmeier, S. P., S. M. Sekelsky, J. M. Firda, G. A. Sadowy, and R. E. McIntosh (1997), Classification of particles in stratiform clouds using the 33 and 95 GHz polarimetric cloud profiling radar system (CPRS), *IEEE Transactions on Geoscience and Remote Sensing*, *35*, 256–270, doi:10.1109/36.563264.
- Löhnert, U., J. H. Schween, C. Acquistapace, K. Ebell, M. Maahn, M. Barreraverdejo, A. Hirsikko, B. Bohn, A. Knaps, E. O’connor, C. Simmer, A. Wahner, and S. Crewell (2015), JOYCE: Jülich observatory for cloud evolution, *Bulletin of the American Meteorological Society*, *96*, 1157–1174, doi:10.1175/BAMS-D-14-00105.1.
- Luke, E. P., P. Kollias, and M. D. Shupe (2010), Detection of supercooled liquid in mixed-phase clouds using radar Doppler spectra, *Journal of Geophysical Research (Atmospheres)*, *115*, D19201, doi:10.1029/2009JD012884.
- Mace, G. G., A. J. Heymsfield, and M. R. Poellot (2002), On retrieving the microphysical properties of cirrus clouds using the moments of the millimeter-wavelength Doppler spectrum, *Journal of Geophysical Research (Atmospheres)*, *107*, 4815, doi:10.1029/2001JD001308.
- Marcuvitz, M. (1965), *Waveguide Handbook*, 428 pp., Dover Publications, Inc.
- Martner, B. E., and K. P. Moran (2001), Using cloud radar polarization measurements to evaluate stratus cloud and insect echoes, *Journal of Geophysical Research (Atmospheres)*, *106*, 4891–4897, doi:10.1029/2000JD900623.
-

- Martucci, G., and C. D. O'Dowd (2011), Ground-based retrieval of continental and marine warm cloud microphysics, *Atmospheric Measurement Techniques*, *4*, 2749–2765, doi:10.5194/amt-4-2749-2011.
- Matrosov, S. Y. (1991a), Theoretical study of radar polarization parameters obtained from cirrus clouds, *Journal of Atmospheric Sciences*, *48*, 1062–1070, doi:10.1175/1520-0469(1991)048<1062:TSORPP>2.0.CO;2.
- Matrosov, S. Y. (1991b), Prospects for the measurement of ice cloud particle shape and orientation with elliptically polarized radar signals, *Radio Science*, *26*, 847–856, doi:10.1029/91RS00965.
- Matrosov, S. Y. (2015), Evaluations of the spheroidal particle model for describing cloud radar depolarization ratios of ice hydrometeors, *Journal of Atmospheric and Oceanic Technology*, *32*, 865–879, doi:10.1175/JTECH-D-14-00115.1.
- Matrosov, S. Y., and R. A. Kropfli (1993), Cirrus cloud studies with elliptically polarized Ka-band radar signals: A suggested approach, *Journal of Atmospheric and Oceanic Technology*, *10*, 684–692, doi:10.1175/1520-0426(1993)010<0684:CCSWEP>2.0.CO;2.
- Matrosov, S. Y., R. A. Kropfli, R. F. Reinking, and B. E. Martner (1999), Prospects for measuring rainfall using propagation differential phase in X- and  $K_a$ -radar bands, *Journal of Applied Meteorology*, *38*, 766–776, doi:10.1175/1520-0450(1999)038<0766:PFMRUP>2.0.CO;2.
- Matrosov, S. Y., R. F. Reinking, R. A. Kropfli, B. E. Martner, and B. W. Bartram (2001), On the use of radar depolarization ratios for estimating shapes of ice hydrometeors in winter clouds, *Journal of Applied Meteorology*, *40*, 479–490, doi:10.1175/1520-0450(2001)040<0479:OTUORD>2.0.CO;2.
- Matrosov, S. Y., R. F. Reinking, and I. V. Djalalova (2005), Inferring Fall Attitudes of Pristine Dendritic Crystals from Polarimetric Radar Data, *Journal of Atmospheric Sciences*, *62*, 241–250, doi:10.1175/JAS-3356.1.
- Matrosov, S. Y., G. G. Mace, R. Marchand, M. D. Shupe, A. G. Hallar, and I. B. McCubbin (2012), Observations of ice crystal habits with a scanning polarimetric W-band radar at slant linear depolarization ratio mode, *Journal of Atmospheric and Oceanic Technology*, *29*, 989–1008, doi:10.1175/JTECH-D-11-00131.1.
- Matsuo, T., and N. Fukuta (1987), Experimental study of ice crystal growth below water saturation in the university of utah supercooled cloud tunnel, *Papers in Meteorology and Geophysics*, *38*, 247–264, doi:10.2467/mripapers.38.247.
-

- Mazin, I. P. (2006), Cloud phase structure: Experimental data analysis and parameterization, *Journal of Atmospheric Sciences*, *63*, 667–681, doi:10.1175/JAS3660.1.
- Mazin, I. P., and A. K. Khrgian (1989), *Clouds and Cloudy Atmosphere*, 647 pp., Gidrometeoizdat, [In Russian].
- McCormick, G. C., and A. Hendry (1975), Principles for the radar determination of the polarization properties of precipitation, *Radio Science*, *10*, 421–434, doi:10.1029/RS010i004p00421.
- McFarquhar, G. M., and S. G. Cober (2004), Single-scattering properties of mixed-phase arctic clouds at solar wavelengths: Impacts on radiative transfer, *Journal of Climate*, *17*, 3799–3813, doi:10.1175/1520-0442(2004)017<3799:SPOMAC>2.0.CO;2.
- McFarquhar, G. M., J. Um, and R. Jackson (2013), Small cloud particle shapes in mixed-phase clouds, *Journal of Applied Meteorology and Climatology*, *52*, 1277–1293, doi:10.1175/JAMC-D-12-0114.1.
- Mech, M., E. Orlandi, S. Crewell, F. Ament, L. Hirsch, M. Hagen, G. Peters, and B. Stevens (2014), HAMP - the microwave package on the High Altitude and Long range research aircraft (HALO), *Atmospheric Measurement Techniques*, *7*, 4539–4553, doi:10.5194/amt-7-4539-2014.
- Melnikov, V., and J. M. Straka (2013), Axis ratios and flutter angles of cloud ice particles: Retrievals from radar data, *Journal of Atmospheric and Oceanic Technology*, *30*, 1691–1703, doi:10.1175/JTECH-D-12-00212.1.
- Melnikov, V. M., R. J. Doviak, D. S. Zrnić, and D. J. Stensrud (2011), Mapping Bragg scatter with a polarimetric WSR-88D, *Journal of Atmospheric and Oceanic Technology*, *28*, 1273–1285, doi:10.1175/JTECH-D-10-05048.1.
- Mitchell, D. L. (1996), Use of mass- and area-dimensional power laws for determining precipitation particle terminal velocities, *Journal of Atmospheric Sciences*, *53*, 1710–1723, doi:10.1175/1520-0469(1996)053<1710:UOMAAD>2.0.CO;2.
- Morrison, H., G. de Boer, G. Feingold, J. Harrington, M. D. Shupe, and K. Sulia (2012), Resilience of persistent Arctic mixed-phase clouds, *Nature Geoscience*, *5*, 11–17, doi:10.1038/ngeo1332.
- Mudukutore, A., V. Chandrasekar, and E. A. Mueller (1995), The differential phase pattern of the CSU CHILL radar antenna, *Journal of Atmospheric and Oceanic Technology*, *12*, 1120–1123, doi:10.1175/1520-0426(1995)012<1120:TDPPOT>2.0.CO;2.
-

- Mülmenstädt, J., O. Sourdeval, J. Delanoë, and J. Quaas (2015), Frequency of occurrence of rain from liquid-, mixed-, and ice-phase clouds derived from A-Train satellite retrievals, *Geophysical Research Letters*, *42*, 6502–6509, doi:10.1002/2015GL064604.
- Murray, B. J., D. O’Sullivan, J. D. Atkinson, and M. E. Webb (2012), Ice nucleation by particles immersed in supercooled cloud droplets, *Chemical Society Reviews*, *41*, 6519–6554, doi:10.1039/C2CS35200A.
- Myagkov, A., P. Seifert, U. Wandinger, M. Bauer-Pfundstein, and S. Y. Matrosov (2015), Effects of antenna patterns on cloud radar polarimetric measurements, *Journal of Atmospheric and Oceanic Technology*, *32*, 1813–1828, doi:10.1175/JTECH-D-15-0045.1.
- Myagkov, A., P. Seifert, M. Bauer-Pfundstein, and U. Wandinger (2016a), Cloud radar with hybrid mode towards estimation of shape and orientation of ice crystals, *Atmospheric Measurement Techniques*, *9*, 469–489, doi:10.5194/amt-9-469-2016.
- Myagkov, A., P. Seifert, U. Wandinger, J. Bühl, and R. Engelmann (2016b), Shape-temperature relationships of pristine ice crystals derived from polarimetric cloud radar observations during the ACCEPT campaign, *Atmospheric Measurement Techniques Discussions*, *2016*, 1–37, doi:10.5194/amt-2015-365.
- Nakaya, U. (1954), *Snow Crystals, Natural and Artificial*, 510 pp., Harvard University Press.
- Nelson, J. (2008), Origin of diversity in falling snow, *Atmospheric Chemistry and Physics*, *8*, 5669–5682, doi:10.5194/acp-8-5669-2008.
- Nghiem, S. V., S. H. Yueh, R. Kwok, and F. K. Li (1992), Symmetry properties in polarimetric remote sensing, *Radio Science*, *27*, 693–711, doi:10.1029/92RS01230.
- Niu, F., and Z. Li (2012), Systematic variations of cloud top temperature and precipitation rate with aerosols over the global tropics, *Atmospheric Chemistry and Physics*, *12*, 8491–8498, doi:10.5194/acp-12-8491-2012.
- Noel, V., and K. Sassen (2005), Study of planar ice crystal orientations in ice clouds from scanning polarization lidar observations, *Journal of Applied Meteorology*, *44*, 653–664, doi:10.1175/JAM2223.1.
- Oguchi, T. (1983), Electromagnetic wave propagation and scattering in rain and other hydrometeors, *IEEE Proceedings*, *71*, 1029–1078, doi:10.1109/PROC.1983.12724.
- Otto, T., and H. W. J. Russchenberg (2011), Estimation of specific differential phase and differential backscatter phase from polarimetric weather radar measurements of rain, *IEEE Geoscience and Remote Sensing Letters*, *8*, 988–992, doi:10.1109/LGRS.2011.2145354.
-



- Oue, M., M. R. Kumjian, Y. Lu, J. Verlinde, K. Aydin, and E. E. Clothiaux (2015), Linear depolarization ratios of columnar ice crystals in a deep precipitating system over the Arctic observed by zenith-pointing Ka-band Doppler radar, *Journal of Applied Meteorology and Climatology*, *54*, 1060–1068, doi:10.1175/JAMC-D-15-0012.1.
- Park, H., A. V. Ryzhkov, D. S. Zrnić, and K.-E. Kim (2009), The hydrometeor classification algorithm for the polarimetric WSR-88D: Description and application to an MCS, *Weather and Forecasting*, *24*, 730, doi:10.1175/2008WAF2222205.1.
- Pazmany, A., J. Mead, R. McIntosh, M. Hervig, R. Kelly, and G. Vali (1994), 95-GHz polarimetric radar measurements of orographic cap clouds, *Journal of Atmospheric and Oceanic Technology*, *11*, 140–153, doi:10.1175/1520-0426(1994)011<0140:GPRMOO>2.0.CO;2.
- Phillips, V. T. J., P. J. Demott, C. Andronache, K. A. Pratt, K. A. Prather, R. Subramanian, and C. Twohy (2013), Improvements to an empirical parameterization of heterogeneous ice nucleation and its comparison with observations, *Journal of Atmospheric Sciences*, *70*, 378–409, doi:10.1175/JAS-D-12-080.1.
- Piras, M., G. Mascaro, R. Deidda, and E. R. Vivoni (2014), Quantification of hydrologic impacts of climate change in a Mediterranean basin in Sardinia, Italy, through high-resolution simulations, *Hydrology and Earth System Sciences Discussions*, *11*, 8493–8535, doi:10.5194/hessd-11-8493-2014.
- Probert-Jones, J. R. (1964), The radar equation in meteorology, *Quarterly Journal of the Royal Meteorological Society*, *90*, 108–109, doi:10.1002/qj.49709038316.
- Pruppacher, H. R., and J. D. Klett (1997), *Microphysics of Clouds and Precipitation*, vol. 18, 954 pp., Springer.
- Rangno, A. L., and P. V. Hobbs (2005), Microstructures and precipitation development in cumulus and small cumulonimbus clouds over the warm pool of the tropical Pacific Ocean, *Quarterly Journal of the Royal Meteorological Society*, *131*, 639–673, doi:10.1256/qj.04.13.
- Rauber, R. M. (1987), Characteristics of cloud ice and precipitation during wintertime storms over the mountains of Northern Colorado, *Journal of Applied Meteorology*, *26*, 488–524, doi:10.1175/1520-0450(1987)026<0488:COCIAP>2.0.CO;2.
- Rauber, R. M., and A. Tokay (1991), An explanation for the existence of supercooled water at the top of cold clouds, *Journal of Atmospheric Sciences*, *48*, 1005–1023, doi:10.1175/1520-0469(1991)048<1005:AEFTEO>2.0.CO;2.
- Ray, P. S. (1972), Broadband complex refractive indices of ice and water, *Applied Optics*, *11*, 1836–1844, doi:10.1364/AO.11.001836.
-

- Reinking, R. F., S. Y. Matrosov, R. A. Kropfli, and B. W. Bartram (2002), Evaluation of a 45° slant quasi-linear radar polarization state for distinguishing drizzle droplets, pristine ice crystals, and less regular ice particles, *Journal of Atmospheric and Oceanic Technology*, 19, 296–321, doi:10.1175/1520-0426-19.3.296.
- Richardson, M. S., P. J. Demott, S. M. Kreidenweis, D. J. Cziczo, E. J. Dunlea, J. L. Jimenez, D. S. Thomson, L. L. Ashbaugh, R. D. Borys, D. L. Westphal, G. S. Casuccio, and T. L. Lersch (2007), Measurements of heterogeneous ice nuclei in the western United States in springtime and their relation to aerosol characteristics, *Journal of Geophysical Research (Atmospheres)*, 112, D02209, doi:10.1029/2006JD007500.
- Rose, T., S. Crewell, U. Löhnert, and C. Simmer (2005), A network suitable microwave radiometer for operational monitoring of the cloudy atmosphere, *Atmospheric Research*, 75, 183–200, doi:10.1016/j.atmosres.2004.12.005.
- Rutledge, S. A., and P. V. Hobbs (1984), The mesoscale and microscale structure and organization of clouds and precipitation in midlatitude cyclones. XII: A diagnostic modeling study of precipitation development in narrow cold-frontal rainbands, *Journal of Atmospheric Sciences*, 41, 2949–2972, doi:10.1175/1520-0469(1984)041<2949:TMAMSA>2.0.CO;2.
- Ryan, B. F., E. R. Wishart, and D. E. Shaw (1976), The Growth Rates and Densities of Ice Crystals between  $-3^{\circ}$  and  $-21^{\circ}$  C, *Journal of Atmospheric Sciences*, 33, 842–850, doi:10.1175/1520-0469(1976)033<0842:TGRADO>2.0.CO;2.
- Ryzhkov, A. V. (2001), Interpretation of polarimetric radar covariance matrix for meteorological scatterers: Theoretical analysis, *Journal of Atmospheric and Oceanic Technology*, 18, 315–328, doi:10.1175/1520-0426(2001)018<0315:IOPRCM>2.0.CO;2.
- Ryzhkov, A. V., D. S. Zrnic, J. C. Hubbert, V. N. Bringi, J. Vivekanandan, and E. A. Brandes (2002), Polarimetric radar observations and interpretation of co-cross-polar correlation coefficients, *Journal of Atmospheric and Oceanic Technology*, 19, 340–354, doi:10.1175/1520-0426-19.3.340.
- Ryzhkov, A. V., T. J. Schuur, D. W. Burgess, P. L. Heinselman, S. E. Giangrande, and D. S. Zrnic (2005a), The joint polarization experiment: Polarimetric rainfall measurements and hydrometeor classification., *Bulletin of the American Meteorological Society*, 86, 809–824, doi:10.1175/BAMS-86-6-809.
- Ryzhkov, A. V., T. J. Schuur, D. W. Burgess, and D. S. Zrnic (2005b), Polarimetric tornado detection, *Journal of Applied Meteorology*, 44, 557–570, doi:10.1175/JAM2235.1.
-

- Sand, W. R., W. A. Cooper, M. K. Politovich, and D. L. Veal (1984), Icing conditions encountered by a research aircraft, *Journal of Applied Meteorology*, *23*, 1427–1440, doi:10.1175/0733-3021-23.10.1427.
- Sassen, K. (1980), Remote sensing of planar ice crystal fall attitudes, *Journal of the Meteorological Society of Japan*, *58*, 422–429.
- Sassen, K. (2002), Indirect climate forcing over the western US from Asian dust storms, *Geophysical Research Letters*, *29*, 1465, doi:10.1029/2001GL014051.
- Sassen, K., and V. I. Khvorostyanov (2008), Cloud effects from boreal forest fire smoke: evidence for ice nucleation from polarization lidar data and cloud model simulations, *Environmental Research Letters*, *3*, 025006, doi:10.1088/1748-9326/3/2/025006.
- Sassen, K., P. J. DeMott, J. M. Prospero, and M. R. Poellot (2003), Saharan dust storms and indirect aerosol effects on clouds: CRYSTAL-FACE results, *Geophysical Research Letters*, *30*, 1633, doi:10.1029/2003GL017371.
- Schotland, R. M., K. Sassen, and R. Stone (1971), Observations by lidar of linear depolarization ratios for hydrometeors, *Journal of Applied Meteorology*, *10*, 1011–1017, doi:10.1175/1520-0450(1971)010<1011:OBLOLD>2.0.CO;2.
- Seifert, A., and K. D. Beheng (2006), A two-moment cloud microphysics parameterization for mixed-phase clouds. Part 1: Model description, *Meteorology and Atmospheric Physics*, *92*, 45–66, doi:10.1007/s00703-005-0112-4.
- Seifert, P., A. Ansmann, I. Mattis, U. Wandinger, M. Tesche, R. Engelmann, D. Müller, C. Pérez, and K. Hausteiner (2010), Saharan dust and heterogeneous ice formation: Eleven years of cloud observations at a central European EARLINET site, *Journal of Geophysical Research (Atmospheres)*, *115*, D20201, doi:10.1029/2009JD013222.
- Seifert, P., C. Kunz, H. Baars, A. Ansmann, J. Bühl, F. Senf, R. Engelmann, D. Althausen, and P. Artaxo (2015), Seasonal variability of heterogeneous ice formation in stratiform clouds over the Amazon Basin, *Geophysical Research Letters*, *42*, 5587–5593, doi:10.1002/2015GL064068.
- Seliga, T. A., and V. N. Bringi (1978), Differential reflectivity and differential phase shift: Applications in radar meteorology, *Radio Science*, *13*, 271–275, doi:10.1029/RS013i002p00271.
- Shupe, M. D. (2011), Clouds at Arctic atmospheric observatories. Part II: Thermodynamic phase characteristics, *Journal of Applied Meteorology and Climatology*, *50*, 645–661, doi:10.1175/2010JAMC2468.1.
-

- Shupe, M. D., J. S. Daniel, G. de Boer, E. W. Eloranta, P. Kollias, C. N. Long, E. P. Luke, D. D. Turner, and J. Verlinde (2008), A focus on mixed-phase clouds, *Bulletin of the American Meteorological Society*, *89*, 1549–1562, doi:10.1175/2008BAMS2378.1.
- Siquig, R. A. (1990), Impact of icing on unmanned aerial vehicle operations, *Tech. rep.*, Naval environmental prediction research facility, Monterey, CA, 8 pp.
- Skolnik, M. (1980), *Introduction to Radar Systems*, 581 pp., McGraw-Hill.
- Smith, A. J., V. E. Larson, J. Niu, J. A. Kankiewicz, and L. D. Carey (2009), Processes that generate and deplete liquid water and snow in thin midlevel mixed-phase clouds, *Journal of Geophysical Research (Atmospheres)*, *114*, D12203, doi:10.1029/2008JD011531.
- Spek, A. L. J., C. M. H. Unal, D. N. Moisseev, H. W. J. Russchenberg, V. Chandrasekar, and Y. Dufournet (2008), A new technique to categorize and retrieve the microphysical properties of ice particles above the melting layer using radar dual-polarization spectral analysis, *Journal of Atmospheric and Oceanic Technology*, *25*, 482–497, doi:10.1175/2007JTECHA944.1.
- Stephens, G. L., D. G. Vane, S. Tanelli, E. Im, S. Durden, M. Rokey, D. Reinke, P. Partain, G. G. Mace, R. Austin, T. L'Ecuyer, J. Haynes, M. Lebsock, K. Suzuki, D. Waliser, D. Wu, J. Kay, A. Gettelman, Z. Wang, and R. Marchand (2008), Cloudsat mission: Performance and early science after the first year of operation, *Journal of Geophysical Research (Atmospheres)*, *113*(D8), D00A18, doi:10.1029/2008JD009982, d00A18.
- Straka, J. M., D. S. Zrni, and A. V. Ryzhkov (2000), Bulk hydrometeor classification and quantification using polarimetric radar data: Synthesis of relations, *Journal of Applied Meteorology*, *39*, 1341–1372, doi:10.1175/1520-0450(2000)039<1341:BHCAQU>2.0.CO;2.
- Sun, Z., and K. P. Shine (1994), Studies of the radiative properties of ice and mixed-phase clouds, *Quarterly Journal of the Royal Meteorological Society*, *120*, 111–137, doi:10.1002/qj.49712051508.
- Sun, Z., and K. P. Shine (1995), Parameterization of ice cloud radiative properties and its application to the potential climatic importance of mixed-phase clouds, *Journal of Climate*, *8*, 1874–1888, doi:10.1175/1520-0442(1995)008<1874:POICRP>2.0.CO;2.
- Suortti, T. M., A. Kats, R. Kivi, N. Kämpfer, U. Leiterer, L. M. Miloshevich, R. Neuber, A. Paukkunen, P. Ruppert, H. Vömel, and V. Yushkov (2008), Tropospheric comparisons of Vaisala radiosondes and balloon-borne frost-point and Lyman- $\alpha$  hygrometers during the LAUTLOS-WAVVAP experiment, *Journal of Atmospheric and Oceanic Technology*, *25*, 149–166, doi:10.1175/2007JTECHA887.1.
-

- Takahashi, T. (2014), Influence of liquid water content and temperature on the form and growth of branched planar snow crystals in a cloud, *Journal of Atmospheric Sciences*, *71*, 4127–4142, doi:10.1175/JAS-D-14-0043.1.
- Takahashi, T., and N. Fukuta (1988), Supercooled cloud tunnel studies on the growth of snow crystals between  $-4^{\circ}$  and  $-20^{\circ}\text{C}$ , *Journal of the Meteorological Society of Japan. Ser. II*, *66*, 841–855.
- Takahashi, T., T. Endoh, G. Wakahama, and N. Fukuta (1991), Vapor diffusional growth of free-falling snow crystals between  $-3^{\circ}$  and  $-23^{\circ}\text{C}$ , *Journal of the Meteorological Society of Japan. Ser. II*, *69*, 15–30.
- Tao, W.-K., and M. W. Moncrieff (2009), Multiscale cloud system modeling, *Reviews of Geophysics*, *47*, RG4002, doi:10.1029/2008RG000276.
- Tatarinov, V. N., and S. V. Tatarinov (2011), A statistical theory of the electromagnetic field polarization parameters at the scattering by distributed radar objects. *Wave Propagation*, p. 513–538, InTech.
- Tippett, M., J. Allen, V. Gensini, and H. Brooks (2015), Climate and hazardous convective weather, *Current Climate Change Reports*, *1*, 60–73, doi:10.1007/s40641-015-0006-6.
- Trömel, S., M. R. Kumjian, A. V. Ryzhkov, C. Simmer, and M. Diederich (2013), Backscatter differential phase–estimation and variability, *Journal of Applied Meteorology and Climatology*, *52*, 2529–2548, doi:10.1175/JAMC-D-13-0124.1.
- Vali, G., P. J. DeMott, O. Möhler, and T. F. Whale (2015), Technical Note: A proposal for ice nucleation terminology, *Atmospheric Chemistry & Physics*, *15*, 10263–10270, doi:10.5194/acp-15-10263-2015.
- Verlinde, J., J. Y. Harrington, G. M. McFarquhar, V. T. Yannuzzi, A. Avramov, S. Greenberg, N. Johnson, G. Zhang, M. R. Poellot, J. H. Mather, D. D. Turner, E. W. Eloranta, B. D. Zak, A. J. Prenni, J. S. Daniel, G. L. Kok, D. C. Tobin, R. Holz, K. Sassen, D. Spangenberg, P. Minnis, T. P. Tooman, M. D. Ivey, S. J. Richardson, C. P. Bahrmann, M. Shupe, P. J. Demott, A. J. Heymsfield, and R. Schofield (2007), The Mixed-Phase Arctic Cloud Experiment, *Bulletin of the American Meteorological Society*, *88*, 205–221, doi:10.1175/BAMS-88-2-205.
- Vig, J. R. (1992), Introduction to quartz frequency standards, revision 1, *NASA STI/Recon Technical Report N*, *93*, 15330, [Available online at [www.dtic.mil/dtic/tr/fulltext/u2/a256373.pdf](http://www.dtic.mil/dtic/tr/fulltext/u2/a256373.pdf)].
-

- Wandinger, U., P. Seifert, R. Engelmann, J. Buehl, J. Schmidt, and A. Ansmann (2012), Observation of aerosol-cloud-turbulence interaction with integrated remote-sensing instrumentation, in *Proceedings of the 9th International Symposium on Tropospheric Profiling*, ISBN: 978-90-815839-4-7, L'Aquila, Italy.
- Wang, Y., V. Chandrasekar, and V. N. Bringi (2006), Characterization and evaluation of hybrid polarization observation of precipitation, *Journal of Atmospheric and Oceanic Technology*, *23*, 552–572, doi:10.1175/JTECH1869.1.
- Wang, Z., K. Sassen, D. N. Whiteman, and B. B. Demoz (2004), Studying altocumulus with ice virga using ground-based active and passive remote sensors, *Journal of Applied Meteorology*, *43*, 449–460, doi:10.1175/1520-0450(2004)043<0449:SAWIVU>2.0.CO;2.
- Westbrook, C. D., and A. J. Heymsfield (2011), Ice crystals growing from vapor in supercooled clouds between  $-2.5^{\circ}$  and  $-22^{\circ}\text{C}$ : Testing current parameterization methods using laboratory data, *Journal of Atmospheric Sciences*, *68*, 2416–2429, doi:10.1175/JAS-D-11-017.1.
- Westbrook, C. D., and A. J. Illingworth (2011), Evidence that ice forms primarily in supercooled liquid clouds at temperatures  $-27^{\circ}\text{C}$ , *Geophysical Research Letters*, *38*, L14808, doi:10.1029/2011GL048021.
- Westbrook, C. D., and A. J. Illingworth (2013), The formation of ice in a long-lived supercooled layer cloud, *Quarterly Journal of the Royal Meteorological Society*, *139*, 2209–2221, doi:10.1002/qj.2096.
- Wolde, M., and G. Vali (2001), Polarimetric signatures from ice crystals observed at 95 GHz in winter clouds. Part II: Frequencies of occurrence, *Journal of Atmospheric Sciences*, *58*, 842–849, doi:10.1175/1520-0469(2001)058<0842:PSFICO>2.0.CO;2.
- Wylie, D., D. L. Jackson, W. P. Menzel, and J. J. Bates (2005), Trends in global cloud cover in two decades of HIRS observations, *Journal of Climate*, *18*, 3021–3031, doi:10.1175/JCLI3461.1.
- Xie, P., and P. A. Arkin (1997), Global precipitation: A 17-year monthly analysis based on gauge observations, satellite estimates, and numerical model outputs, *Bulletin of the American Meteorological Society*, *78*, 2539–2558, doi:10.1175/1520-0477(1997)078<2539:GPAYMA>2.0.CO;2.
- Yokoyama, E., and T. Kuroda (1990), Pattern formation in growth of snow crystals occurring in the surface kinetic process and the diffusion process, *Physical Review A*, *41*, 2038–2049, doi:10.1103/PhysRevA.41.2038.
-

- Yoshida, Y., and S. Asano (2005), Effects of the vertical profiles of cloud droplets and ice particles on the visible and near-infrared radiative properties of mixed-phase stratocumulus clouds, *Journal of the Meteorological Society of Japan. Ser. II*, *83*, 471–480, doi:10.2151/jmsj.83.471.
- Zhang, D., Z. Wang, and D. Liu (2010), A global view of midlevel liquid-layer topped stratiform cloud distribution and phase partition from CALIPSO and CloudSat measurements, *Journal of Geophysical Research (Atmospheres)*, *115*, D00H13, doi:10.1029/2009JD012143.
- Zhang, D., Z. Wang, A. Heymsfield, J. Fan, D. Liu, and M. Zhao (2012), Quantifying the impact of dust on heterogeneous ice generation in midlevel supercooled stratiform clouds, *Geophysical Research Letters*, *39*, L18805, doi:10.1029/2012GL052831.
- Zrnić, D., R. Doviak, G. Zhang, and A. Ryzhkov (2010), Bias in differential reflectivity due to cross coupling through the radiation patterns of polarimetric weather radars, *Journal of Atmospheric and Oceanic Technology*, *27*, 1624–1637, doi:10.1175/2010JTECHA1350.1.
- Zrnic, D. S., and A. V. Ryzhkov (1998), Observations of insects and birds with a polarimetric radar, *IEEE Transactions on Geoscience and Remote Sensing*, *36*, 661–668, doi:10.1109/36.662746.
- Zrnic, D. S., and A. V. Ryzhkov (1999), Polarimetry for weather surveillance radars, *Bulletin of the American Meteorological Society*, *80*, 389–406, doi:10.1175/1520-0477(1999)080<0389:PFWSR>2.0.CO;2.
- Zrnić, D. S., and A. V. Ryzhkov (2004), Polarimetric properties of chaff, *Journal of Atmospheric and Oceanic Technology*, *21*, 1017–1024, doi:10.1175/1520-0426(2004)021<1017:PPOC>2.0.CO;2.
- Zrnic, D. S., R. Raghavan, and V. Chandrasekar (1994), Observations of copolar correlation coefficient through a bright band at vertical incidence, *Journal of Applied Meteorology*, *33*, 45–52, doi:10.1175/1520-0450(1994)033<0045:OOCCT>2.0.CO;2.
- Zuidema, P., B. Baker, Y. Han, J. Intrieri, J. Key, P. Lawson, S. Matrosov, M. Shupe, R. Stone, and T. Uttal (2005), An Arctic springtime mixed-phase cloudy boundary layer observed during SHEBA, *Journal of Atmospheric Sciences*, *62*, 160–176, doi:10.1175/JAS-3368.1.
-





## List of Abbreviations

ACCEPT	Analysis of the Composition of Clouds with Extended Polarization Techniques
ACTRIS	Aerosol, Clouds and Trace gases Research Infrastructure
CESAR	Cabauw Experimental Site for Atmospheric Research
CCN	Cloud condensation nuclei
FFT	Fast Fourier Transformation
GDAS	Global Data Assimilation System
INP	Ice nucleating particle
IS	Ice saturation
ITaRS	Initial Training for atmospheric Remote Sensing
IWC	Ice water content
KNMI	Royal Netherlands Meteorological Institute
LACROS	Leipzig Aerosol and Cloud Remote Observation System
LWC	Liquid water content
NEXRAD	Next-generation radar
NOAA	National Oceanic and Atmospheric Administration
OMT	Orthomode transducer
OPERA	European Operational Program for Exchange of Weather Radar Information
STSR	Simultaneous transmitting and receiving
TROPOS	Leibniz Institute for Tropospheric Research
UTC	Coordinated Universal Time
WS	Water saturation
V-QL-S	Vapor-Quasi-Liquid-Solid mechanism

---



# List of Symbols

Symbol	Description
$a$	Width of an ice crystal
$A$	Half-power of non-polarized part in the description basis
$A_a$	Non-polarized component of the received signal produced by anisotropic scattering
$A_{cor}$	Parameter $A_L$ corrected for the polarization coupling
$A_i$	Parameter $A_L$ measured for isotropic scatterers
$A'_i$	Normalized $A_i$
$A_L$	Half-power of non-polarized part in the LDR mode
$A_S$	Half-power of non-polarized part in the slanted basis
$A'_S$	Parameter $A_S$ corrected for the polarization coupling
$B$	Power of fully-polarized parts in the horizontal channel
$B_i$	Parameter $B_L$ measured for isotropic scatterers
$B'_i$	Normalized $B_i$
$B_L$	Power of fully-polarized parts in the co-channel
$B_S$	Power of fully-polarized parts in the cross-channel in the slanted basis
$B'_S$	Parameter $B_S$ corrected for the polarization coupling
$B_{hh}, \dot{B}_{hv},$ $\dot{B}_{vh}, B_{vv}$	Elements of $\mathbf{B}$
$B_{xx}, \dot{B}_{xc},$ $B_{cc}$	Elements of $\mathbf{B}_S$
$B_{Tc}, B_{Tx}$	Thresholds applied for the signal detection in the co- and cross-channel
$B'_{xx}, B'_{cc}$	Elements $B_{xx}$ and $B_{cc}$ corrected for noise levels
$\hat{B}_{hh}, \hat{B}_{hv},$ $\hat{B}_{vh}, \hat{B}_{vv}$	Modeled elements of the coherency matrix
$\hat{B}'_{hv}, B'_{vv}$	Elements $\hat{B}_{hv}$ and $B_{vv}$ corrected for the amplification difference
$\mathbf{B}$	Spectral coherency matrix
$\mathbf{B}'$	Spectral coherency matrix corrected for the amplification difference
$\mathbf{B}_S$	Spectral coherency matrix in the slanted polarization basis
$\mathbf{B}'_S$	Spectral coherency matrix in the slanted polarization basis corrected for noise levels

---

Symbol	Description
$c$	Height of an ice crystal
$C$	Powers of fully-polarized parts in the vertical channel
$C_0$	Constant in Eq. (2.3)
$C_a$	Fully-polarized component of the received signal produced by anisotropic scattering
$C_{cor}$	Parameter $C_L$ corrected for the polarization coupling
$C_i$	Parameter $C_L$ measured for isotropic scatterers
$C'_i$	Normalized $C_i$
$C_L$	Power of fully-polarized parts in the cross-channel
$C_S$	Powers of fully-polarized parts in the co-channel in the slanted basis
$C'_S$	Parameter $C_S$ corrected for the polarization coupling
$d_1, d_2$	Depolarizing factors
$D$	Covariance of signals in the horizontal and vertical channels
$\dot{D}_L$	Covariance of signals in the co- and cross-channels in LDR mode
$D_S$	Covariance of signals in the co- and cross-channels in the slanted basis
$E_{c,x}$	Amplitudes of signals in the co- ( $c$ ) and cross- ( $x$ ) receiving channel
$E_{ZDR},$	
$E_{RHV}, E_s$	Error functions related to Eqs. (5.41) – (5.43)
$\dot{E}_{c,x}$	Complex amplitudes of signals in the co- ( $c$ ) and cross- ( $x$ ) receiving channel
$\dot{E}_{h,v}$	Complex amplitudes of the received signals in the horizontal and vertical channels
$\dot{E}_{th,tv}$	Complex amplitudes of the transmitted signals in the horizontal and vertical channels
$\mathbf{e}_h, \mathbf{e}_v, \mathbf{e}_z$	Unit vectors forming the measurement coordinate system
$f_r$	Pulse repetition frequency
$\dot{f}_{cc, cx, xc, xx}$	Elements of $\mathbf{F}$
$F_1 - F_{11}$	Related to Eqs. (5.17) – (5.27)
$F_{cc, cx, xc, xx}$	Normalized amplitude antenna patterns
$\mathbf{F}$	Matrix form of receiving antenna patterns
$\mathbf{F}'$	Matrix form of normalized receiving antenna patterns
$\mathbf{F}_R$	Rotational operator
$H_{1,2,3}$	Related to Eqs. (3.6)–(3.8)
$i$	Imaginary unit
$\mathbf{I}$	Unit matrix
$I_c, I_x$	In-phase components in the co- and cross-channels
$I_h, I_v$	In-phase components in the horizontal and vertical channels
ICPR	Integrated cross-polarization ratio
ICPR <sub>ub</sub>	Upper bound of ICPR

---

---

Symbol	Description
$J_{cc}, \dot{J}_{cx},$ $\dot{J}_{xc}, J_{xx}$	Elements of the coherency matrix $\mathbf{J}$
$\mathbf{J}$	Coherency matrix in LDR mode
$k_0$	Free-space wavenumber
$K_a$	Correction coefficient related to Eq. (4.8)
$K_n$	Correction coefficient related to Eq. (4.34)
$K_{DP}$	Specific differential phase shift
LDR	Linear depolarization ratio
$\text{LDR}_{cor}$	LDR corrected for the polarization coupling
$\text{LDR}_i$	LDR for isotropic particles
$m$	Mass of an ice crystal
$N$	Number of scatterers in the scattering volume
$N_c, N_x$	Noise levels in the co- and cross-channels
$N_F$	Number of pulses used for FFT
$N_h, N_v$	Noise levels in the horizontal and vertical channels
$N_s$	Number of spectra for averaging
$p_{1,2}$	Polarizability elements
$P_{1,2}$	Related to Eqs. (5.28) and (5.29)
$P_{c,x}$	Powers in the co- and cross-channel
$Q$	Related to Eq. (4.16)
$Q_c, Q_x$	Quadrature components in the co- and cross-channels
$Q_h, Q_v$	Quadrature components in the horizontal and vertical channels
$r$	Distance to a scatterer
$r_s$	Distance to the scattering volume
$R$	Factor related to Eq. (5.32)
$R_{1,2}$	Related to Eqs. (3.10) and (3.11)
$\dot{S}_h, \dot{S}_v$	Discrete complex spectra in the horizontal and vertical channels
$\dot{S}_{hh}, \dot{S}_{hv},$ $\dot{S}_{vh}, \dot{S}_{vv}$	Elements of the matrix $\mathbf{S}$
$(\dot{S}_{hh})_\Sigma,$ $(\dot{S}_{hv})_\Sigma,$ $(\dot{S}_{vh})_\Sigma,$ $(\dot{S}_{vv})_\Sigma$	Elements of the matrix $\mathbf{S}_\Sigma$
$s_i$	Area of the $i$ -th crystal surface
SLDR	Slanted linear depolarization ratio
$\widehat{\text{SLDR}}$	Modeled slanted linear depolarization ratio
SNR	Signal-to-noise ratio
$\text{SNR}_{h,v}$	Signal-to-noise ratios of signals in the horizontal (h) and vertical (v) receiving channel

---

---

Symbol	Description
$\mathbf{S}$	Scattering matrix for a single particle
$\mathbf{S}_\Sigma$	Scattering matrix of a scattering volume
$T_{1,2}$	Related to Eqs. (5.30) and (5.31)
$V$	Volume of an approximating spheroid
$W$	Probability density function
$Z_h$	Equivalent radar reflectivity factor
$Z_{DR}$	Differential reflectivity
$\hat{Z}_{DR}$	Modeled differential reflectivity
$\alpha_{1,2,3}$	Phase differences
$\beta$	Orientation angle of the polarization plane of the transmitted signal
$\gamma$	Argument of $\dot{J}_{cx}$
$\delta$	Backscattering differential phase shift
$\Delta G$	Total free energy of a crystal
$\Delta G_i$	Free energy of the i-th crystal surface
$\Delta\phi_{bs}$	Phase shift produced by atmospheric scatterers
$\Delta\phi_{ps}$	Phase shift introduced by the phase shifter
$\Delta\phi_{rp}$	Phase shift caused by the difference in the electrical path lengths between the reception channels
$\Delta\phi_R$	Reception phase difference
$\Delta\phi_{tp}$	Phase shift caused by the difference in the electrical path lengths between the transmission channels
$\Delta\phi_T$	Transmission phase difference
$\Delta\phi_\Sigma$	Total phase difference between the horizontal and vertical channels
$\Delta\Phi$	Phase shift between the orthogonal components in the LDR mode
$\epsilon_0$	Vacuum permittivity
$\epsilon_r$	Relative permittivity
$\theta$	Azimuth angle with respect to the maximum of the radar beam
$\theta_0$	Mean elevation orientation of spheroids
$\theta_p$	Elevation orientation of the spheroid symmetry axis
$\Theta$	Parameter related to Eq. (5.32)
$\kappa$	Degree of orientation
$\lambda$	Wavelength
$\lambda_g$	Wavelength in a waveguide
$\Lambda_{1,2}$	Related to Eq. (5.6)
$\mu$	Degree of polarization
$\xi_e$	Polarizability ratio
$\xi_g$	Axis ratio
$\rho_a$	Apparent ice density
$\rho_b$	Bias in $\rho_{cx}$

---

---

Symbol	Description
$\rho_{cor}$	Parameter $\rho_{cx}$ corrected for the polarization coupling
$\rho_{cx}$	Cross-correlation coefficient in LDR mode
$\rho_{hv}$	Correlation coefficient
$\hat{\rho}_s$	Modeled cross-correlation coefficient in the slanted basis
$\hat{\rho}_{hv}$	Modeled correlation coefficient
$\rho_s$	Cross-correlation coefficient in the slanted basis
$\sigma$	Standard deviation
$\sigma_i$	Work spent in forming a unit of the $i$ -th crystal surface
$\phi$	Elevation angle with respect to the maximum of the radar beam
$\varphi_p$	Azimuth orientation of the spheroid symmetry axis
$\Phi$	Related to Fig. 3.9
$\Phi_{c,x}$	Phases of signals in the co- ( $c$ ) and cross- ( $x$ ) receiving channel
$\Phi_{DP}$	Differential phase shift
$\psi$	Elevation angle
$\omega_k$	Spectral components for a spectral line $k$
$\omega_n$	Spectral components with SNR in both channels higher than 30 dB
$\Omega$	Solid angle

---





# Acknowledgements

The work leading to this thesis has received funding from the European Union Seventh Framework Programme (FP7/2007–2013): People, ITN Marie Curie Actions Programme (2012–2016) in the frame of Initial Training for atmospheric Remote Sensing (ITaRS) under grant agreement no. 289923. The ACCEPT campaign was partly funded by the European Union Seventh Framework Programme (FP7/2007–2013) under grant agreement no. 262254.

I express my gratitude to all the partners of the ITaRS program for giving me an opportunity to contribute to the project. In the frame of ITaRS I participated in fruitful trainings, which helped me to improve presentation, writing, and networking skills and to build an excellent basis for my future professional activity. Many thanks go to all the ITaRS fellows for sharing the experience and enjoying summer schools, secondment periods, and conferences.

I sincerely appreciate the support from my host institution, the Leibniz Institute for Tropospheric Research, for providing me with administrative, bibliographical, and instrumental resources needed for my work.

I would like to thank my supervisory board committee: Prof. Macke, Prof. Russchenberg, Dr. Wandinger, and Dr. Seifert. With their brilliant guidance, encouragement, and continuous support, I have brought my small ideas to atmospheric science. My special thanks go to Dr. Wandinger, and Dr. Seifert for making my first days in Germany easier. I admire their invaluable help with corrections of papers and the thesis.

I would also acknowledge the support from METEK GmbH. Matthias Bauer-Pfunstein, Alexander Partus, and Hans-Jürgen Kirtzel have spent a lot of effort performing the antenna measurements, hardware and software developments.

I am grateful for the support of METEK GmbH, the Technical University of Delft, The Royal Netherlands Meteorological Institute, and the Ludwig Maximilian University of Munich during the ACCEPT campaign. I would like to express my deep gratitude to Prof. Takahashi from the Hokkaido University of Education, Sapporo, Japan, for providing the data from the free-fall cloud chamber. The evaluation of my retrieval would have been impossible without his effort.

I wish to thank my family, my girlfriend Tanya, and friends for their kind support.



## **Statement of authorship**

I hereby certify that this dissertation thesis has been composed by myself, and describes my own work, unless otherwise acknowledged in the text. All references and verbatim extracts have been quoted, and all sources of information have been specifically acknowledged. It has not been accepted in any previous application for a degree.

.....

Alexander Myagkov

After positive appraisal of this thesis, I agree that one copy of my presented thesis may remain at the disposal of the library of Leipzig University.

.....

Alexander Myagkov